Measurement and modeling of thermodynamic properties for the processing of polymers in supercritical fluids

Measurement and modeling of thermodynamic properties for the processing of polymers in supercritical fluids

PROEFSCHRIFT

ter verkrijging van de graad van doctor aan de
Technische Universiteit Eindhoven, op gezag van de
Rector Magnificus, prof.dr. R.A. van Santen, voor een
commissie aangewezen door het College voor
Promoties in het openbaar te verdedigen
op maandag 13 september 2004 om 16.00 uur

door

Marcus Antonius Jacobs

geboren te Oost-, West- en Middelbeers

Dit proefschrift is goedgekeurd door de promotoren:

prof.dr.ir. J.T.F. Keurentjes
en
prof.dr.ir. L.P.B.M. Janssen

Copromotor:
dr.ir. M.F. Kemmere

Omslagontwerp: Dion van Rijswijk, Sittard.

CIP-DATA LIBRARY TECHNISCHE UNIVERSITEIT EINDHOVEN

Jacobs, Marcus A.

Measurement and modeling of thermodynamic properties for the processing of polymers in supercritical fluids / by Marcus A. Jacobs. – Eindhoven : Technische Universiteit Eindhoven, 2004.
Proefschrift. – ISBN 90-386-2596-0
NUR 913
Trefwoorden: polymeermengsels / polymeren ; fysische eigenschappen / superkritische vloeistoffen ; koolstofdioxide / thermodynamica ; fase-evenwicht / fysisch-chemische simulatie en modellering / statistische associërende vloeistof theorie ; SAFT / Peng-Robinson toestandsvergelijking
Subject headings: polymer blends / polymers ; physical properties / supercritical fluids ; carbon dioxide / thermodynamics ; phase equilibrium / physicochemical simulation and modeling / statistical associating / fluid theory ; SAFT / Peng-Robinson equation of state

Contents

CHAPTER 1

POLYMER PROCESSING USING SUPERCRITICAL FLUIDS

Abstract

Supercritical fluid technology can be used for the replacement of organic solvents in various industrial processes. The unique properties of supercritical fluids provide opportunities for a variety of polymer processes. In this chapter, the general properties of supercritical fluids and their interactions with polymers are described. Furthermore, existing applications as well as current developments are addressed. At the end of the chapter, the scope of the thesis is presented.

1.1 Strategic solvent replacement

Many polymer production and processing applications involve an excessive use of organic solvents, either as a reaction medium or as a processing medium for extraction, impregnation or viscosity reduction. In Figure 1.1 a typical polymer production scheme is shown. In the production of polymers, three sub-processes can be identified: the polymerization of the monomer(s), the shaping of the raw polymer and the post-processing of the polymer[1]. In each of these steps, most of the effort of the process is put into the solvent recovery. For example, in the production of butadiene rubber (BR) a typical production process applies a recycle of approximately 4 tons of solvent per ton BR[2], while conversions are usually below 60%. Annually, these processes add substantially to the total amount of emitted volatile organic compounds (VOC) such as hexane and toluene. For these reasons, it is highly desired to replace these solvents and other organic solvents with an environmentally benign and easily recoverable solvent, both from an environmental and from an economical point of view. In our opinion, supercritical carbon dioxide can act as a viable alternative solvent for polymer processing. Besides the obvious environmental benefits, supercritical carbon dioxide also has interesting physical and chemical properties from a process point of view. These include its relative chemical inertness, readily accessible critical point, and its highly tunable solvent behavior, thus facilitating easy separation.

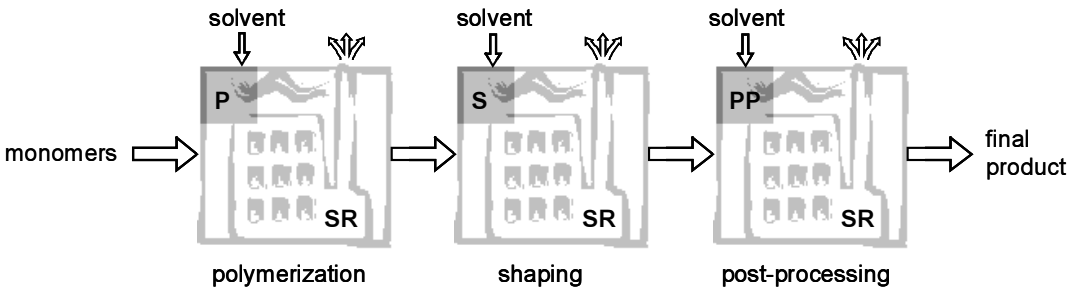

Figure 1.1 General polymer production scheme.

1.2 Physical and chemical properties of supercritical fluids

In 1822, Baron Gagniard de la Tour discovered the critical point of a substance in his famous cannon barrel experiments. Listening to discontinuities in the sound of a rolling flint ball in a sealed cannon, he observed the critical temperature.

Table 1.1 Physical properties of various solvents[3-5].

	T_c (K)	P_c (bar)	$\alpha \times 10^{25}$ (cm^3)	μ (D)	$Q \times 10^{26}$ ($erg^{1/2}\ cm^{5/2}$)
methane	190.4	46.0	26	0.0	
ethane	305.3	48.7	45.0	0.0	-0.7
propane	369.8	42.5	62.9	0.1	
ethylene	282.4	50.4	42.3	0.0	
propylene	364.9	46.0	62.6	0.4	
ethyne	308.3	61.4	33.3	0.0	+3.0
dimethyl ether	400.0	52.4	51.6	1.3	
sulfur hexafluoride	318.7	37.6	54.6	0.0	
difluoromethane	351.6	58.3	24.8	2.0	
trifluoromethane	299.3	48.6	26.5	1.7	
tetrafluoromethane	227.6	37.4	28.6	0.0	
difluoroethane	386.7	45.0	41.5	2.3	
hexafluoroethane	293.0	30.6	47.6	0.0	-0.7
carbon dioxide	304.1	73.8	27.6	0.0	-4.3
n-hexane	507.5	30.1	118.3	0.0	
cyclohexane	553.5	40.7	109	0.3	
diethyl ether	466.7	36.4	87.3	1.3	
methanol	512.6	80.9	32.3	1.7	
acetone	508.1	47.0	63.3	2.9	

α is the polarizability, μ is the dipole moment and Q is the quadrupole moment.

Above this temperature, the distinction between the liquid phase and the gas phase disappears, resulting in a single supercritical fluid phase. In Table 1.1, the critical properties are shown for some components, which are commonly used as supercritical fluids. Of these components, carbon dioxide and water are the most frequently used in a wide range of applications. In polymer systems, ethylene and propylene are also widely used, where they act both as a solvent and as the reacting monomer[6].

In Figure 1.2, two projections of the phase diagram of carbon dioxide are shown. In the pressure-temperature phase diagram (Figure 1.2a) the boiling line is observed, which separates the vapor and liquid region and ends in the critical point. At the critical point, the densities of the equilibrium liquid phase and the

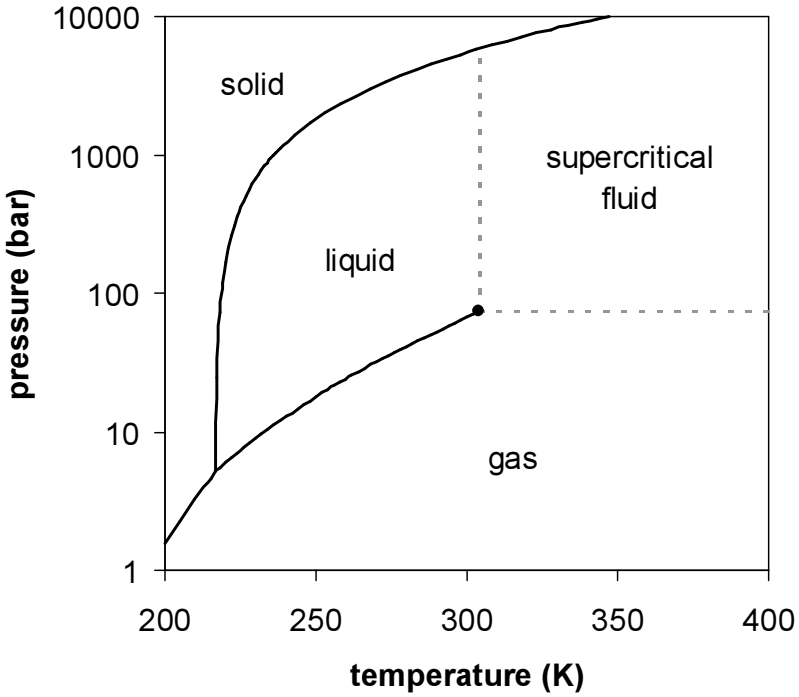

A

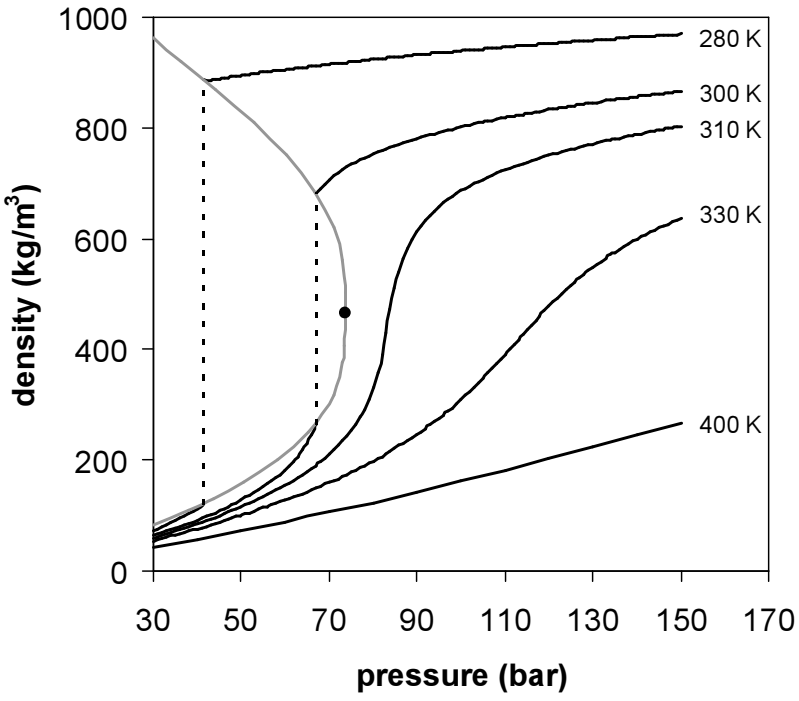

B

Figure 1.2 Projections of the phase diagram of carbon dioxide A) in the pressure-temperature plane and B) in the density-pressure plane[7,8].

saturated vapor phases become equal, resulting in the formation of a single supercritical phase. This can be observed in the density-pressure phase diagram for carbon dioxide, as shown in Figure 1.2b, where the critical point is located at 304.1 K and 73.8 bar. With increasing temperatures, the liquid-vapor density gap decreases, up to the critical temperature, at which the discontinuity disappears. Thus, above the critical temperature a gas cannot be liquefied by pressure. However, at extremely high pressures the fluid can solidify, as visible at the top of Figure 1.2a. By definition, a supercritical fluid is a substance above both its critical temperature and pressure. In a practical sense, the area of interest in supercritical fluids for processing and separation purposes is limited to temperatures in the vicinity of the critical point, where large gradients in the physical properties are observed. The changes near the critical point are not limited to density. Many other physical properties also show large gradients with pressure near the critical point, e.g. viscosity, the relative permittivity and the solvent strength, which are all closely related to the density. At higher temperatures, the fluid starts to behave like a gas, as can be seen in Figure 1.2b. For carbon dioxide at 400 K, the density increases almost linearly with pressure.

For engineering purposes, supercritical fluids can be regarded as "hybrid solvents" with properties between those of gases and liquids, i.e. a solvent with a low viscosity, high diffusion rates and no surface tension. In the case of supercritical carbon dioxide, the viscosity is in the range of 0.02-0.1 cP, where liquids have viscosities of approximately 0.5-1.0 cP and gases approximately 0.01 cP, respectively. Diffusivities of solutes in supercritical carbon dioxide are up to a factor 10 higher than in liquid solvents. Additionally, these properties are strongly pressure-dependent in the vicinity of the critical point, making supercritical fluids highly tunable solvents.

1.3 Interactions of carbon dioxide with polymers and solutes

The thermodynamic properties of pure substances and mixtures of molecules are determined by intermolecular forces acting between the molecules or polymer segments. By examining these potentials between molecules in a mixture, insight in the solution behavior of the mixture can be obtained. The most common occurring interactions are dispersion, dipole-dipole, dipole-quadrupole, quadrupole-quadrupole and specific interactions, as shown in Figure 1.3. For small molecules, the contribution of each interaction to the intermolecular potential energy $\Gamma_{ij}(r,T)$, is given by[5]

$$\Gamma_{ij}(r,T) \approx -\left[C_1 \frac{\alpha_i \alpha_j}{r^6} + C_2 \frac{\mu_i^2 \mu_j^2}{r^6 kT} + C_3 \frac{\mu_i^2 Q_j^2}{r^8 kT} + C_4 \frac{Q_i^2 Q_j^2}{r^{10} kT} + \mathrm{SI} \right] \tag{1.1}$$

where α is the polarizability, μ is the dipole moment and Q is the quadruple moment and SI are specifics interactions like complex formation or hydrogen bonding. The interactions work over different distances, with the longest range for dispersion and dipole interactions. Note that the dispersion interaction depends on the polarizability only and not on the temperature. Consequently, an increased polarizability of the supercritical solvent is expected to decrease the pressures needed to dissolve a nonpolar solute or polymer. Furthermore, at elevated temperatures, the configurational alignment of directional interactions as dipoles or quadrupoles is disrupted by the thermal energy, leading to a nonpolar behavior. Hence, it may be possible to dissolve a nonpolar solute or a polymer in a polar supercritical fluid. However, to obtain sufficient density for dissolving the solutes at those elevated temperatures, substantially higher pressures need to be applied.

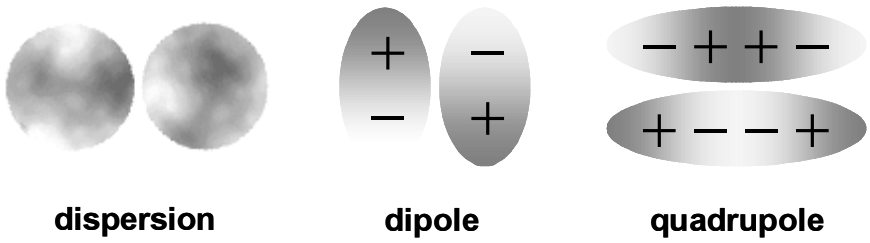

Figure 1.3 Charge distributions for various molecular interactions

Additionally, specific interactions such as complex formation and hydrogen bonding can increase the solvent strength of the supercritical fluid. These interactions are also highly temperature sensitive.

1.3.1 Solubility in carbon dioxide

The solvent strength of carbon dioxide for solutes is dominated by a low polarizability and a strong quadrupole moment, as shown in Table 1.1. Consequently, carbon dioxide is difficult to compare to conventional solvents, due to this ambivalent character. With its low polarizability and nonpolarity, carbon dioxide is similar to perfluoromethane, perfluoroethane and to methane. These fluids are very weak solvents for many components. Additionally, the acidity of carbon dioxide increases the solvent strength for weakly basic solutes. In general,

carbon dioxide is a reasonable solvent for small molecules, both polar and nonpolar. For many components, with the exception of water, complete miscibility can be obtained at elevated pressures. However, the critical point of the mixture, i.e. the lowest pressure at a given temperature where CO_2 is still completely miscible, raises sharply with increasing molecule size, as shown for some *n*-alkanes in Figure 1.4.

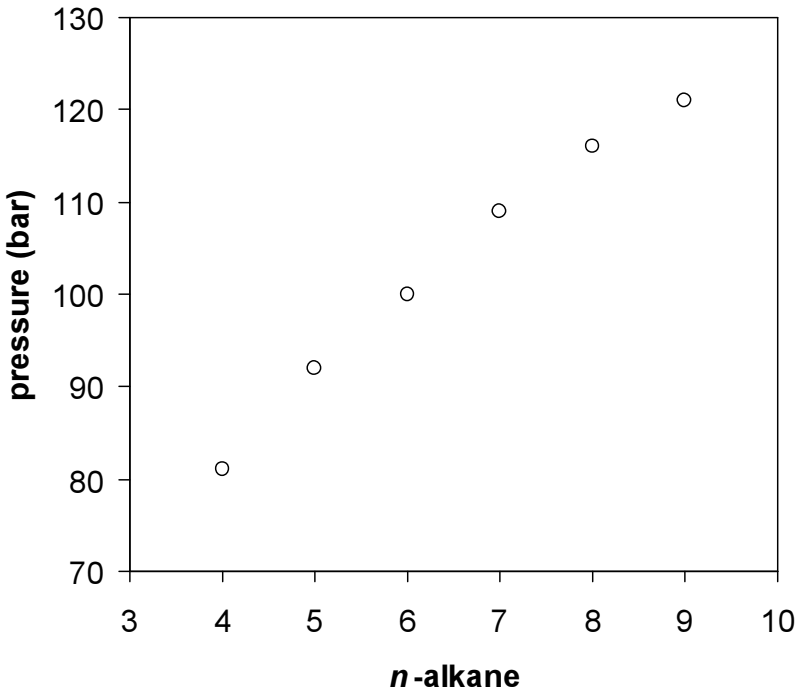

Figure 1.4 Mixture critical pressure of n-alkanes with carbon dioxide at 343 K.

Consequently, most larger components and polymers exhibit a very limited solubility in carbon dioxide. Polymers that do exhibit a large solubility in carbon dioxide[9-12] are commonly characterized by a flexible backbone and a high free volume (hence low T_g), weak interactions between the polymer segments and a weakly basic interaction site like a carbonyl group. Carbon dioxide soluble polymers incorporating these characteristics are e.g. poly(alkene oxides), perfluorinated poly(propylene oxide), poly(methyl acrylate), poly(vinyl acetate), poly(alkyl siloxanes) and poly(ether carbonate).

The influence of the carbonyl group on the solubility of the polymer in carbon dioxide is apparent from the difference in cloud-point pressures for poly(methyl acrylate) and poly(vinyl acetate), shown in Figure 1.5. Structurally these polymers are very similar, however, the carbonyl group in PVA is more easily accessible to CO_2 making it more susceptible to complex formation. As a result, the cloud-point

pressure of PVA is up to 1500 bar lower than that of PMA, even though the molecular weight of PVA is four times higher than that of PMA, and its glass transition temperature is 21 K higher.

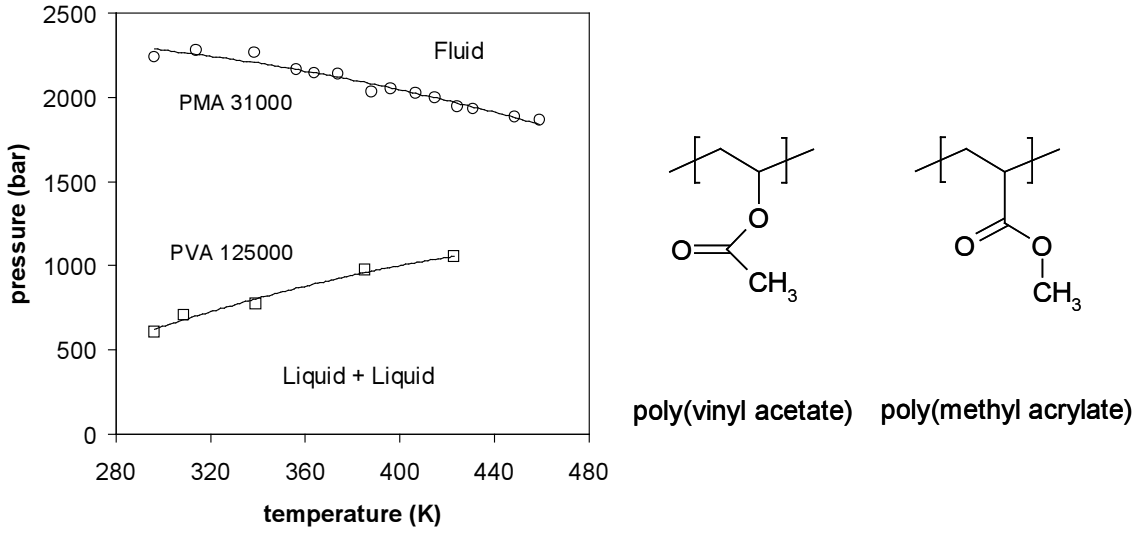

Figure 1.5 Cloud-point curves of carbon dioxide-poly(methyl acrylate) and carbon dioxide-poly(vinyl acetate) with polymer concentrations of ~5 wt%[9].

1.3.2 Sorption and swelling of polymers

The sorption of carbon dioxide by polymers and the resulting swelling of the polymer are related to the solution behavior of polymers in high-density carbon dioxide. The conditions at which polymers show a high degree of sorption in supercritical carbon dioxide are identical to those of high solubility. The sorption of CO_2 into polymers results in swelling of the polymer and induces changes in the mechanical and physical properties of the polymers. The most important effect is plasticization, i.e. the reduction of the glass transition temperature (T_g) of glassy polymers. The plasticization, characterized by increased segmental mobility, chain mobility and inter-chain distance, is largely determined by polymer-solvent interactions and solvent size[14]. The molecular weight of the polymer is of little influence on the swelling once the entanglement molecular weight has been exceeded. The influence of specific interactions of carbon dioxide with various groups in the polymer on the swelling isotherms is shown in Figure 1.6.[13] These polymers all have a T_g of approximately 378 K. Carbon dioxide shows little interaction with the phenyl groups in PS, resulting in limited swelling. Substituting one of the CH groups in styrene with a nitrogen atom renders

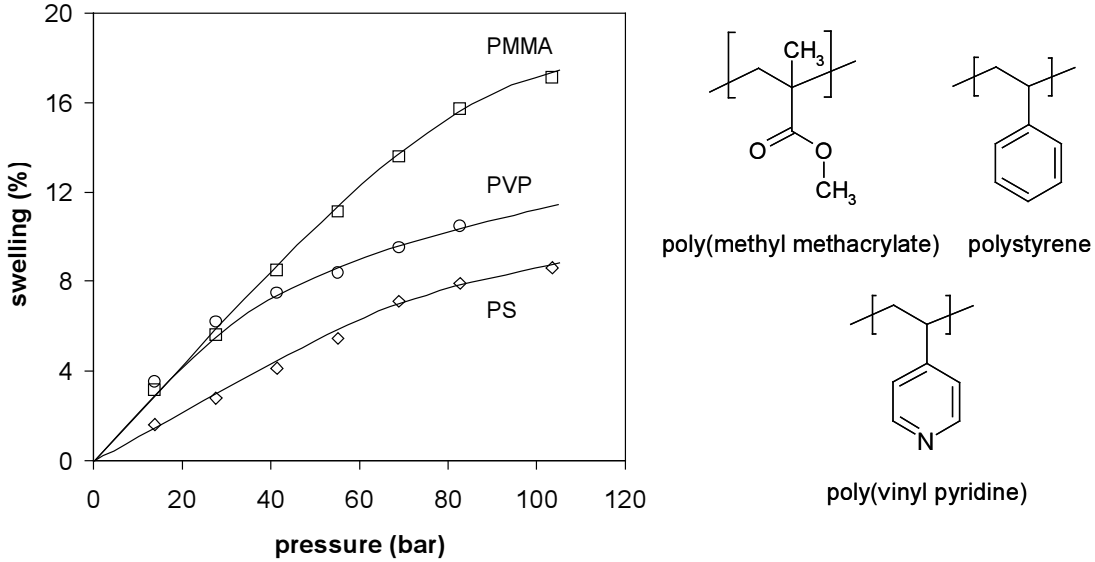

Figure 1.6 Swelling isotherms of poly(methyl methacrylate), polystyrene and poly(vinyl pyridine) in carbon dioxide at 308 K.[13]

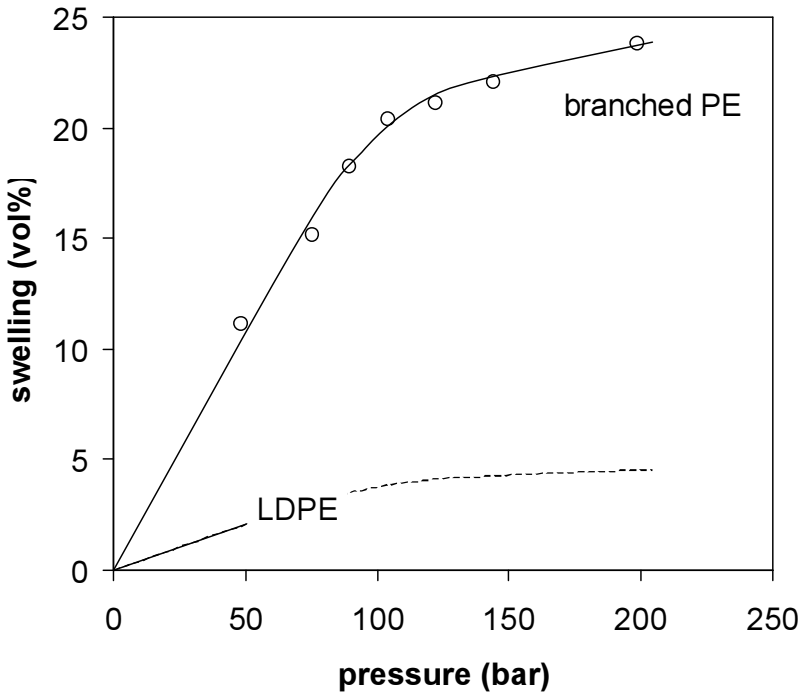

Figure 1.7 Sorption isotherms of a highly branched polyethylene[16] *and commercial LDPE*[15] *at 323 K. Lines are trend lines; the dotted line is a possible extrapolation of the low-pressure measurements (Henry sorption regime).*

the polymer somewhat basic, thereby increasing the swelling level as well as the swelling rate. Building carbonyl groups into the polymer has an even stronger effect. In the case of PMMA, the swelling level is doubled compared to PS.

Besides enhancing interactions with carbon dioxide, the sorption and swelling can also be increased by lowering the inter-chain interactions of the polymer. This is shown in Figure 1.7 for commercial semi-crystalline LDPE[15] (40% cryst., measurements in the Henry sorption regime) and highly branched amorphous polyethylene[16] (< 2% cryst.). Although both polymers lack specific interactions with carbon dioxide, the highly branched PE shows a strongly enhanced swelling in carbon dioxide. This is caused by the absence of crystallinity and the increased free volume introduced by branching.

1.4 Applications and current research

Applications of supercritical fluids in polymer processing can be divided into three areas: processing of swollen and dissolved polymers and applications where carbon dioxide does not interact with the polymer. Schematically, this is shown in Figure 1.8.[17] In the first case, when no interaction with the polymer occurs, which is typically the case for crystalline and rigid polymers, supercritical carbon dioxide can be used as a cleaning solvent. Applications in this category include precision cleaning of surfaces, degreasing, particle removal and dry cleaning. In particular, dry cleaning is industrially investigated for widespread application, as traditional processes using perchloroethylene are under pressure due to health and environmental issues. Current research in this area is focused on the development of low-cost non-fluorous CO_2-phylic surfactants[11,18] and on the development of membrane systems for the economical reuse of carbon dioxide[19].

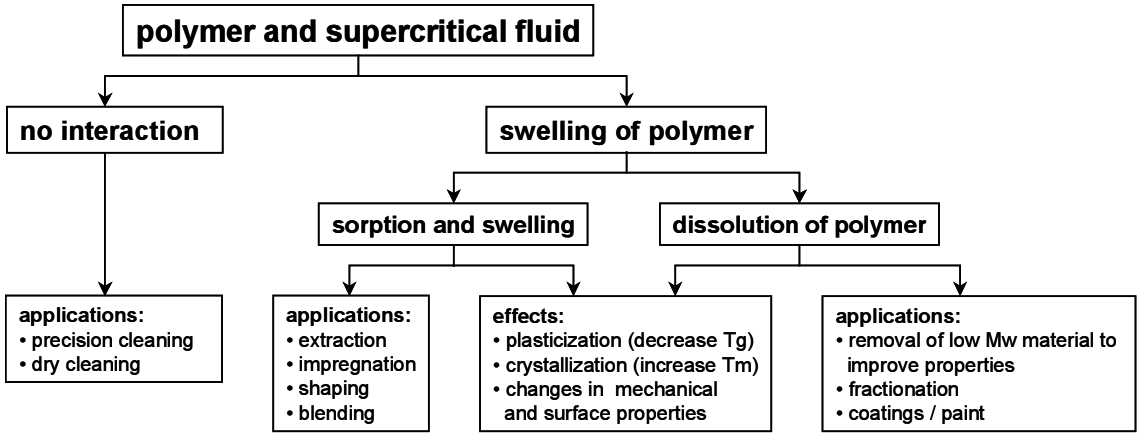

Figure 1.8 Interactions of supercritical fluids with polymers and their applications[17].

In the case of moderate interactions of carbon dioxide with the polymer, substantial levels of sorption and swelling can occur. The swelling of the polymer significantly enhances diffusivities of solutes in the polymer matrix, enabling rapid extraction and impregnation processes. Extraction applications include removal of residual monomers, solvents and catalysts[20,21]. An important application of impregnation of polymers is the dyeing of textiles and fibers, motivated by the replacement of large amounts of water in the dying process[22,23]. Another interesting application is *in situ* polymerization in an existing polymer matrix after impregnation with a monomer and an initiator to form polymer blends[24]. This enables the formation of polymer blends that cannot easily be obtained by conventional methods, e.g. due to large differences in melting temperatures. Other impregnation applications include impregnation of polymer matrices with drugs for the production of controlled drug delivery devices[25]. Advantages in this process are low processing temperatures and the lack of organic solvents, which need to be removed in post-processing steps.

Applications in the third category, where the polymer is dissolved in the supercritical fluid, include coating processes. Various groups have worked on the RESS-based process for spray coating using supercritical carbon dioxide as a solvent[26-28]. The main advantage of these processes is the reduction of VOC emissions. However, as most coating materials show low solubilities in supercritical carbon dioxide, cosolvents like methanol are needed to enhance solubilities. An alternative to the addition of cosolvents is the use of stabilizers, as demonstrated by Shim et al[29].

A more elaborate overview of polymer processing applications using supercritical fluids, including the applications mentioned above, is given in an extensive review by Kazarian[14].

1.5 Outline of the thesis

The aim of this thesis is to investigate some fundamental issues rising from the use of supercritical carbon dioxide in various polymer processing applications. These include the phase behavior of polymer-supercritical carbon dioxide systems, and the shaping of polymers using supercritical carbon dioxide. Chapter 2 examines the equation-of-state modeling of antisolvent effects of carbon dioxide on EPDM cloud-points in ethylene, using the Sanchez-Lacombe model and the Statistical Associating Fluid theory (SAFT) model. In Chapter 3 the foam processing of a rubbery poly(ethylene-*co*-vinyl acetate) (EVA) copolymer is studied. The influence of process conditions on the morphology are discussed, as

well as the sorption and swelling behavior of EVA in supercritical carbon dioxide. An important and widely overlooked issue in polymer processing using supercritical fluids is the swelling of the polymer. Chapters 4 and 5 describe a new method for the simultaneous measurement of sorption and swelling of polymers under high pressures. In Chapter 4, a high-pressure fluid level detection technique is presented. This technique is applied in the swelling apparatus, which is presented in Chapter 5. Finally, Chapter 6 addresses several remaining challenges in modeling and measurement of polymer-supercritical fluid interactions.

1.6 References

1. K.H. Reichert and H.U. Moritz, *Compr. Polym. Sci.* **3** (1989) 327.
2. International Institute of Synthetic Rubber Producers, Inc., internet publication http://www.iisrp.com/WebPolymers/01FinalPolybutadieneVer2.pdf
3. R.C. Reid, J.M. Prausnitz and B.E. Poling, *The Properties of Gases and Liquids*, 4th ed., McGraw-Hill, New York, 1987.
4. C.F. Kirby and M.A. McHugh, *Chem. Rev.* **99** (1999) 565.
5. J.M. Prausnitz, R.N. Lichtenthaler and E.G. de Azevedo, *Molecular Thermodynamics of Fluid Phase Equilibria*, 2nd ed., Prentice-Hall, Englewood Cliffs, 1986.
6. H. Orbey, C.P. Bokis and C.C. Chen, *Ind. Eng. Chem. Res.* **37** (1998) 4481.
7. S. Angus, B. Armstrong and K.M. de Reuck, *International Thermodynamic Tables of the Fluid State. Carbon Dioxide*, Pergamon Press, Oxford, 1976.
8. R. Span and W. Wagner, *J. Phys. Chem. Ref. Data* **25** (1996) 1509.
9. F. Rindfleisch, T.P. DiNoia and M.A. McHugh, *J. Phys. Chem.* **100** (1996) 15581.
10. T. Sarbu, T. Styranec and E.J. Beckman, *Ind. Eng. Chem. Res.* **39** (2000) 1678.
11. T. Sarbu, T. Styranec and E.J. Beckman, *Nature* **405** (2000) 165.
12. S.G. Kazarian, M.F. Vincent, F.V. Bright, C.L. Liotta and C.A. Eckert, *J. Am. Chem. Soc.* **118** (1996) 1729.
13. Y. Zhang, K.K. Gangwani and R.M. Lemert, *J. Supercrit. Fluids* **11** (1997) 115.
14. S.G. Kazarian, *Polym. Sci.* **42** (2000) 78.
15. T. Hirose, K. Mizoguchi and Y. Kayima, *J. Polym. Sci. B* **24** (1986) 2107.
16. T.J. de Vries, *Late Transition State Metal Catalyzed Polymerizations of Olefins in Supercritical Carbon Dioxide*, PhD thesis, Technische Universiteit Eindhoven, Eindhoven, 2003.
17. Y.T. Shieh, J.H. Su, G. Manivannan, P.F. Lee, S.P. Sawan and W.D. Spall, *J. Appl. Polym. Sci.* **59** (1996) 695.
18. T. Sarbu, T.J. Styranec and E.J. Beckman, *Ind. Eng. Chem. Res.* **39** (2000) 4678.
19. Y.W. Chiu and C.S. Tan, *J. Supercrit. Fluids* **21** (2001) 81.
20. S. Alsoy and J.L. Duda, *AIChE J.* **44** (1998) 582.

21. M.F. Kemmere, M.H.W. Cleven, M.A. van Schilt and J.T.F. Keurentjes, *Chem. Eng. Sci.* **57** (2002) 3929.
22. M.R. De Giorgi, E. Cadoni, D. Maricca and A. Piras, *Dyes and Pigments* **45** (2000) 75.
23. M.W. Park and H.K. Bae, *J. of Supercrit. Fluids* **22** (2002) 65.
24. J.J. Watkins and T.J. McCarthy, *Macromolecules* **27** (1994) 4845.
25. O. Guney and A. Akgerman, *AIChE J.* **48** (2002) 856.
26. R.C. Petersen, D.W. Matson and R.D. Smith, *Polym. Eng. Sci.* **27** (1987) 1693.
27. Y. Chernyak, F. Henon, R.B. Harris, R.D. Gould, R.K. Franklin, J.R. Edwards, J.M. DeSimone and R.G. Carbonell, *Ind. Eng. Chem. Res.* **40** (2001) 6118.
28. R.K. Franklin, J.R. Edwards, Y. Chernyak, R.D. Gould, F. Henon and R.G. Carbonell, *Ind. Eng. Chem. Res.* **40** (2001) 6127.
29. J.J. Shim, M.Z. Yates and K.P. Johnston, *Ind. Eng. Chem. Res.* **38** (2001) 3655.

CHAPTER 2

MODELING ANTISOLVENT EFFECTS OF CARBON DIOXIDE IN ETHYLENE-PEP SYSTEMS

Abstract

Supercritical carbon dioxide is to an increasing extent used in polymer production and modification processes. To study the extent of the antisolvent effects caused by carbon dioxide on polymer-supercritical fluid systems, cloud-point measurements have been performed for poly(ethylene-*co*-propylene)-ethylene-carbon dioxide mixtures. The Sanchez-Lacombe and SAFT models are used to describe the effects of carbon dioxide on the phase behavior of the poly(ethylene-*co*-propylene)-ethylene system. Both models give a qualitative description of the increase in ethylene-PEP cloud-points upon addition of carbon dioxide. For a quantitative correlation with the Sanchez-Lacombe model, a temperature dependent interaction parameter is required. Additionally, the parameter is determined for each individual cloud-point composition. For the SAFT model, one temperature dependent interaction parameter suffices for all compositions. Assuming a monodisperse polymer, the description of the phase behavior with the SAFT model is in much better agreement with the experimental data than for the Sanchez-Lacombe model.

This chapter has been published as: M.A. Jacobs, T.J. de Vries, M.F. Kemmere, Th.W. de Loos and J.T.F. Keurentjes, Antisolvent effect of carbon dioxide in ethylene-PEP systems; SAFT and Sanchez-Lacombe modeling, *Recent Res. Devel. Appl. Polym. Sci.* **1** (2002) 171.

2.1 Introduction

In recent literature, a range of new possibilities for the deployment of supercritical fluids (SCFs) in a variety of polymer processes is reported[1]. Applications range from polymerization[2,3] and modification reactions[4,5] to processing steps like extraction and fractionation[6,7] and particle formation[8,9]. Solubility and phase separation data are required for the evaluation and design of new processes using the tunable properties of SCFs. This information is usually obtained experimentally. The experimental effort can be reduced, by using thermodynamic models to correlate and predict phase equilibria. Modeling of polymer-supercritical fluid mixtures is particularly challenging, as the model has to be able to describe the behavior of a mixture containing molecules covering a wide range of molecular weights. Regarding the models suitable for description of polymer-SCF solvent behavior, the Sanchez-Lacombe (SL) equation-of-state (eos) and the Statistical Associating Fluid Theory (SAFT) models are widely used[10-16]. These models are representative examples of a lattice model and a perturbation model, respectively.

In this work, we look at the ability of the SL and SAFT eos to correlate the poly(ethylene-co-propylene)-ethylene cloud-point behavior and the influence of CO_2 as an antisolvent on this system. The antisolvent properties of carbon dioxide are explicitly used in SAS-like processes (Supercritical Antisolvent induced phase Separation)[17,18]. Furthermore, the antisolvent effect of carbon dioxide on the phase behavior of polymer-monomer systems is a key-factor in the design of polymerization processes in supercritical carbon dioxide[19].

2.2 Thermodynamic models

2.2.1 Sanchez-Lacombe equation-of-state

The Sanchez-Lacombe (SL) equation-of-state[10-12] is based on the classical lattice-fluid theory extended with vacancies in the lattice in order to account for compressibility. The equation-of-state for pure fluids is given by

$$\tilde{\rho}^2 + \tilde{P} + \tilde{T}\left[\ln(1-\tilde{\rho}) + \left(1-\frac{1}{r}\right)\tilde{\rho}\right] = 0 \qquad (2.1)$$

where $\tilde{T}$, $\tilde{P}$ and $\tilde{\rho}$ are the reduced temperature, pressure and density, respectively. The reduced parameters are defined from characteristic fluid parameters and are in an adapted notation[13] given by

$$\begin{aligned} \tilde{P} &= P/P^* & P^* &= \varepsilon/\sigma^3 \\ \tilde{T} &= T/T^* & T^* &= P^* v_0/R \\ \tilde{\rho} &= \rho/\rho^* & \rho^* &= M/v^* \\ \tilde{v} &= v/v^* & \tilde{v} &= 1/\tilde{\rho} \\ r &= v^*/v_0 & r &= P^* v^*/RT^* \end{aligned} \tag{2.2}$$

where σ is the closest distance allowed between two mers, ε is the mer interaction energy, v_0 is the hole volume, R is the gas constant, M is the molecular weight and v^* is the hard-core molecular volume. The size parameter r can be expressed as a function of the other lattice parameters, resulting in a complete description of a pure component with three parameters, i.e. T^*, P^* and ρ^*. The adapted form of the SL-theory[13] emphasizes the ambiguous character of the hole volume v_0. Furthermore, the usual assumption of $\sigma^3 \sim v_0$ is not imposed.

The lattice fluid model for mixtures is obtained by the extension with mixing rules

$$\frac{1}{v^*} = \sum_i \frac{\phi_i}{v_i^*} \tag{2.3}$$

$$\frac{1}{v_0} = \sum_i \frac{\phi_i P_i^*}{RT_i^*} \tag{2.4}$$

$$P^* = \sum_i \phi_i P_i^* - RT \sum_j \sum_{i<j} \phi_i \phi_j \chi_{ij} \tag{2.5}$$

where ϕ_i is the close-packed volume fraction of component i in the mixture, related to mass fractions by

$$\phi_i = \frac{w_i/\rho_i^*}{\sum_j w_j/\rho_j^*} \tag{2.6}$$

The χ_{ij} parameter is usually obtained from a geometric mean approximation

$$RT\chi_{ij} = P_i^* + P_j^* - 2\sqrt{P_i^* P_j^*}\left(1 - k_{ij}\right) \tag{2.7}$$

where k_{ij} is an adjustable binary interaction parameter.

The free energy density is given by

$$g = -\tilde{\rho}P^* + P\tilde{v} + RT\tilde{v}\left[\frac{(1-\tilde{\rho})\ln(1-\tilde{\rho})}{v_0} + \frac{\tilde{\rho}\ln\tilde{\rho}}{v^*}\right] + RT\sum_i \frac{\phi_i \ln\phi_i}{v_i^*} \tag{2.8}$$

from which chemical potentials are derived by

$$\mu_i = v_i^*\left[g + \left(\frac{\partial g}{\partial \phi_i}\right)_{\phi',\tilde{v}} - \sum_j \phi_j \left(\frac{\partial g}{\partial \phi_j}\right)_{\phi',\tilde{v}}\right] \tag{2.9}$$

2.2.2 Statistical Associating Fluid Theory

The Statistical Associating Fluid Theory (SAFT) equation-of-state[14-16] is based on Wertheim's cluster expansion theory, which gives a relation between the residual Helmholtz energy due to association and the monomer density. Hard sphere, chain and association effects are incorporated using a reference fluid. Additional intermolecular forces are included through a mean field perturbation term (dispersion term).

$$\begin{aligned} a^{res} &= a^{ref} + {}^{disp} \\ a^{ref} &= a^{hs} + a^{chain} + a^{assoc} \end{aligned} \tag{2.10}$$

In a parameterized notation, the reduced residual Helmholtz energy is given by

$$\begin{aligned} \frac{a^{res}}{RT} = {} & \frac{C\left[C^2 - 3BD(\zeta_3 - 1)\right]\zeta_3}{D^2(\zeta_3 - 1)^2} + \left[\frac{C^3}{D^2} - A\right]\ln(1-\zeta_3) + F \\ & + E\sum_i \sum_j D_{ij} G^i \left(\frac{\zeta_3}{\tau}\right)^j + H \end{aligned} \tag{2.11}$$

with parameters

$$A = \sum_i x_i m_i (d_i)^0 \qquad \zeta_0 = (\pi/6)\rho A \tag{2.12}$$

$$B = \sum_i x_i m_i (d_i)^1 \qquad \zeta_1 = (\pi/6)\rho B \tag{2.13}$$

$$C = \sum_i x_i m_i (d_i)^2 \qquad \zeta_2 = (\pi/6)\rho C \tag{2.14}$$

$$D = \sum_i x_i m_i (d_i)^3 \qquad \zeta_3 = (\pi/6)\rho D \tag{2.15}$$

$$E = m = \sum_i x_i m_i \tag{2.16}$$

$$F = \frac{a^{chain}}{RT} = \sum_i x_i (1 - m_i) \ln\left(g_i(d_i)\right) \tag{2.17}$$

$$G = \frac{u}{kT} = \frac{\sum_i \sum_j x_i x_j m_i m_j \left(\frac{u_{ij}}{kT}\right) v_i^{\circ}}{\sum_i \sum_j x_i x_j m_i m_j v_{ij}^{\circ}} \tag{2.18}$$

$$H = \frac{a^{assoc}}{RT} = \sum_i \left[\sum_{A_i} \left(\ln x^{A_i} - \frac{x^{A_i}}{2} \right) + \frac{M_i}{2} \right] \tag{2.19}$$

where ρ is the density, x^{A_i} is the mole fraction of molecules *i* not bonded at site *A* and M_i is the molecular weight of component *i*. D_{ij} and τ are universal constants. The radial distribution function $g_i(d_i)$ is given by

$$g_i(d_i) = \left[\frac{1}{1-\zeta_3} + \frac{3d_i}{2} \frac{\zeta_2}{(1-\zeta_3)^2} + \frac{d_i^2}{2} \frac{\zeta_2^2}{(1-\zeta_3)^3} \right] \tag{2.20}$$

The temperature-dependent segment volume v_{ij}°, dispersion energy u_{ij} and segment diameter d_i are calculated from pure component parameters using the Van der Waals one-fluid mixing rules:

$$v_{ij}^{\circ} = \left(\frac{\left(v_i^{\circ\circ}\right)^{1/3} + \left(v_j^{\circ\circ}\right)^{1/3}}{2} \right)^3 \tag{2.21}$$

$$u_{ij} = \left(1 - k_{ij}\right) \sqrt{u_i u_j} \tag{2.22}$$

$$d_i = \left(\frac{6\tau v_i^{\circ}}{\pi N_{av}} \right) \tag{2.23}$$

where k_{ij} is an adjustable binary interaction parameter.

The compressibility factor *Z* and the fugacity coefficient ϕ are derived from the reduced residual Helmholtz energy, $\tilde{a} = a^{res} / RT$, as given in Equation (2.11).

$$Z = 1 + \rho \left(\frac{\partial \tilde{a}}{\partial \rho} \right)_{T, x_i} \tag{2.24}$$

$$\ln \phi_i = \tilde{a} + \left(\frac{\partial \tilde{a}}{\partial x_i} \right)_{\rho,T,x_{j\neq i}} - \sum_j x_j \left(\frac{\partial \tilde{a}}{\partial x_i} \right)_{\rho,T,x_{j\neq i}} + (Z-1) - \ln Z \qquad (2.25)$$

2.3 Experimental section

2.3.1 Materials

Carbon dioxide (Messer Nederland, grade 4.5) and ethylene (Aga Gas, grade 3.5) were used as received. A few parts per million of hydroquinone was added to suppress ethylene polymerization. The properties of the poly(ethylene-*co*-propylene) used, are listed in Table 2.1.

2.3.2 Cloud-point measurements

The cloud-point behavior of the systems ethylene-poly(ethylene-*co*-propylene) (PEP) and ethylene-poly(ethylene-*co*-propylene)-carbon dioxide was studied in an optical high-pressure cell for pressures up to 4000 bar and temperatures up to 450 K[20]. The cell is provided with sapphire windows and magnetic stirring. For a detailed description of the apparatus and the experimental techniques used, we refer to De Loos et al.[21].

The cloud-point pressures of mixtures of known composition were measured as a function of temperature by visual observation of the disappearing phase boundary. The phase boundaries were determined departing from the two-phase region to prevent measurement of a meta-stable phase. The cloud-points were determined with an absolute error of ± 1 bar in pressure and ± 0.03 K in temperature. The relative error in the amount of the components in the mixture is estimated to be less than 0.1 wt% for PEP and for ethylene, and less than 0.7 wt% for carbon dioxide.

Table 2.1 Poly(ethylene-co-propylene) molecular weights and composition.

PEP	M_n (kg/mol)	M_w (kg/mol)	Propylene (wt%)
Cloud-points[a]	51	120	0.54
Parameter fit[b]	52	134	0.57

[a]High temperature GPC experiments[20]. [b]Data Zoller and Walsh[25], M_w from light scattering experiments and M_w/M_n from GPC experiments.

2.3.3 Equilibrium calculations

Equilibrium calculations were performed using a standard Rachford-Rice flash algorithm, treating the polymer component as monodisperse. Starting with an initially guessed K value, phase compositions were determined using a mass balance solver. Subsequently, stable phase densities were determined using a volume solver. Based on these compositions and densities, the chemical potentials or fugacities of the components in each phase could be calculated. The criterion for equilibrium is given by

$$\mu_i^{II}(T,P,y) - \mu_i^{I}(T,P,x) = 0 \tag{2.26}$$

As long as Equation (2.26) is not satisfied to a specified tolerance, new K values were obtained from

$$\ln K_i^{n+1} = \ln K_i^n - \frac{1}{m}\left(\frac{\mu_i^{II}}{RT} - \frac{\mu_i^{I}}{RT}\right)^n \tag{2.27}$$

where m is the damping factor as proposed by Heidemann and Michelsen[22]. Similar equations were derived for calculations using fugacities.

2.3.4 Equation-of-state parameters

Calculation of phase equilibria using the Sanchez-Lacombe and SAFT models require pure component parameters and binary interaction parameters. Pure component parameters for light components were obtained by fitting vapor pressure data and liquid densities. Alternatively, parameters for the Sanchez-Lacombe eos can be determined from critical data and the acentric factor using a three-parameter corresponding states principle[23].

Pure component parameters for polymers are less easily determined. Commonly, the parameters are obtained from *PVT* data by a nonlinear fit of densities. Another approach for the SL parameters is a determination from the thermal expansion coefficient and the isothermal compressibility at given temperature, pressure and density. However, a fit of *PVT* data is preferred[24]. Parameters for the SAFT equation-of-state can be obtained by an extrapolation of the parameters of a homologous series of *n*-alkanes, as shown by Huang and Radosz[14]. The parameters used in the calculations are shown in Tables 2.2 and 2.3.

Table 2.2 SAFT pure component parameters.

Component	M (g/mol)	$u°/k$ (K)	$\upsilon°°$ (mL/mol)	m	e/k
Ethylene[14]	28.054	212.06	18.157	1.464	10
Carbon dioxide[14]	44.01	216.08	13.578	1.417	40
PEP[a,20]	51,000	469.86	21.618	0.034365 M	10
PEP[b,14]	51,000	210.00	12.000	0.050960 M	10

[a]Fit to densities from literature[25]. [b]Extrapolation of homologous series of *n*-alkanes[14].

Table 2.3 Sanchez-Lacombe pure component parameters.

Component	M (g/mol)	T^* (K)	P^* (bar)	ρ^* (kg/m^3)
Ethylene[35]	28.054	277.5	3401.5	668.2
Ethylene[a]	28.504	275.4	3057.5	588.9
CO_2[36]	44.01	305	5745	1510
CO_2[a]	44.01	274.8	6146.2	1403.9
PEP[b]	51,000	479.3	3497.7	945.3
PEP[c]	51,000	578.6	4590.5	919.9

[a]Derived from critical data and acentric factor[37]. [b]Fit to densities from literature[25]. [c]Derived from isothermal compressibility and thermal expansion coefficient approximated at 295 K and 1 bar[25].

The PEP pure component parameters were derived from literature *PVT* data[25]. Table 2.1 shows the molecular weights and compositions of the PEP used in the *PVT* studies and the PEP used for the cloud-point measurements.

2.4 Results and discussion

2.4.1 Experimental results

The experimental cloud-point curves for the system ethylene-PEP are presented in Figure 2.1. The system shows a decrease in cloud-point pressure upon an increase in temperature and polymer concentration. A similar trend has been observed for other nonpolar polymer-ethylene mixtures such as linear polyethylene in ethylene[21]. The pressure-composition sections show a slightly concave curvature, possibly due to the polydispersity of the sample.

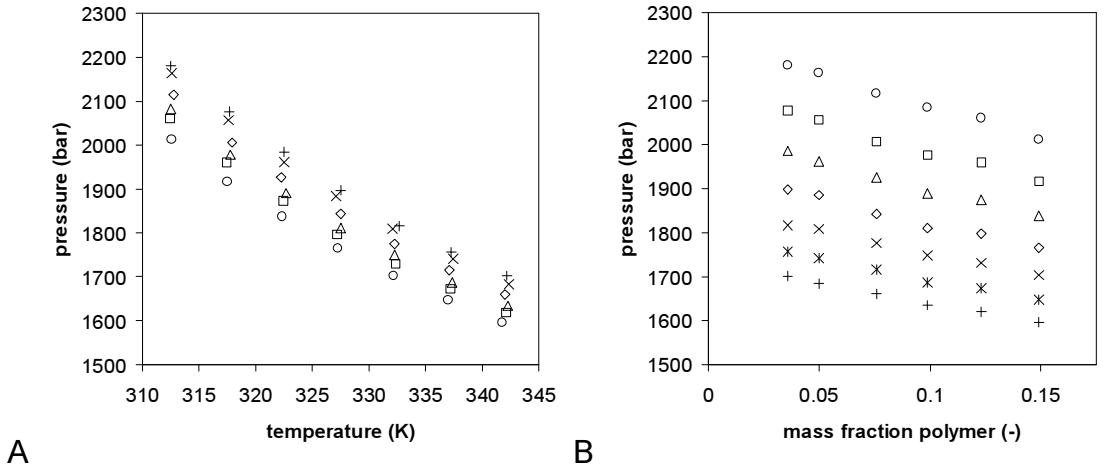

Figure 2.1 A) Pressure-composition sections for the ethylene-PEP systems at temperatures: o *= 312.6 K;* □ *= 317.6 K;* Δ *= 322.4 K;* ◊ *= 327.3 K;* × *= 332.3 K;* * *= 337.2 K;* + *= 342.1 K; B) Cloud-point measurements for the isopleths with weight fractions PEP:* + *= 0.0357;* × *= 0.0498;* ◊ *= 0.0756;* Δ *= 0.0989;* □ *= 0.1230;* o *= 0.1491.*

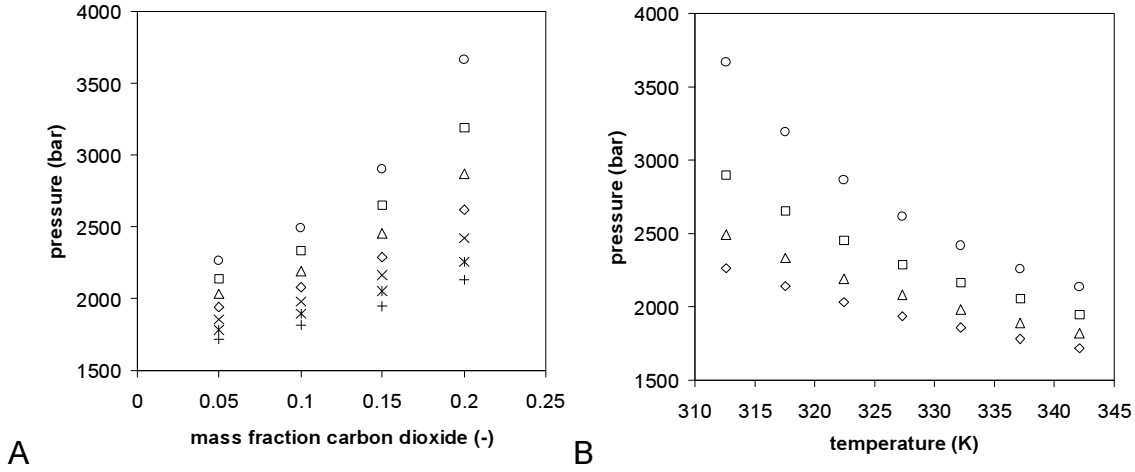

Figure 2.2 Antisolvent effect of CO_2 on a 10 wt% PEP solution in ethylene as a function of A) CO_2 content; o *= 312.6 K;* □ *= 317.6 K;* Δ *= 322.4 K;* ◊ *= 327.3 K;* o *= 332.3 K;* * *= 337.2 K;* + *= 342.1 K; B) temperature;* ◊ *= 0.05;* Δ *= 0.10;* □ *= 0.15;* o *= 0.20.*

The experimental cloud-point curves for the ternary system ethylene-PEP-carbon dioxide are presented in Figure 2.2. This figure shows a strong antisolvent effect of carbon dioxide, marked by a significant increase in cloud-point pressures upon addition of carbon dioxide. This effect is attributed to the lower polarizability and the higher quadrupole moment of carbon dioxide compared to ethylene. Both properties lower the dispersion interaction with the polymer. The

increased temperature sensitivity of the isopleths with increasing weight fraction CO_2 is caused by the higher quadrupole moment of CO_2. A quadrupole moment favors specific mutual interactions of the solvent, but levels off at higher temperatures.

2.4.2 Pure fluids

Thermodynamic modeling of phase equilibria requires model-specific pure component parameters. Various methods are available to determine these parameters, as previously mentioned. To check the validity of the obtained parameters, the thermophysical properties of ethylene and carbon dioxide along the saturation line have been investigated.

In Figure 2.3 the reduced vapor pressure curves and saturation curves of ethylene[26] as calculated by SAFT, SL using VLE-fit parameters and SL using critical data and the acentric factor, are shown. Using VLE-fit parameters, both SAFT and SL show a similar balanced description of vapor pressures and saturation densities. Therefore, the critical temperature is slightly overestimated, while the critical pressure is overestimated up to 20%. The SL model based on parameters derived from critical data and the acentric factor, forces the vapor pressure curve through the point at T_r = 0.7 and the critical point. This results in an excellent agreement for vapor pressures at the expense of the predicted liquid densities, due to the deviating curvature near the critical point. This is indicated

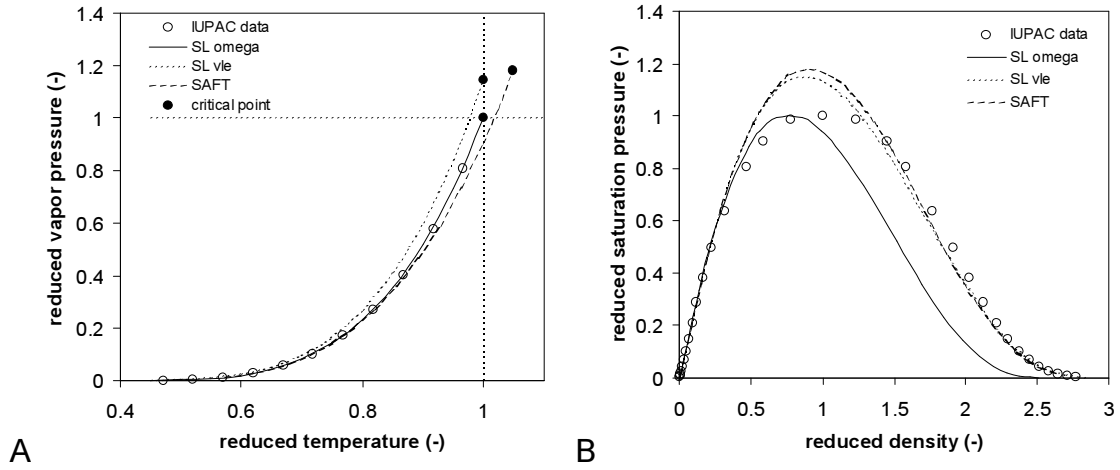

Figure 2.3 A) Reduced vapor pressure curve and B) saturation curve of ethylene[26] as compared to the modeling results for SAFT, SL using VLE-fit parameters and SL using critical data and the acentric factor ω.

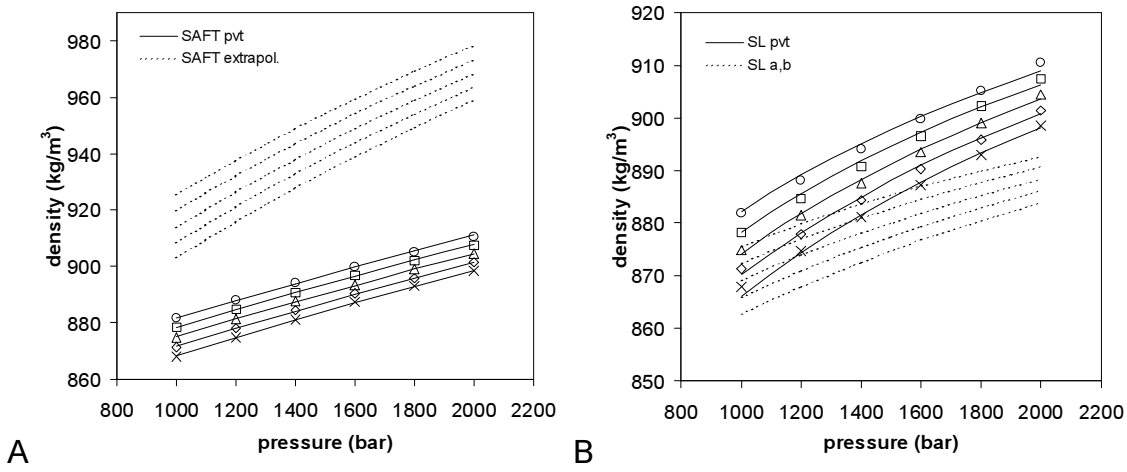

Figure 2.4 Densities of PEP and model predicted values for A) SAFT with PVT-*fit parameters and SAFT with parameters extrapolated from a homologous series of* n-*alkanes B) SL with* PVT-*fit parameters and SL with parameters derived from the thermal expansion coefficient* α *and the isothermal compressibility* β*.* o = *312.6 K;* □ = *320.7 K;* Δ = *329.1 K;* ◊ = *337.1 K;* × = *345.2 K.*

by the critical compressibility Z_c, a unique function of r, which varies between 0.333 and 0.386 for r in the range 0 to ∞. However, for most simple molecules, Z_c appears to be less than 0.3. The saturation curves for carbon dioxide[27] follow similar trends.

The modeling results of the volumetric properties of poly(ethylene-*co*-propylene) are shown in Figure 2.4. Using parameters fit to the *PVT* data, an excellent agreement is obtained for the SAFT model. Densities fit by the SL model start to deviate near the low pressure-high temperature and high pressure-low temperature limits. Description of the density of PEP with SAFT and *n*-alkane extrapolated parameters results in a significant overestimation of both volumetric temperature dependency and pressure dependency. Deriving SL parameters from α and β at 273 K and 1 bar, a good prediction of PEP densities is obtained at 1 bar over a wide temperature range. However, the densities are structurally underestimated at higher pressures, due to a deviation of the pressure dependency. In further calculations, only the parameters fit to VLE and *PVT* data are used.

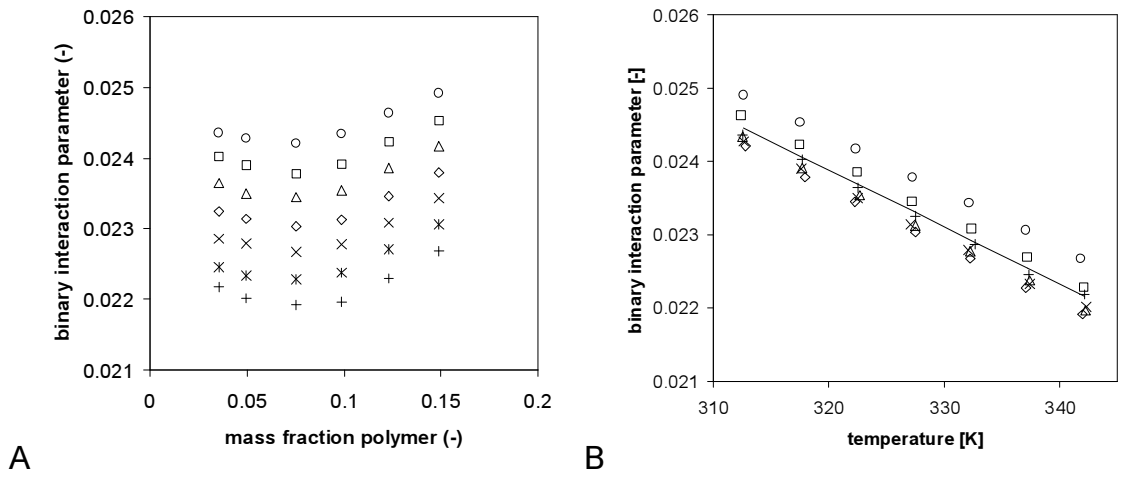

Figure 2.5 SL binary interaction parameters of the system ethylene-PEP as a function of A) mass fraction polymer, o *= 312.6 K;* □ *= 317.6 K;* Δ *= 322.4 K;* ◊ *= 327.3 K;* × *= 332.3 K;* * *= 337.2 K;* + *= 342.1 K; B) temperature,* + *= 0.0357;* × *= 0.0498;* ◊ *= 0.0756;* Δ *= 0.0989;* □ *= 0.1230;* o *= 0.1491.*

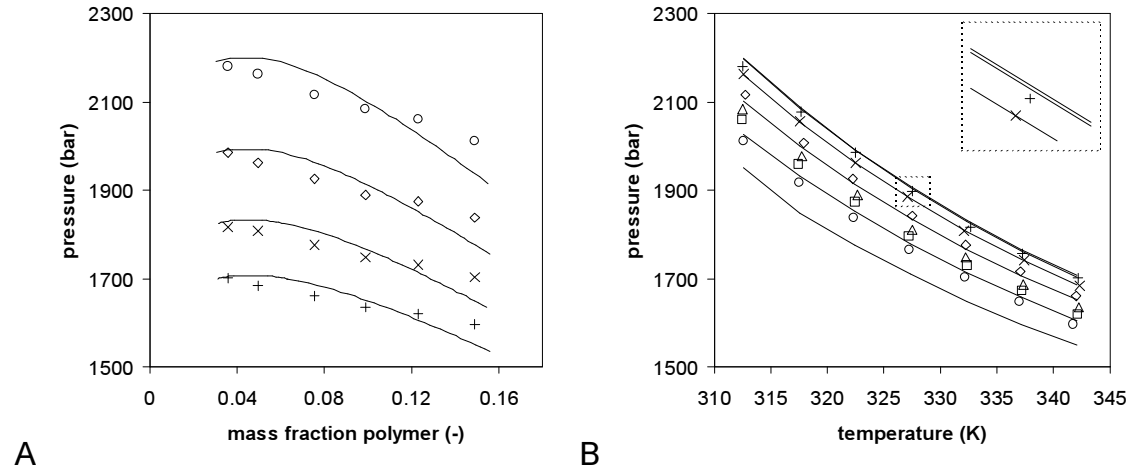

Figure 2.6 SL correlation of the cloud-point curves for the system ethylene-PEP as a function of A) temperature, o *= 312.6 K;* ◊ *= 322.4 K;* × *= 332.3 K;* + *= 342.1 K; B) PEP mass fractions,* + *= 0.0357;* × *= 0.0498;* ◊ *= 0.0756;* Δ *= 0.0989;* □ *= 0.1230;* o *= 0.1491. It should be noted that the SL model predicts a 0.0498 isopleth above the 0.0357 isopleth.*

2.4.3 Ethylene-PEP

The quantitative description of phase equilibria with SAFT and SL requires a binary interaction parameter per set of components. The binary interaction parameters needed for the description of the system ethylene-PEP, are determined

separately for each cloud-point. In Figure 2.5 the SL interaction parameters are shown as a function of cloud-point composition and temperature. The parameter shows a distinct concentration dependency, indicating a deviating description of cloud-point compositions. This can be attributed to the polydispersity of the polymer sample, which is not accounted for in the calculations. The cloud-points suggest a slightly concave curvature in the pressure-concentration diagram, possibly caused by measurements in the vicinity of the critical point. For model predictions of monodisperse polymers, a convex curve is obtained near the critical point. Although a spread in interaction parameters is observed due to the concentration dependency, a uniform linear temperature dependency can be fit, as shown in Figure 2.5b. The cloud-point curves are correlated using these linearly temperature-dependent interaction parameters, shown in Figure 2.6. As expected from the behavior of the interaction parameter, only a fair description of the cloud-point isotherms is obtained. Using a monodisperse polymer in the SL model results in a maximum in cloud-point pressure near 5 wt% PEP, which is not observed in the experimental data. In Figure 2.6b, this results in a 4.98 wt% isopleth *above* the 3.57 wt% isopleth.

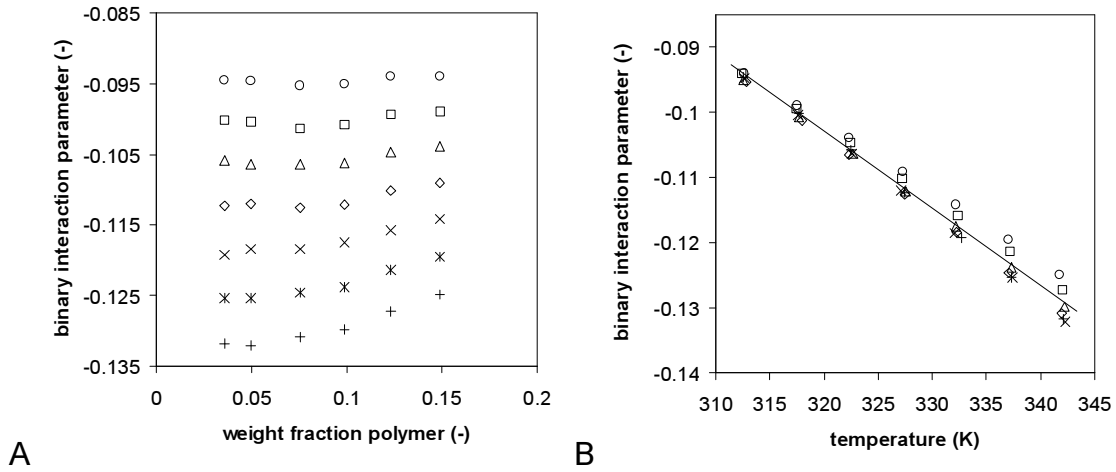

Figure 2.7 SAFT binary interaction parameters of the system ethylene-PEP as a function of A) mass fraction polymer, o *= 312.6 K;* □ *= 317.6 K;* Δ *= 322.4 K;* ◊ *= 327.3 K;* × *= 332.3 K;* * *= 337.2 K;* + *= 342.1 K; B) temperature,* + *= 0.0357;* × *= 0.0498;* ◊ *= 0.0756;* Δ *= 0.0989;* □ *= 0.1230;* o *= 0.1491.*

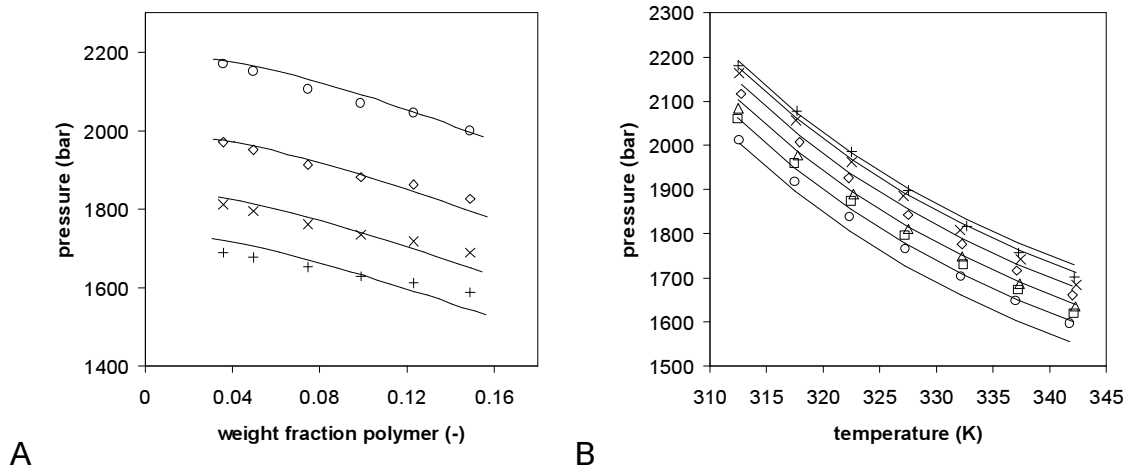

Figure 2.8 SAFT correlation of the cloud-point curves for the system ethylene-PEP as a function of A) temperatures, o *= 312.6 K;* ◊ *= 322.4 K;* × *= 332.3 K;* + *= 342.1 K; B) PEP mass fractions,* + *= 0.0357;* × *= 0.0498;* ◊ *= 0.0756;* Δ *= 0.0989;* □ *= 0.1230;* o *= 0.1491.*

Koak and Heidemann[28] have investigated the use of pseudo-components with SL for the description of polydispersity effects occurring in a solution of polyethylene in ethylene (M_w = 99,000, M_n = 56,000). Depending on the method of discretization of the mass distribution, between 12 and 18 pseudo-components are necessary to describe the experimentally observed phase behavior. Although assuming monodispersity, using a binary interaction parameter that is only linearly dependent on temperature results in a good description of the temperature dependency.

The SAFT binary interaction parameters fit to the ethylene-PEP cloud-point data are shown in Figure 2.7. At the lowest temperature, the interaction parameter is independent of the polymer concentration. However, with increasing temperature, the interaction parameter becomes increasingly more dependent on concentration. This results in a non-uniform temperature dependency, as shown in Figure 2.7b. For each polymer concentration, the interaction parameter can be described as a linear function of temperature. The results of the correlation of the cloud-point data with the SAFT model, using a mean slope for the linear temperature dependency, are shown in Figure 2.8. A reasonable agreement is obtained for the low temperature isotherms. At higher temperatures, an increasing deviation from the experimental data is observed. This corresponds directly with the concentration dependency of the interaction parameter at higher temperatures. An optimal description of the cloud-point pressures is obtained for the 9.89 wt% isopleth in Figure 2.8b. Here, the binary interaction parameters are in good

agreement with the linear temperature relation in Figure 2.7b. Under the assumption of monodispersity, the SAFT model predicts a critical point at lower polymer concentrations than the SL model. Therefore, no maximum in the cloud-point pressures is observed in the measured region, and a better correlation of the cloud-points is obtained. SAFT calculations with 36 polymer pseudo-components by Koak et al.[29] on the same ethylene-polyethylene solutions as mentioned in Koak and Heidemann[28], shows a significant improvement of the description of the cloud-point behavior. Predictive SAFT and SL cloud-point calculations by Xiong and Kiran[30] for *n*-pentane mixtures of various polyethylenes, show a similar advantage for SAFT.

2.4.4 Carbon dioxide-ethylene

Binary interaction parameters for the system carbon dioxide-ethylene are obtained from isothermal vapor-liquid equilibrium data[31-33]. In this system, an azeotrope is observed at temperatures below 283 K. The binary interaction parameter for SAFT is determined separately for each isotherm. With exception of the highest temperature near the critical point, excellent agreement between model and data is obtained, when using a binary interaction parameter depending linearly on the temperature. The binary interaction parameter for the SL model is less easily obtained. The SL model is not able to reproduce the azeotrope with a single binary interaction parameter per isotherm. Fitting a binary interaction parameter to each set of points on the demixing envelope, results in a wide spread

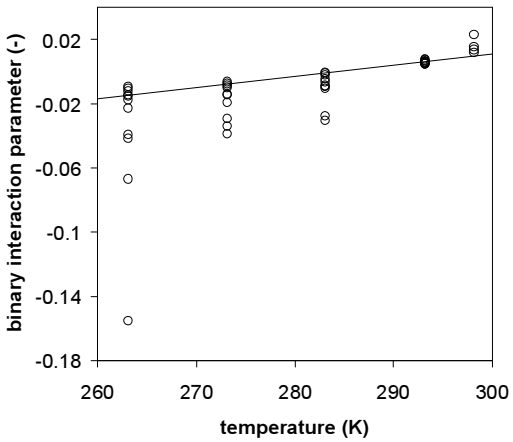

Figure 2.9 SL binary interaction parameters for the system carbon dioxide-ethylene. A linear temperature dependency is obtained from averages of the interaction parameters near the center of the demixing envelopes.

Table 2.4 Temperature dependence of binary interaction parameters

System	Binary interaction parameter[a]
SAFT	
Ethylene-PEP	$k_{12} = -1.1847 \cdot 10^{-3}\ T + 0.27616$
Ethylene-CO_2	$k_{13} = 4.91 \cdot 10^{-4}\ T - 0.0669$
PEP-CO_2	$k_{23} = -1.051 \cdot 10^{-3}\ T + 0.49373$
Sanchez-Lacombe	
Ethylene-PEP	$k_{12} = -7.7642 \cdot 10^{-5}\ T + 0.04873$
Ethylene-CO_2	$k_{13} = 7.1432 \cdot 10^{-4}\ T - 0.20304$
PEP-CO_2	$k_{23} = -0.18290$

[a]Temperatures in K

of values for each isotherm, as shown in Figure 2.9. To obtain a composition independent value, the binary interaction parameter is fit to the center of the demixing envelope at the carbon dioxide-rich side of the azeotrope, then a linear temperature dependency for the interaction parameter is obtained. In Table 2.4 the temperature dependency of the binary interactions for the SAFT and SL models is shown.

Description of the VLE data with SAFT and SL using these parameters is shown in Figure 2.10. The model predictions of SAFT are good agreement with the data, whereas the SL model is only able to describe the carbon dioxide-rich data.

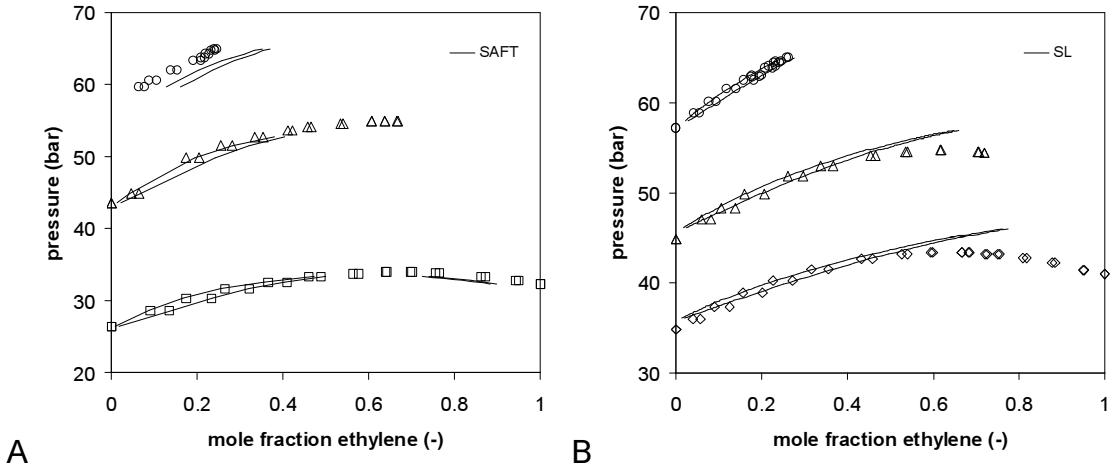

Figure 2.10 Carbon dioxide-ethylene vapor-liquid equilibrium as predicted by A) SAFT, o *= 293 K;* Δ *= 283 K;* □ *= 263 K; B) SL using PVT-fit parameters,* o *= 293 K;* Δ *= 283 K;* □ *= 273 K.*

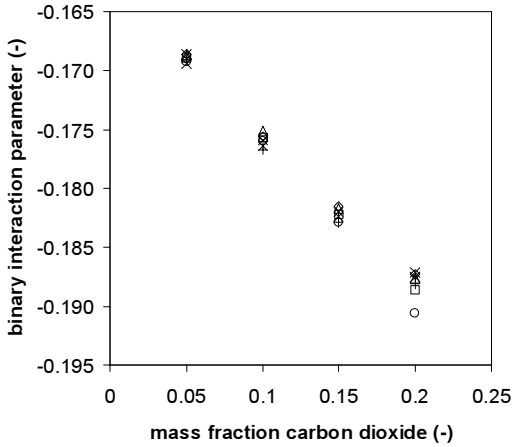

Figure 2.11 SL binary interaction parameters of the system carbon dioxide-PEP as obtained from the ternary system. Interaction parameters as a function of mass fraction carbon dioxide, o *= 312.6 K;* □ *= 317.6 K;* Δ *= 322.4 K;* ◊ *= 327.3 K;* × *= 332.2 K;* * *= 337.1 K;* + *= 342.1 K.*

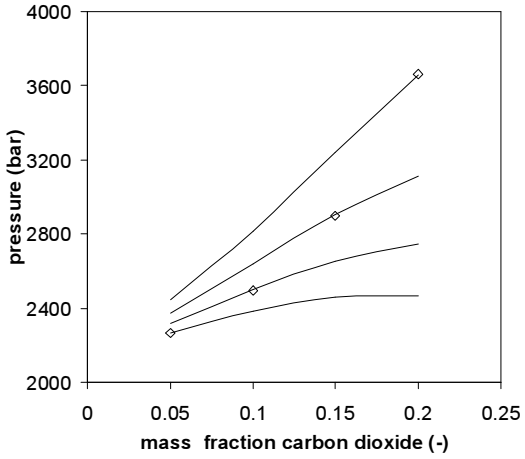

Figure 2.12 SL correlation of the cloud-point pressure as a function of CO_2 content at 312.6 K. Influence of k_{23} values fit to different CO_2 concentrations. SL correlations intersect with data at the fit CO_2 concentrations.

2.4.5 Carbon dioxide-ethylene-PEP

A last requirement for a description of the ternary system is the carbon dioxide-PEP binary interaction parameter. As PEP is insoluble in carbon dioxide at pressures within experimental reach, the interaction parameter is obtained from the ternary system consisting of 10 wt% PEP, carbon dioxide and ethylene. In Figure 2.11 the CO_2-PEP interaction parameters for the Sanchez-Lacombe model are shown as a function of carbon dioxide content and temperature. In contrast to the ethylene-PEP system, a strong concentration dependency is necessary to correlate the ternary system. On the other hand, it is justified to make the interaction parameter temperature independent. To avoid the use of a composition dependent interaction parameter, a fixed value is used. Figure 2.12 shows the influence of the k_{23} values on the correlation of the increase in cloud-point pressure by CO_2 at 312.6 K. The k_{23} value obtained from the 15 wt% CO_2 isopleth is selected, as this value results in the most balanced SL description of the cloud-points as a function of CO_2 content.

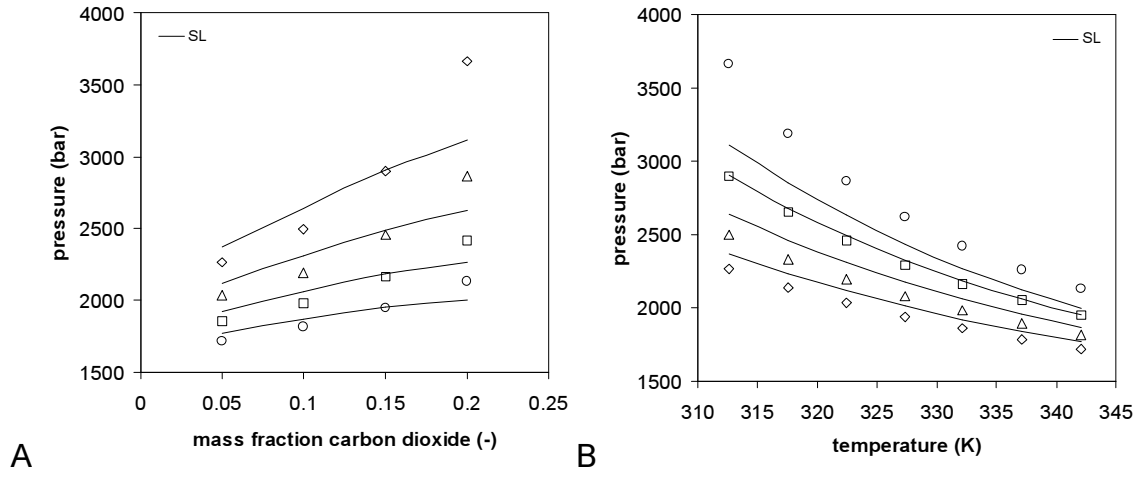

Figure 2.13 SL correlation of the cloud-point curves for the ternary system ethylene-carbon dioxide-PEP containing 10 wt% PEP as a function of A) carbon dioxide content, temperatures: ◊ = 312.6 K; Δ = 322.4 K; □ = 332.2 K; o = 342.1 K; and B) temperature, mass fractions carbon dioxide: ◊ = 0.05; Δ = 0.10; □ = 0.15; o = 0.20.

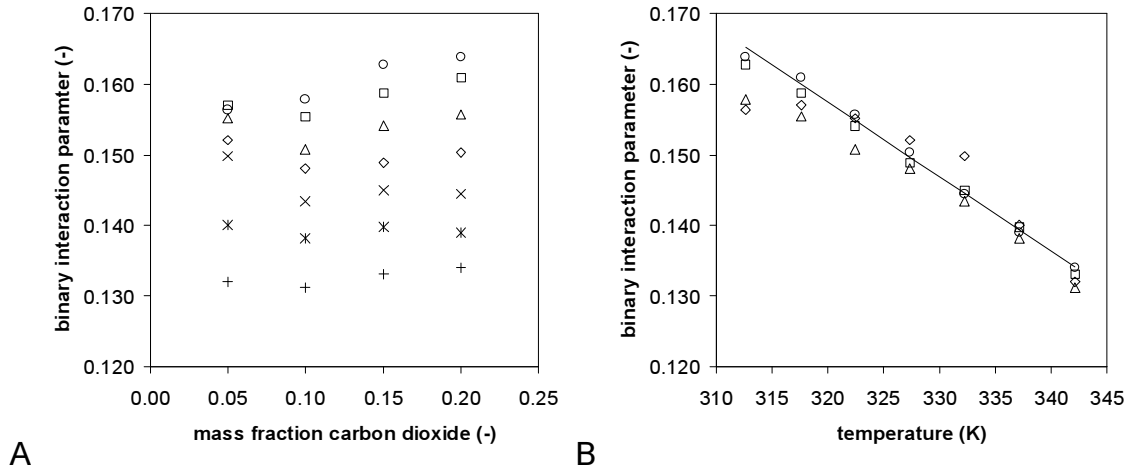

Figure 2.14 SAFT binary interaction parameters of the system carbon dioxide-PEP obtained from ternary system. Interaction parameters as a function of A) mass fraction carbon dioxide, o *= 312.6 K; □ = 317.6 K; Δ = 322.4 K; ◊ = 327.3 K; × = 332.2 K; * = 337.1 K; + = 342.1 K; B) temperature, ◊ = 0.05; Δ = 0.10; □ = 0.15;* o *= 0.20.*

Using the three binary interaction parameters given in Table 2.4, the SL correlation of the antisolvent effect of CO_2 on the cloud-point curves for the ternary system is shown in Figure 2.13. Taking into account the strong concentration dependency of the binary interaction parameter, a reasonable description of the increase in cloud-points due to CO_2 is obtained. Regardless of

the value of k_{23}, SL predicts an increase in cloud-point pressures upon addition of CO_2. At higher concentrations, this increase levels off, in contrast to the experimental data, which show a progressive increase in cloud-point pressure. The SL model yields an excellent description of the temperature dependency of the antisolvent effects of CO_2, as is seen for the 15 wt% CO_2 isopleth in Figure 2.13b. As shown by Martin et al.[34], in the system *n*-pentane-polypropylene the SL model is capable of a accurate description of the antisolvent effect of carbon dioxide, both in terms of temperature and composition. The SL model is able to describe the binary system *n*-pentane-CO_2 well. The rather poor description of the ethylene-PEP-CO_2 system in terms of CO_2 content is possibly caused by the inability of the SL model to accurately describe the phase behavior of the ethylene-CO_2 subsystem.

The SAFT CO_2-PEP binary interaction parameters fit to each composition and temperature are shown in Figure 2.14. The interaction parameter decreases with increasing temperature for all CO_2 concentrations. At lower temperatures, k_{23} tends to vary with CO_2 concentration. As the calculated cloud-points at high CO_2 concentrations are significantly more sensitive to k_{23} than at low concentrations, the 20 wt% isopleth is used for a linear fit of k_{23}. The calculated cloud-points for the ternary system are shown in Figure 2.15. The SAFT model, using the interaction parameters obtained above, gives an excellent description of the antisolvent effects of carbon dioxide on the ethylene-PEP system, both in terms of CO_2 content and in temperature.

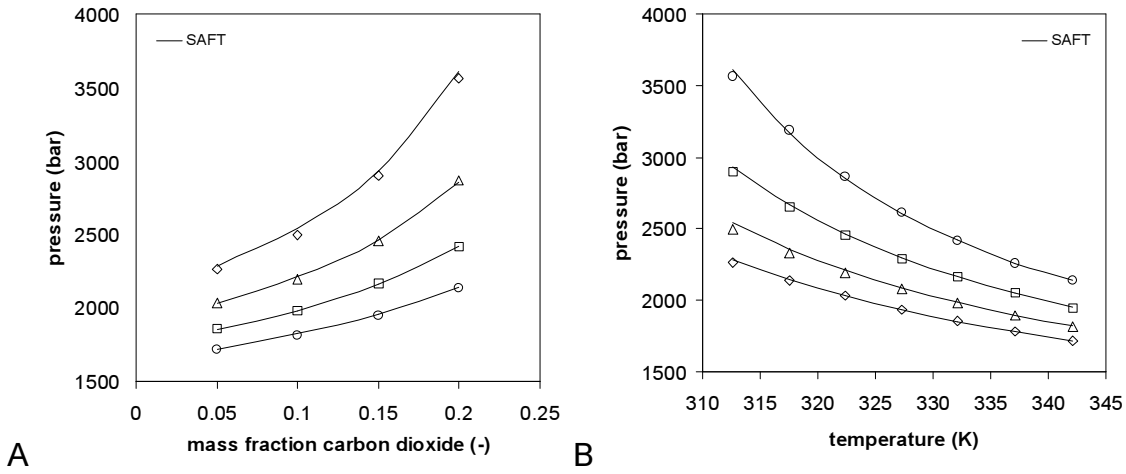

Figure 2.15 SAFT correlation of the cloud-point curves for the ternary system ethylene-carbon dioxide-PEP containing 10 wt% PEP as a function of A) carbon dioxide content, temperatures: ◊ = 312.6 K; Δ = 322.4 K; □ = 332.2 K; o = 342.1 K; and B) temperature, mass fractions carbon dioxide: ◊ = 0.05; Δ = 0.10; □ = 0.15; o = 0.20.

2.5 Concluding remarks

It is shown that both the SAFT and the Sanchez-Lacombe model correlate the qualitative aspects of the antisolvent effects of carbon dioxide on a polymer-SCF system like ethylene-PEP. For a quantitative description of the phase behavior, temperature-dependent interaction parameters are required. These must be obtained from experimental data. For light components, VLE data are readily available. However, for polymer-solvent systems suitable data are scarcer. In addition, for systems containing polymers, the molecular weight and the polydispersity of the polymer should be taken into account. The SL model has the advantage that it is very tractable and it is suitable for interpolation of data. On the other hand, the SL model yields a poor description of systems containing specific interactions, which is rather visible in the description of the subsystem CO_2-ethylene. The SL model is a mean-field theory, with mixing rules assuming a random mixture, so that specific interactions can only be introduced through a temperature-dependent interaction parameter. The SAFT model does take into account specific interactions between components, at the expense of computational complexity. Similar to the Sanchez-Lacombe eos, the SAFT eos is also ill suited for the prediction of SCF-polymer phase behavior, as it also needs interaction parameters, however, it does yield a considerably better correlation of experimental data.

2.6 References

1. A.I. Cooper, *J. Mat. Chem.* **10** (2000) 207.
2. J.L. Kendall, D.A. Canelas, J.L. Young and J.M. DeSimone, *Chem. Rev.* **99** (1999) 543.
3. T.J. de Vries, R. Duchateau, M.A.G. Vorstman and J.T.F. Keurentjes, *Chem. Comm.* (2000) 263.
4. J.M. de Gooijer, A. de Haan, M. Scheltus, L. Schmieder-v.d. Vondervoort and C. Koning, *Polymer* **40** (1999) 6493.
5. H.J. Hayes and T.J. McCarthy, *Macromolecules* **31** (1998) 4813.
6. M.A. McHugh and V.J. Krukonis, *Supercritical Fluid Extraction: Principles and Practice*, Butterworth Heinemann, Boston, 1994.
7. S. Kim, Y.S. Kim and S.B. Lee, *J. Supercrit. Fluids* **13** (1998) 99.
8. J.W. Tom and P.G. Debenedetti, *Biotechnol. Prog.* **7** (1991) 403.
9. S. Mawson, K.P. Johnston, J.R. Combes and J.M. DeSimone, *Macromolecules* **28** (1995) 3182.
10. I.C. Sanchez and R.H. Lacombe, *J. Phys. Chem.* **80** (1976) 2352.
11. R.H. Lacombe and I.C. Sanchez, *J. Phys. Chem.* **80** (1976) 2568.

12. I.C. Sanchez and R.H. Lacombe, *Macromolecules* **11** (1978) 1145.
13. I.C. Sanchez, In *Encyclopedia of Physical Science and Technology*, 2nd edition, vol. 13, p. 153, Academic Press, Boston, 1992.
14. S.H. Huang and M. Radosz, *Ind. Eng. Chem. Res.* **29** (1990) 2284.
15. S.H. Huang and M. Radosz, *Ind. Eng. Chem. Res.* **30** (1991) 1994.
16. S.H. Huang and M. Radosz, *Ind. Eng. Chem. Res.* **32** (1993) 762.
17. B. Bungert, G. Sadowski and W. Artl, *Fluid Phase Equilibria* **139** (1997) 349.
18. E. Reverchon, *J. Supercrit. Fluids* **15** (1999) 1.
19. M. Kemmere, T. de Vries, M. Vorstman and J. Keurentjes, *Chem. Eng. Sci.* **56** (2001) 4197.
20. T.J. de Vries, P.J.A. Somers, Th.W. de Loos, M.A.G. Vorstman and J.T.F. Keurentjes, *Ind. Eng. Chem. Res.* **39** (2000) 4510.
21. Th.W. de Loos, W. Poot and G.A.M. Diepen, *Macromolecules* **16** (1983) 111.
22. R.A. Heidemann and M.L. Michelsen, *Ind. Eng. Chem. Res.* **34** (1995)958.
23. K. Gauter and R.A. Heidemann, *Ind. Eng. Chem. Res.* **39** (2000) 1115.
24. I.C. Sanchez and R.H. Lacombe, *Polym. Letters* **15** (1977) 71.
25. P. Zoller and D.J. Walsh, *Standard Pressure-Volume-Temperature Data for Polymers*, Technomic Publishing, Lancaster, 1995.
26. S. Angus, B. Armstrong and K.M. de Reuck, *International Tables of the Fluid State. Ethylene*, Pergamon Press, Oxford, 1972.
27. S. Angus, B. Armstrong and K.M. de Reuck, *International Tables of the Fluid State. Carbon Dioxide*, Pergamon Press, Oxford, 1976.
28. N. Koak and R.A. Heidemann, *AIChE J.* **47** (2001) 1219.
29. N. Koak, R.M. Visser and Th.W. de Loos, *Fluid Phase Equilibria* **158-160** (1999) 835.
30. Y. Xiong and E. Kiran, *J. Appl. Polym. Sci.* **55** (1995) 1805.
31. H.K. Bae, K. Nagahama and M. Hirata, *J. Chem. Eng. Data* **27** (1982) 25.
32. G.G. Haselden, D.M. Newitt, F.R.S. Shah and S.M. Shah, *Proc. Royal Soc. London A* **209** (1951) 1.
33. G.G. Haselden, F.A. Holland, M.B. King and R.F. Strickland-Constable, *Proc. Royal Soc. London A* **240** (1957) 1.
34. T.M. Martin, *Fluid Phase Equilibria* **154** (1999) 241.
35. D.S. Pope, I.C. Sanchez, W.J. Koros and G.K. Fleming, *Macromolecules* **24** (1991) 1779.
36. M.B. Kiszka, M.A. Meilchen and M.A. McHugh, *J. Appl. Polym. Sci.* **36** (1988) 583.
37. R.C. Reid, J.M. Prausnitz and B.E. Poling, *The Properties of Gases and Liquids*, 4th edition, McGraw-Hill, New York, 1987.

CHAPTER 3

FOAM PROCESSING OF POLY(ETHYLENE-*CO*-VINYL ACETATE) RUBBER USING SUPERCRITICAL CARBON DIOXIDE

Abstract

Soft rubber foams like poly(ethylene-*co*-vinyl acetate) (EVA) are industrially applied in a broad range of products, including sports gear, insulation materials and drug delivery systems. In contrast to glassy polymers, few studies in literature concern the foaming of soft rubbers using supercritical carbon dioxide. In this study, open microporous matrices of EVA have been formed using supercritical carbon dioxide. Prior to the foam expansion, sorption and swelling isotherms of carbon dioxide in EVA have been measured and the obtained isotherms have been correlated using the Sanchez-Lacombe equation-of-state. Additionally, a pressure-independent diffusion coefficient of CO_2 in EVA has been obtained from these experiments. The open microporous foams have been formed by a pressure quench of the carbon dioxide-swollen polymer matrix. Sorption pressure as well as temperature and decompression times appear to control the pore size and bulk density of the foam. Increasing the sorption pressure or decompression rate produces more dense foams with a smaller pore size. Although higher sorption temperatures also reduce the pore size, the processing temperature is limited by the melting point of the polymer. In summary, supercritical carbon dioxide allows for a control of the foam structure of EVA rubbers, which is advantageous for specialty applications such as biological scaffolds and drug delivery systems.

This chapter has been submitted as: M.A. Jacobs, M.F. Kemmere and J.T.F. Keurentjes, Foam processing of poly(ethylene-co-vinyl acetate) rubber using supercritical carbon dioxide.

3.1 Introduction

Microcellular polymeric foams are usually defined as foams with a cell size less than 10 μm[1]. Applications of microcellular polymers are widespread and include thermal and electrical insulation, adsorbents, separation membranes, catalyst supports and controlled drug release devices. Traditionally, polymers are foamed in a variety of ways. The most common techniques are the foaming by thermally induced phase separation (TIPS) and the use of chemical foaming agents (CFA) in the extrusion process of rubbers. In the TIPS process the polymer is dissolved in an appropriate organic solvent, forming a single-phase solution at an elevated temperature. Subsequently, a phase separation is induced by a temperature quench. After careful removal of the solvent either by freeze-drying or supercritical extraction, a microporous polymer matrix is obtained. A drawback of this method is possible structure coarsening due to temperature gradients during phase separation and the occurrence of surface forces during the solvent removal. The TIPS process is applied in the production of foams from many glassy polymers, e.g. in foaming of polystyrene using pentane as the solvent[2].

A common technique for the foaming of rubbery and low-melting polymers is the application of chemical foaming agents in extrusion of these polymers. A foaming agent consists of an organic or inorganic thermally unstable component, which decomposes to gaseous components upon heating above a certain temperature. In the foam processing of polymers such as polyethylene (PE), polypropylene (PP), poly(ethylene-*co*-vinyl acetate) (EVA) and poly(vinyl chloride) (PVC), the main component in commonly used foaming agents is azodicarbonamide. Although azodicarbonamide itself is relatively harmless, the decomposition products are less benign. Besides nitrogen and carbon dioxide, the decomposition gas consists of approximately 32 vol% carbon monoxide and up to 1 vol% ammonia[3]. During the decomposition of azodicarbonamide approximately 68 wt% of the azodicarbonamide is converted to solid residue and sublimate, which remain in the polymer matrix.

In recent years, the application of supercritical fluids (SCFs) in the production of microporous foams from glassy polymers has been widely studied[4]. Supercritical fluids, in particular carbon dioxide, possess many advantageous properties, which enable their use as foaming agents. These include a tunable solvent strength, plasticization of glassy polymers and enhanced diffusion rates. Furthermore, the low critical temperature of carbon dioxide allows for an easy and complete separation from the polymer, without encountering a vapor-liquid

transition during the expansion. Additionally, carbon dioxide is, besides being environmentally benign, readily applicable as a solvent in pharmaceutical and food processes as it has a GRAS-status (generally regarded as safe).

Most research on the foaming of polymers using supercritical carbon dioxide has been focused on glassy polymers as poly(methyl methacrylate) (PMMA), polystyrene (PS), polyethylene therepfthalate (PET) and polycarbonate (PC)[2,5-7]. To investigate the use of carbon dioxide as an alternative to CFAs in the processing of rubbery polymers, we have applied the foaming technique described by Goel and Beckman[2,5] for the foaming of EVA. Foamed EVA is widely used in products ranging from shoe soles, sports gear, insulation material, packaging and wrapping material to toys. Additionally, the biocompatible character of EVA allows for applications in drug delivery systems[8,9].

In this work, the foaming of rubbery EVA with supercritical carbon dioxide has been investigated. The influence of sorption pressure, temperature and decompression rates on the foam morphology is reported. Additionally, the sorption and swelling behavior and the diffusion rates of carbon dioxide in EVA have been measured. The obtained isotherms are correlated using the Sanchez-Lacombe equation-of-state.

3.2 Experimental

3.2.1 Materials

Poly(ethylene-co-vinyl acetate) with 40 wt% vinyl acetate (EVA-40) was purchased from Aldrich Chemical Company. GPC analysis with polystyrene standards indicated an M_n of 55,000 g/mol and a polydispersity of 2.3. The glass transition temperature and the melting temperature, as determined by DSC analysis, revealed a glass transition temperature of 235 K and two melting temperatures at 328 K and 342 K, respectively. ^{1}H NMR analysis of the EVA showed a copolymer composition of 38 ± 1 wt% VA. Carbon dioxide (grade 4.5) was obtained from Hoekloos (Amsterdam, The Netherlands) and was used without further purification.

3.2.2 Sorption and expansion experiments

Sorption and expansion experiments were performed in a stainless steel high-pressure micro-vessel (total pressurized volume, including tubing, 5.62 mL), equipped with a pressure indicator (PDCK, ± 1 bar). The temperature was controlled using a thermostat bath (Lauda, ± 0.5 K). The experimental setup is

schematically shown in Figure 3.1a.

Sorption levels were determined using the pressure decay method. For this purpose, a weighted amount of spherical EVA pellets was loaded in the vessel and was equilibrated in the thermostat bath for 2 hours before pressurization with carbon dioxide. The sorption level was determined from the difference between the initial pressure and the pressure at equilibrium, the volume of the system and the initial mass of the sample. The diffusion coefficients for carbon dioxide in EVA, assuming sphere geometry, were obtained from the sorption rates. To determine diffusion in plane sheet geometry, plane sheet samples were formed from the spherical pellets by melting under vacuum at 425 K for several hours. The same pressure decay method was applied on these samples.

Microporous structures were produced by rapid expansion of the swollen polymer beads in equilibrium with CO_2. Expansions were performed starting with polymers equilibrated at various temperatures and pressures. The polymers were expanded at various rates, while the samples were unrestricted during the expansion. The expansion rates were controlled using a needle valve, except for the rapid expansion experiments (< 2 s), which were initiated by fast opening of a ball valve.

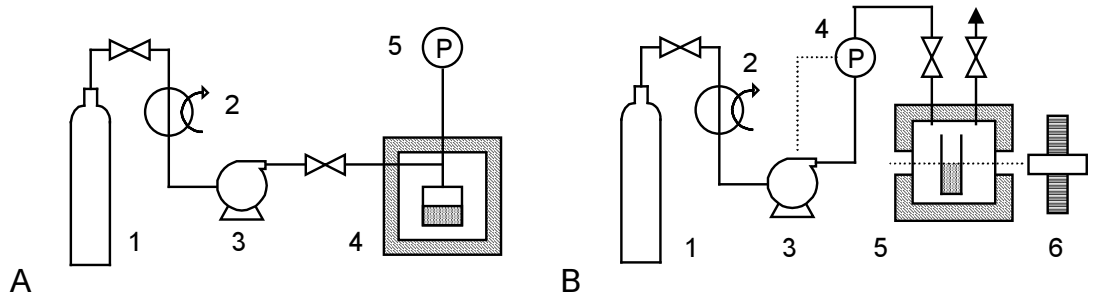

Figure 3.1 Schematic representation of A) sorption equipment with 1) carbon dioxide feed; 2) feed cooling; 3) HPLC pump; 4) high-pressure microcell in thermostat bath; 5) pressure indicator, and B) swelling equipment with 1) carbon dioxide feed; 2) feed cooling; 3) HPLC pump; 4) pressure controller; 5) high-pressure view cell with heating jacket; 6) cathetometer.

3.2.3 Swelling experiments

Swelling experiments were performed in a high-pressure view cell (24 mL), equipped with two opposite sapphire windows and a Pt-100 resistance thermometer. The temperature was controlled using an electrical heating jacked

connected to a resistance thermometer (± 1 K). The pressure was controlled within 1 bar using an HPLC pump equipped with a pressure module (Gilson, ± 1 bar). The height of the meniscus of the polymer liquid was measured using a cathetometer (Precision Tool & Instrument, ± 0.02 mm). The experimental setup is schematically shown in Figure 3.1b.

A weighted amount of EVA pellets was loaded in a calibrated cylindrical glass sample holder. Prior to use, the polymer samples were molten under vacuum at 425 K for several hours. Subsequently, the sample holder was placed in the view cell and was preheated at the desired temperature. After equilibrating the sample for 30 minutes, the initial height of the liquid polymer meniscus was recorded. Subsequently, a constant carbon dioxide pressure was applied and the swelling of the liquid polymer was measured by recording the height of the meniscus in time.

3.2.4 Sanchez-Lacombe equation-of-state

The experimental sorption and swelling isotherms were correlated with the Sanchez-Lacombe equation-of-state (SL eos)[10-12]. The SL eos is based on classical lattice-fluid theory extended with vacancies in the lattice in order to account for compressibility. The equation-of-state, expressed in reduced parameters, is given by

$$\tilde{\rho} + \tilde{P} + \tilde{T}\left[\ln(1-\tilde{\rho}) + \left(1-\frac{1}{r}\right)\tilde{\rho}\right] = 0 \qquad (3.1)$$

in which $\tilde{\rho}$, $\tilde{P}$ and $\tilde{T}$ are the reduced density, pressure and temperature, respectively, and r is a parameter specifying the number of lattice sites occupied by the molecule.

Table 3.1 Sanchez-Lacombe eos pure component parameters.

Parameter	Carbon dioxide[29]	EVA-40[a]
M (kg/mol)	0.044	55
T^* (K)	305	613
P^* (bar)	5745	4956
ρ^* (kg/m^3)	1510	1020

[a]Parameters obtained from a fit to densities from literature data[14] in the range 1-400 bar and 334-400 K.

A pure fluid is characterized by three lattice parameters, which can be regrouped to a characteristic temperature, pressure and density. The characteristic parameters for carbon dioxide and EVA-40 are obtained from VLE data and PVT data, respectively, and are given in Table 3.1. Extension to mixtures is accomplished by applying appropriate mixing rules. For each set of components, a single binary interaction parameter is introduced, which is obtained from a fit to the sorption data.

3.2.5 Diffusion coefficients

The diffusion coefficients of carbon dioxide in EVA were calculated from the sorption and swelling rates as obtained by the methods described above. For symmetric Fickian diffusion in a plane sheet with a uniform initial distribution and constant surface concentrations, the relative sorption rate is given by[13]

$$\frac{M_t}{M_\infty} = 1 - \frac{8}{\pi^2}\sum_{n=0}^{\infty}\frac{1}{(2n+1)^2}\exp\left(-(2n+1)^2\pi^2\frac{Dt}{4L^2}\right) \tag{3.2}$$

where M_t and M_∞ are mass uptakes at time t and at equilibrium, D is the diffusion coefficient and L is the thickness of the sheet. Equivalently, the relation for sphere geometry is given by

$$\frac{M_t}{M_\infty} = 1 - \frac{6}{\pi^2}\sum_{n=0}^{\infty}\frac{1}{n^2}\exp\left(-n^2\pi^2\frac{Dt}{r^2}\right) \tag{3.3}$$

where r is the radius of the sphere. These equations are valid under the assumption of constant diffusion length scales L and r. In practice the polymer system swells as the vapor enters, which leads to an increased diffusion length scale. Equations (3.2) and (3.3) can still be used in that case, provided that a frame of reference fixed with respect to the polymer dimensions is taken[13]. Concentrations and diffusion length scales in these units are thus independent of the swelling. The diffusion coefficient obtained is that of the vapor relative to the stationary polymer. In the case of zero excess volume of mixing, the mutual diffusion coefficient D^V is related to D by[13]

$$D = D^V(1-\phi_V)^2 \tag{3.4}$$

where ϕ_V is the volume fraction of the vapor. To enable calculation of diffusion coefficients from swelling rates, the amount of transferred substance for swelling is approximated by

$$\frac{M_t}{M_\infty} = \frac{V_t - V_0}{V_\infty - V_0} \tag{3.5}$$

3.2.6 Structure characterization

The foams were characterized to determine the cell size, cell shape and bulk density. The cell structure was determined by Scanning Electron Microscopy (Jeol), after cryofracturing and sputter coating of the sample with a gold layer of approximately 55 nm. Bulk foam density, porosity and pore diameters were determined using mercury intrusion porosimetry (Micromeritics). The bulk densities were obtained by

$$\rho_{bulk} = \frac{m}{V_{intr} + mV_{sp}} \tag{3.6}$$

where m is the sample mass, V_{intr} the total intrusion volume and V_{sp} is the specific volume of the unfoamed polymer at intrusion temperature and pressure obtained from literature[14].

3.3 Results and discussion

3.3.1 Sorption and swelling

A prerequisite for the preparation of microporous polymer matrices using carbon dioxide is a sufficient solubility of the gas in the polymer. Sorption and swelling levels for EVA containing 40 wt% vinyl acetate are shown in Figure 3.2 for 323 K and 348 K, respectively. The sorption and swelling isotherms show a gradual increase at both temperatures, with higher sorption and swelling levels at the lower temperature. Sorption of carbon dioxide in polymers depends strongly on specific interactions with carbon dioxide as exhibited by polymers containing fluorinated side groups, siloxane-type backbones, and carbonyl and phenyl groups[15-17]. However, no specific interactions have been observed for polyolefins. Sorption levels of carbon dioxide in EVA will thus strongly depend on the amount of vinyl acetate incorporated in the polymer. A progressive increase in carbon dioxide sorption in EVA copolymers with vinyl acetate contents ranging from 18 to 27 wt% has been shown by Shieh et al.[18]. The observed sorption levels determined for EVA-40, however, are significantly higher than the sorption levels measured by Shieh et al. Extrapolation of these data at 305 K and 250 bar to a polymer composition of 40 wt% VA would result in a sorption level of approximately 37 wt% CO_2. As shown in Figure 2a, at 323 K and 236 bar a content

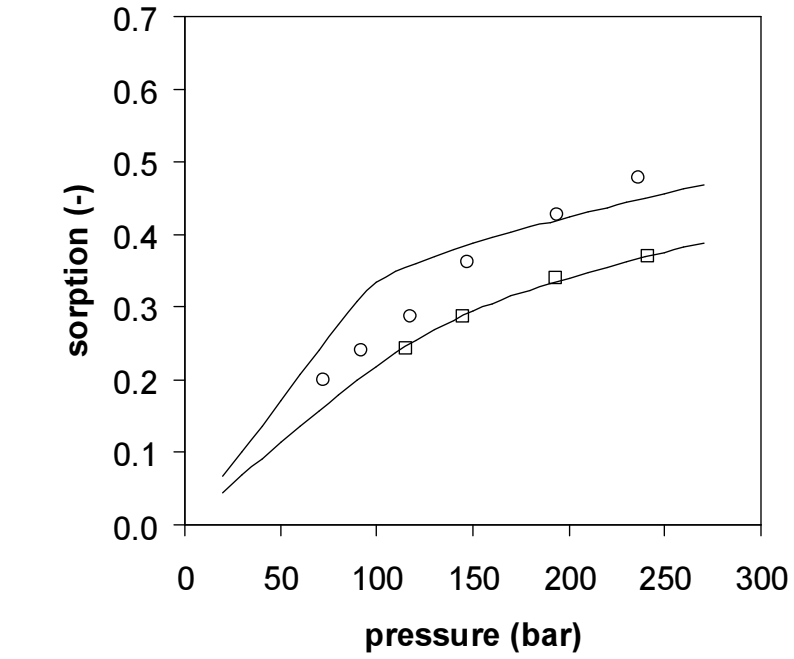

A

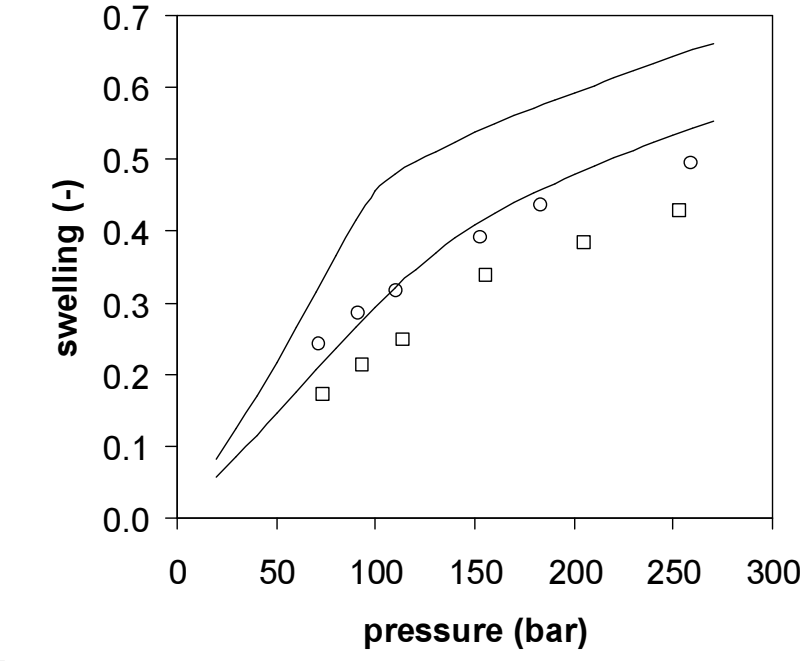

B

Figure 3.2 Sorption and swelling isotherms of carbon dioxide in EVA 40 wt% VA at 323 K and 348 K; A) sorption isotherms; B) swelling isotherms; o *323 K;* □ *348 K;* — *Sanchez-Lacombe model calculations with binary interaction parameter* k_{12} *= −0.00823 obtained from a fit of the sorption data at 348 K.*

of 48 wt% CO_2 is obtained. At 305 K, this value will be even higher. This shows a clear non-linear relation between sorption and copolymer composition, as it has been observed for block copolymers before[19].

The swelling of EVA-40 in carbon dioxide, presented in Figure 3.2b, shows a similar behavior as the sorption curves. The degree of swelling is in the same order as the sorption level, with a maximum value of 49 vol% at 323 K and 259 bar. In many cases the swelling degree exceeds the sorption amount, although the reverse has also been observed, e.g. in polycarbonate[20]. Swelling data, usually obtained from dilation of polymer films, show a substantial uncertainty, as illustrated in the following for PMMA. Kamiya et al.[22] show a swelling of 13 vol% at 308 K and 52 bar, slightly lower than the sorption level of 14 wt%. However, Wissinger and Paulaitis[21] as well as Liau and McHugh[23] report a swelling level lower than the sorption level. At 315 K and 51 bar, both papers report a swelling of 10 vol%, whereas sorption levels of 11 wt% and 14 wt% are shown, respectively. At 101 bar, the differences between the reported swelling levels become significantly large, with values of 28 vol% and 13 vol%, respectively.

The correlation of the sorption data with the SL eos is shown in Figure 3.2a as solid lines. At 323 K a rather sharp transition region is visible around 100 bar in the SL model lines. This corresponds to a steep CO_2 density gradient caused by the overestimation of the critical point by 16.6 K, placing it at 320.7 K. To compensate this effect, the binary interaction parameter is obtained from a fit of the sorption data at 348 K and has a value of $k_{12} = -0.00823$. Using this value, a fair description of the sorption data at 323 K is obtained. For the swelling similar trends are observed, although with a consistent overestimation of the swelling by approximately 25%.

3.3.2 Diffusion

In Figure 3.3a the relative amounts of carbon dioxide diffused into EVA are plotted against the square root of time for the measurements at 323 K and 150 bar, derived from both sorption and swelling data. Initially, the data show a linear increase, confirming Fickian diffusion behavior. A least square fit of the sorption and swelling data to Equations (3.2) and (3.3) results in apparent diffusion coefficients of carbon dioxide in EVA, which are shown in Figure 3.3b. The diffusion coefficients determined from the sorption curves at 323 K are independent of pressure and have values around 6×10^{-10} m^2/s, which is comparable to PBMA at the same temperature[24] (7.1×10^{-10} m^2/s). The diffusion coefficients determined from the swelling experiments have higher values, around 1×10^{-9} m^2/s,

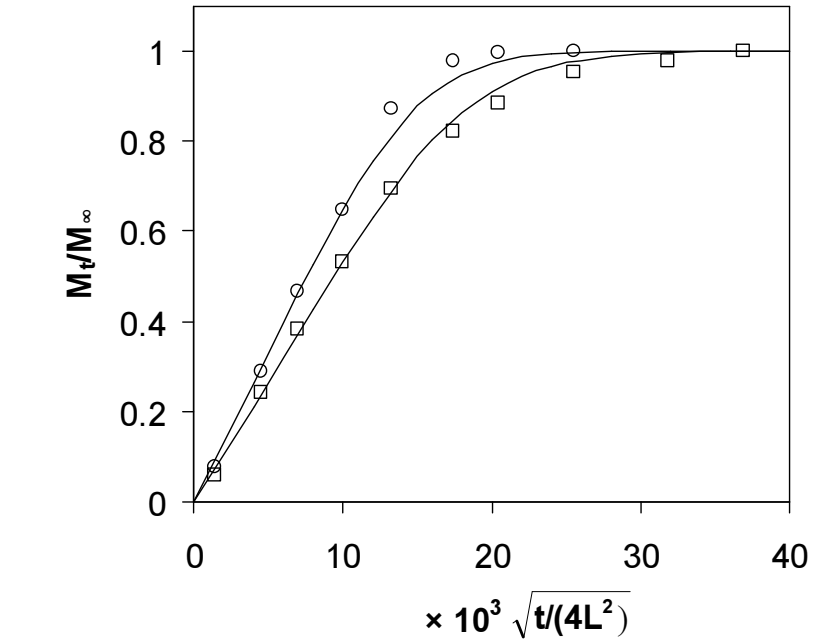

A

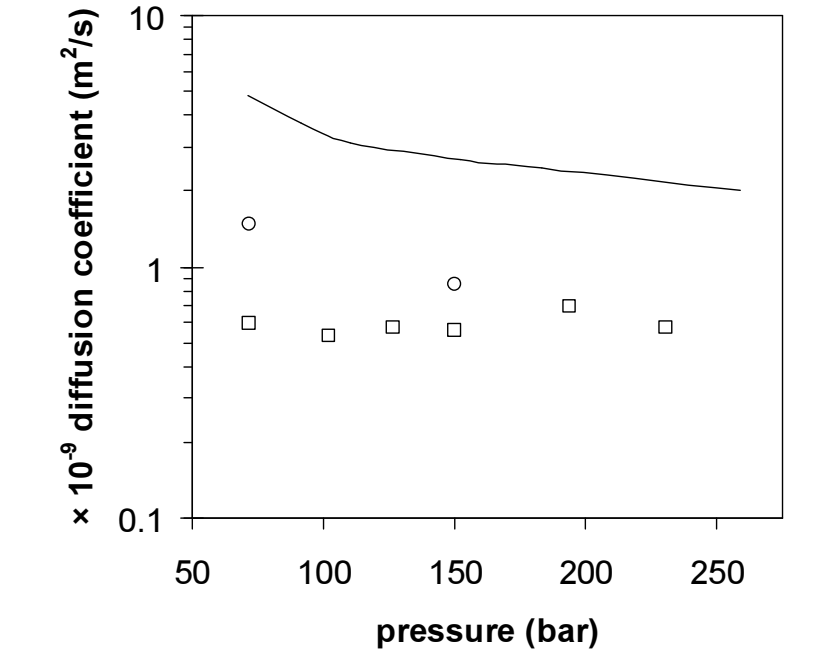

B

Figure 3.3 A) Normalized sorption and swelling kinetics of carbon dioxide in EVA-40 at 323 K and 150 bar; o *swelling;* □ *sorption;* — *Fickian plane sheet diffusion B) Fickian diffusion coefficients of carbon dioxide in EVA-40 at 323 K as a function of sorption pressure;* o *swelling;* □ *sorption; Mackie-Meares model*[25] *(—).*

and appear to conform to the values obtained from sorption curves at higher pressures. Possibly, this is caused by relaxation effects of the volume changes due to the initial compression, in addition to the sorption induced volume change.

Diffusion coefficients of penetrants in polymers can be predicted by the simple macroscopic model of Mackie and Meares[25]

$$D = D_0\left(\frac{\phi_V}{2-\phi_V}\right) \tag{3.7}$$

where ϕ_V is the volume fraction of CO_2 (i.e. the swelling), D the diffusion coefficient of CO_2 in the polymer and D_0 the self-diffusion coefficient of pure carbon dioxide. The model considers the polymer as an impermeable barrier with diffusion taking place through the carbon dioxide phase, resulting in higher diffusion coefficients with increasing swelling of the polymer. However, the pressure dependence of the diffusion coefficient is more complex. With increasing pressure, and thus swelling (see Fig. 3.2b), the diffusion coefficient increases towards the self-diffusion coefficient D_0 of carbon dioxide. This self-diffusion coefficient shows a strong decline with pressure, due to the increased density and viscosity, as estimated using the relation developed by Fuller and coworkers[26]. The resulting diffusion coefficient of CO_2 in EVA, shown in Fig. 3.3b, is weakly dependent on the pressure. Over the entire pressure range, the predicted values are higher than the values obtained from the sorption and swelling experiments. The model, however, does not take into account intrinsic material properties or specific interactions of the penetrant with the polymer.

The diffusion front of carbon dioxide in the rubbery polymer can visually be observed as a moving opaque boundary in the swelling polymer. Figure 3.4 shows a swelling experiment at 323 K and 250 bar at various stages early in the sorption process. The diffusion front is clearly visible as a smooth broadening boundary near the meniscus at 2 and 7 minutes. This is consistent with similar observations of diffusion boundaries in PBMA-carbon dioxide systems[24]. At 26 minutes the swelling starts to become visible, marked by the raised meniscus.

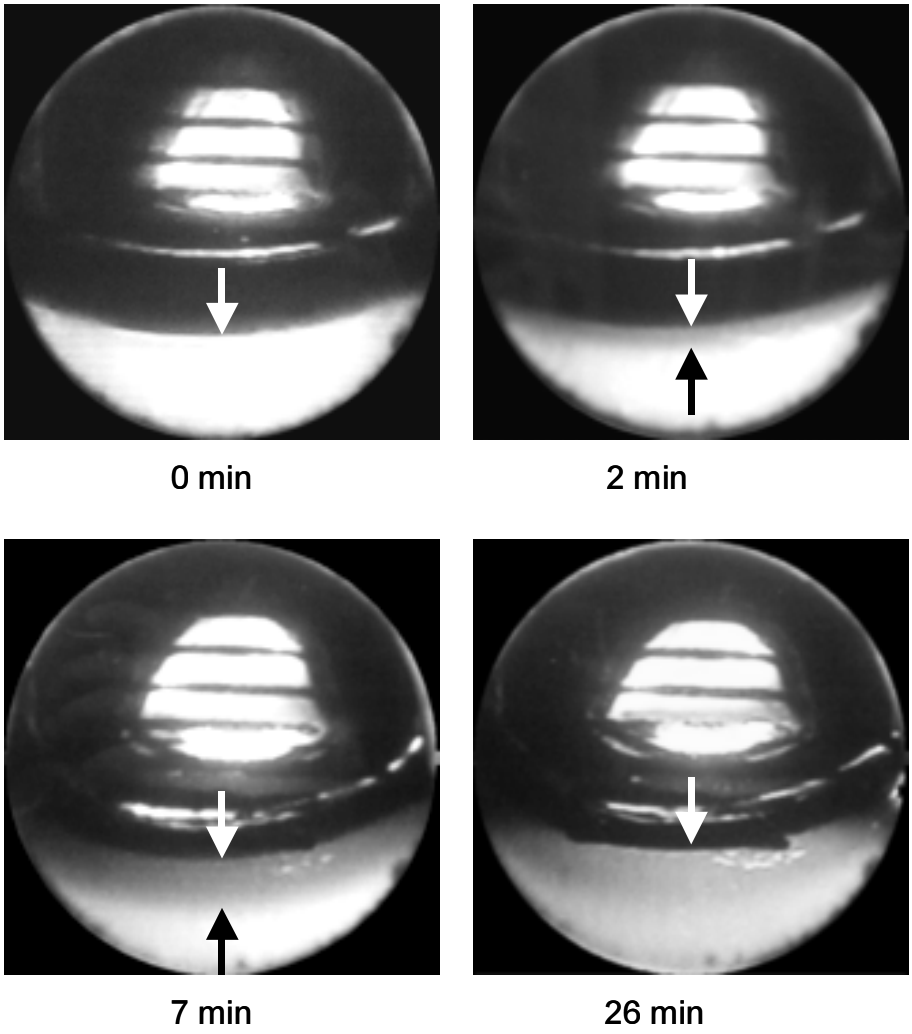

Figure 3.4 Swelling experiment of EVA-40 in carbon dioxide at 323 K and 250 bar. The swelling results in a rising of the meniscus (white marker). Initial diffusion front is visible as a smooth downward moving boundary in the photographs at 2 and 7 minutes (black marker). Horizontal lines are level marks on the glass sample holder.

3.3.3 Foam morphology

The foaming of carbon dioxide swollen polymer occurs after destabilizing the thermodynamic equilibrium. In this study, the polymer is foamed by a pressure quench. During the pressure quench, the polymer mixture becomes highly supersaturated, causing l nucleation and cell growth. Depending on the melting temperature or glass transition temperature, the polymer can vitrify, thereby stopping cell growth. In the case of EVA-40, the melting temperature is of most interest, as the glass transition temperature is generally far below the processing temperature.

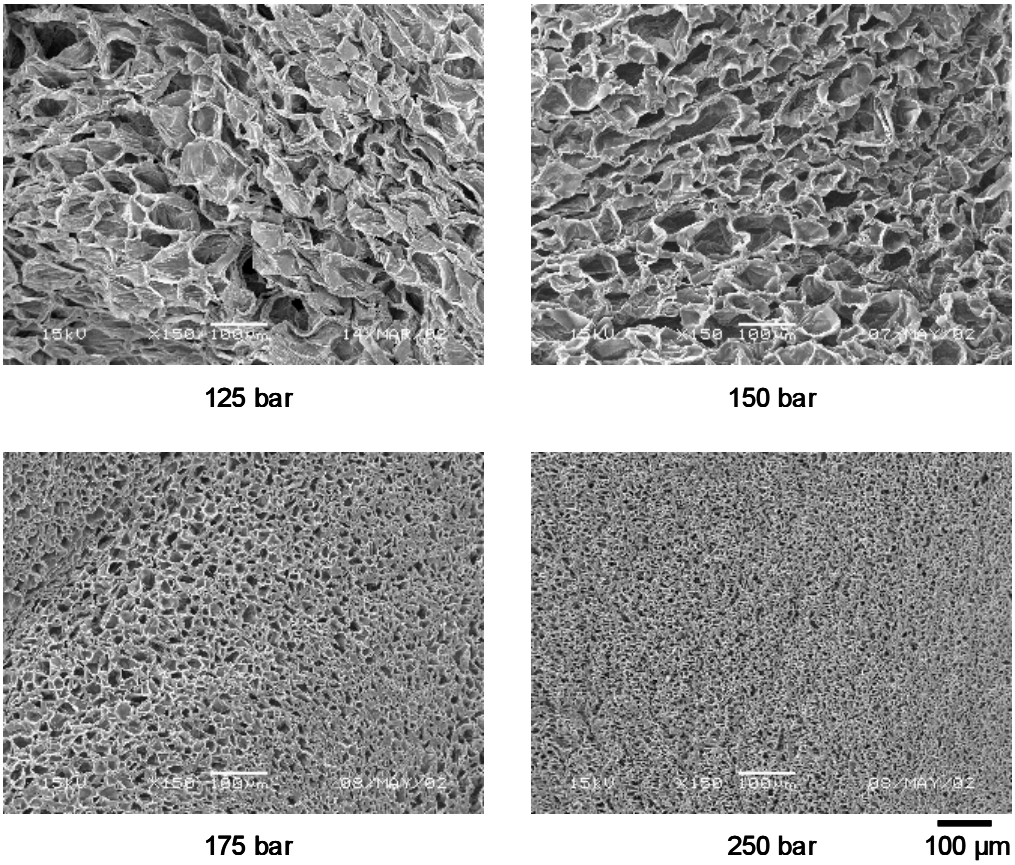

Figure 3.5 SEM micrographs (×150) of EVA-40 expanded with CO_2 at various pressures. Polymer saturated at 323 K and rapidly expanded (< 2 s).

The most accessible control parameters for the polymer foaming process using carbon dioxide are sorption pressure, sorption temperature and decompression rate. The influence of the sorption pressure on the foam morphology has been studied for rapid decompression (in less than two seconds) at a constant sorption temperature of 323 K. In all foaming experiments, sorption times have been chosen such that the polymer was at equilibrium before expansion. The obtained morphologies are shown in Figure 3.5. A decrease in pore size with increasing pressure is observed, with a large reduction in the average pore size between 150 and 175 bar. Higher magnification reveals a non-spherical, mostly open and interconnected structure with voids decreasing from approximately 50 µm at 125 bar to 10 µm at 250 bar. It should be noted, however, that the size of the pores shown in the SEM micrographs differ somewhat from the actual pore size. After gold coating in preparation for SEM, some thermal deformation / relaxation was observed, mostly affecting the samples with a large pore size, where the structure seems to be partly collapsed.

With increasing pressures, and thus higher sorption levels, an increase in supersaturation occurs during expansion. Additionally, according to homogeneous nucleation theory[2], the energy barrier to nucleation decreases with increasing pressure drop, leading to a higher nucleation density. This would result in smaller pore sizes, which is indeed observed in Figure 3.5.

The results from mercury intrusion porosimetry confirm the observations from the SEM micrographs. Figure 3.6a shows the mean and median pore diameters by volume as a function of sorption pressure. Similar to the SEM micrographs, a decrease in pore diameters is observed for increasing sorption pressures. The mean diameters obtained from the intrusion experiments confirm the visually observed diameters with values ranging from 7 μm to 62 μm. The median diameters are substantially lower at low pressures, indicating an broad size distribution at low pressures. The skeletal densities of the polymer foam, as obtained from the intrusion experiments, confirm the open structure of the foam. For the experiments at pressures below 250 bar, the skeletal density is only slighty lower than the density of the unfoamed polymer, indicating a skeletal porosity of approximately 10% due to closed cells. For the experiments at 250 bar no significant skeletal porosity is observed.

The bulk densities increase with pressure, thus lowering the porosity or expansion ratio, as shown in Figure 3.6b. Literature data on the foaming of amorphous polymers[5-7,27,28] mostly concerns polymers processed above the depressed glass transition temperature. At a certain stage in the decompression, the polymer vitrifies, thus ending the cell growth. The result then is a closed-cell microporous structure. In all cases with a sufficiently high temperature, a decrease in pore size diameters with higher sorption pressures is observed, similar to the results shown in Figure 3.6a. The foam densities or expansion ratios as a function of sorption pressure may vary for different polymers. Generally, the bulk density decreases with increasing sorption pressure, as both the carbon dioxide solubility and the nucleation rate increase. The increased sorption results in a longer period of growth, before vitrification occurs. In the case of EVA-40, an increase in bulk density is observed with increasing sorption pressure, as shown in Figure 3.6b. EVA-40 expands to an open porous structure, which is in contrast to the closed cell foams as discussed in literature[5-7,27,28]. Apparently, the gas is hindered in escaping from the polymer matrix, causing the bulk density to decrease and the foam to expand.

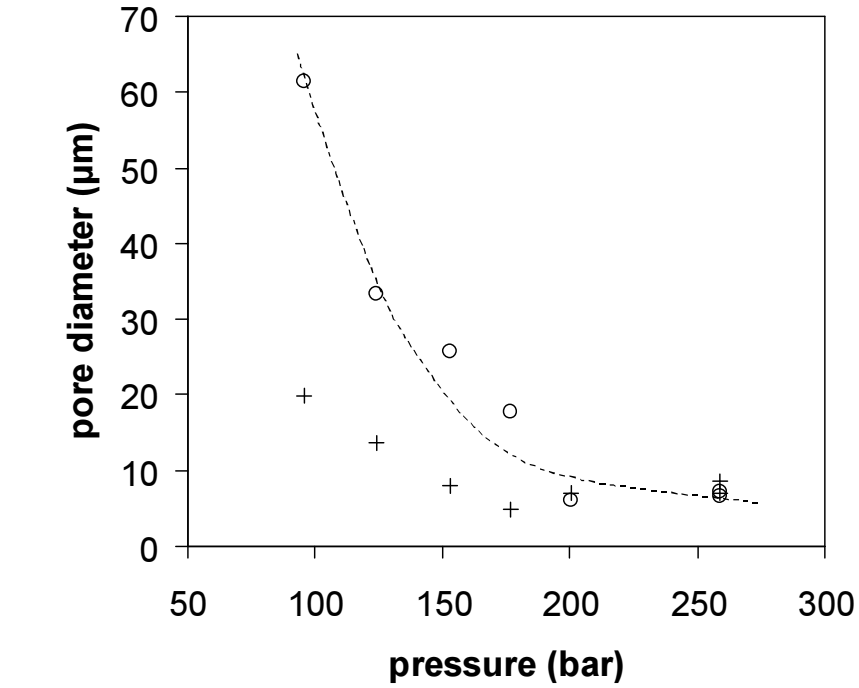

A

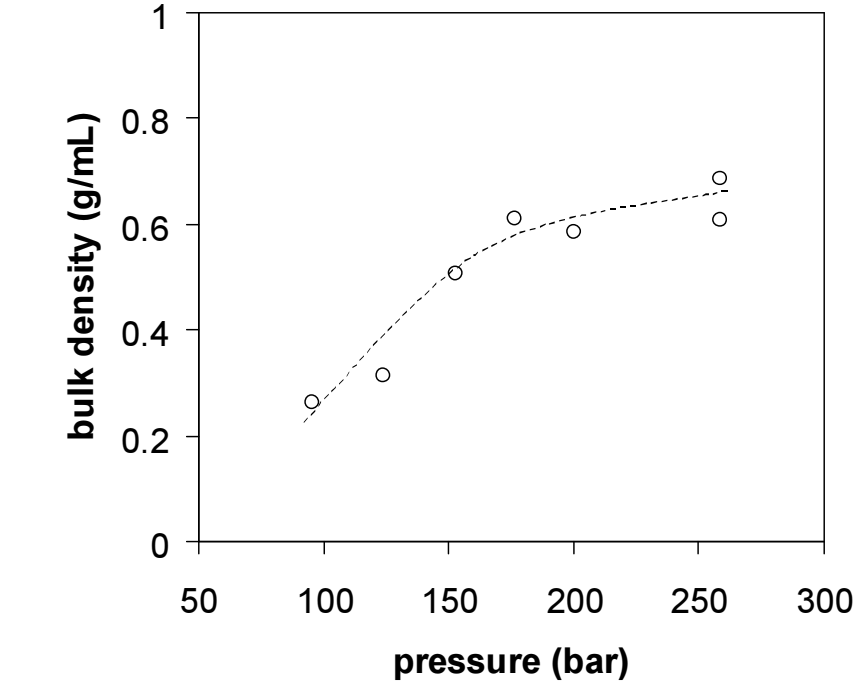

B

Figure 3.6 Mercury intrusion porosimetry characterization of CO_2 foamed EVA-40. Polymer saturated at 323 K and foamed by rapid expansion (< 2 s). A) mean (o) and median (+) pore sizes by volume as a function of sorption pressure; B) bulk densities of CO_2 foamed EVA-40 as a function of sorption pressure. (Lines show trends.)

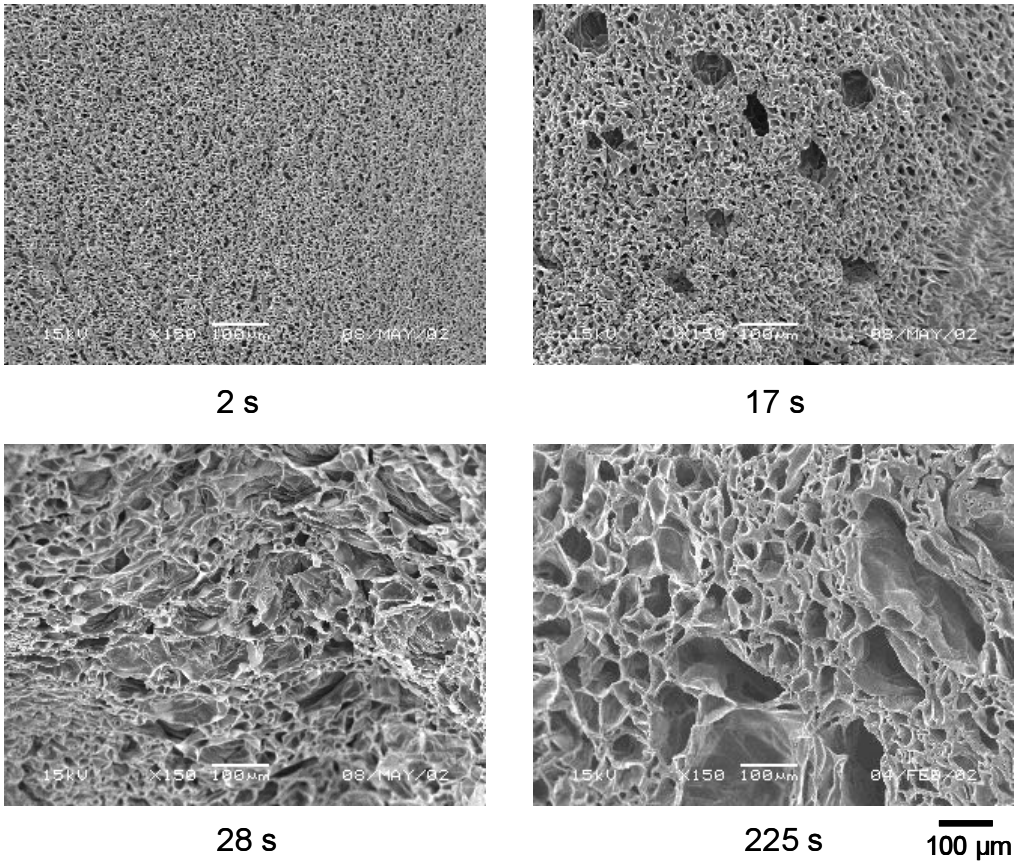

Figure 3.7 SEM micrographs (×150) of EVA-40 expanded with CO_2 at various expansion rates. Polymer saturated at 323 K and 250 bar.

The second adjustable parameter influencing the foam morphology is the decompression rate. The influence of the decompression rate on the foam morphology was studied for polymers equilibrated at a constant pressure and temperature of 250 bar and 323 K, respectively. Figure 3.7 shows the obtained morphologies, which reveal an increase in pore size with increasing decompression time. As previously mentioned, longer decompression times, and thus lower decompression rates, increase the energy barrier for nucleation. As a result, a reduced number of cells is formed. The formed cells follow a longer period of growth, resulting in a larger pore size, which is indeed observed in Figure 3.7. A large reduction in pore size is visible between the decompression times of 17 to 28 seconds. A similar increase in pore size has been obtained for the expansion of polystyrene with carbon dioxide by Arora et al.[6], although the experiments were performed on a decompression time scale of minutes rather than seconds. Higher magnifications of the polymer foams reveal pore morphologies very similar to the ones formed by rapid decompression and varying sorption levels.

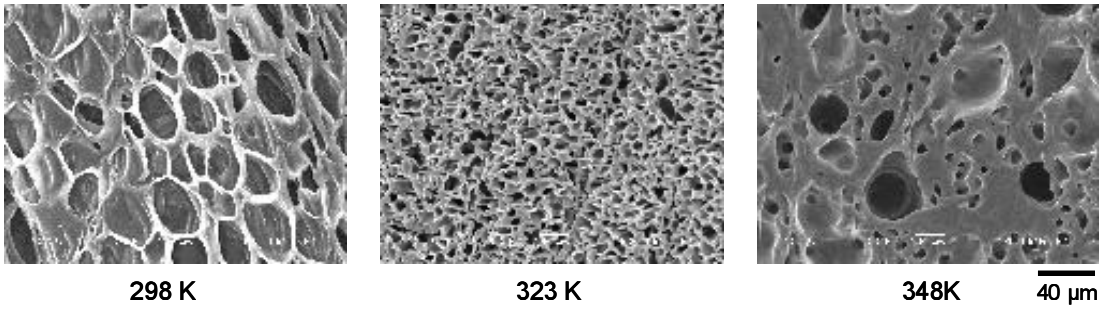

Figure 3.8 SEM micrographs (×550) of EVA-40 expanded with CO_2 at various temperatures. Polymer saturated at 250 bar. Foams formed by rapidly expansion (< 2 s).

The third parameter influencing the foam morphology is the sorption temperature. To study the influence of temperature on the foam morphology, experiments were carried out with polymer samples rapidly expanded from a constant sorption pressure of 250 bar. SEM micrographs of the obtained foams are shown in Figure 3.8. The influence of temperature on the morphology is rather complex, as it influences the sorption level, the nucleation rate as well as the viscosity. From Figure 3.8, a drastic change in morphology is observed with increasing temperature. At 323 K the same open microporous structure is obtained as discussed above. At this temperature, EVA-40 is just below its melting

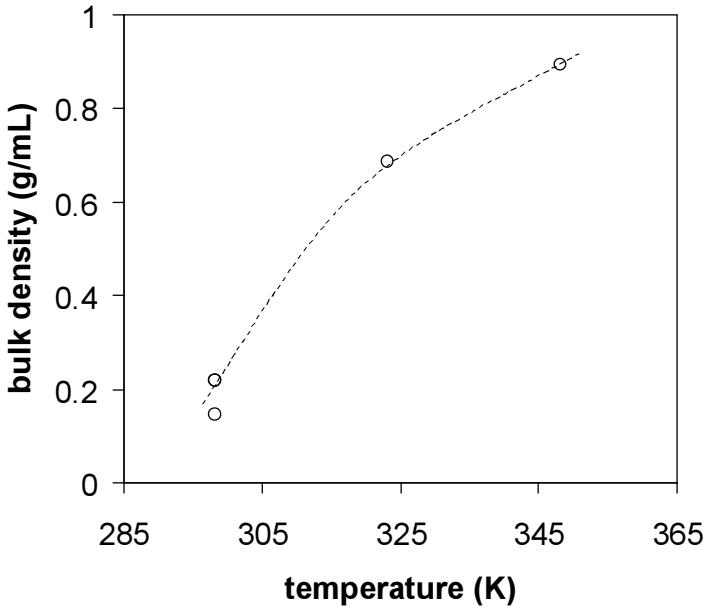

Figure 3.9 Influence of sorption temperature on the bulk density of CO_2 foamed EVA-40. Polymer saturated at 250 bar and foamed by rapid expansion. (Line shows trend).

temperature, which is possibly slightly depressed by carbon dioxide sorption. Expanding EVA-40 sorped at 298 K, results in an open porous morphology with an increased pore size of approximately 25 μm. At this sorption temperature, the expansion occurs in a swollen rubber with a concentration of CO_2 of approximately 55 wt% (SL eos estimation). Homogeneous nucleation theory[2] predicts a decrease in nucleation rate at lower temperatures, while previous sorption experiments have shown a higher sorption level at lower temperatures. For the sample at 298 K, this would result in a lower number of cells with an increased cell size compared to the foams formed at 323 K, which is indeed observed. Rapid expansion of the polymer equilibrated at 348 K, leads to a collapsed closed cell foam after decompression, which is expected considering the melting point of EVA-40. Mercury intrusion porosimetry confirms the SEM micrographs. For the samples expanded at 298 K, porosimetry indicates pore sizes of approximately 17 μm, where pore sizes of approximately 7 μm are obtained at 323 K. The foam bulk densities are shown in Figure 3.9. An increase in bulk densities is observed with increasing temperature, similar to Figure 3.6b. For the expansion at 298 K, the formation of a dense skin at the surface is observed. Figure 3.10, shows the dense skin of the polymer expanded at 298 K, whereas such a skin is not observed for the polymer expanded at 323 K, indicating a cooling of the surface of the polymer below the glass transition during the expansion. Calculation of gas temperatures obtained in irreversible adiabatic expansion reveal that this is indeed the case. Expansion of carbon dioxide at 298 K and 250 bar to atmospheric pressure results in a gas temperature of 218 K, which is below

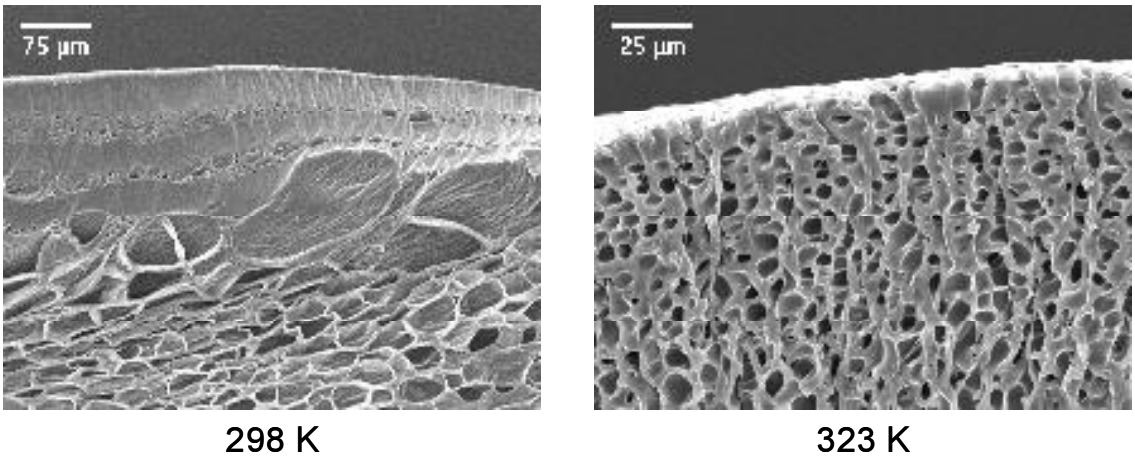

Figure 3.10 Skin formation after rapid expansion of EVA-40 sorped with CO_2 at 250 bar and temperatures 298 K and 323 K.

the T_g of EVA-40 (235 K). For CO_2 at 323 K, the final temperature after expansion is 243 K, which is above the glass transition temperature, hence no skin is formed.

3.4 Conclusions

The foaming of poly(ethylene-*co*-vinyl acetate) in supercritical carbon dioxide has been studied as a function of sorption pressure and temperature as well as decompression rate. The sorption and swelling isotherms have been measured and an increase in sorption and swelling levels at lower temperatures is observed. The sorption kinetics reveal a pressure independent diffusion coefficient for CO_2 in EVA-40. The foam morphology obtained after expansion can be controlled by the process conditions. All expansion conditions below the melting point of EVA result in mostly open microporous foam morphologies. Increasing the sorption pressure produces denser foams with smaller pore sizes after rapid expansion. Varying the expansion rates has a similar effect, resulting in foams with lower densities and smaller pore sizes at higher expansion rates. The sorption temperature has a substantial influence on the morphology of the foam. With increasing temperature, denser foams with smaller pores are formed. Above the melting point, the foam becomes unstable and partially collapses after expansion. To summarize, foaming of EVA rubbers using supercritical carbon dioxide allows for significant control of the foam structure, enabling a wide range of specialty applications, such as biomedical materials.

3.5 References

1. J.E. Martini-Vvedensky, N.P. Suh and F.A. Waldman, US patent 4473665, 1984.
2. S.K. Goel and E.J. Beckman, *Polym. Eng. Sci.* **34** (1994) 1137.
3. R.A. Reed, *Brit. Plast.* **33** (1960) 468.
4. S.G. Kazarian, *Polym. Sci.* **42** (2000) 78.
5. S.K. Goel and E.J. Beckman, *Polym. Eng. Sci.* **34** (1994) 1148.
6. K.A. Arora, A.J. Lesser and T.J. McCarthy, *Macromolecules* **31** (1998) 4614.
7. M.T. Liang and C.M. Wang, *Ind. Eng. Chem. Res.* **39** (2000) 4622.
8. J.A.H. Laarhoven, M.A.B. Kruft and H. Vromans, *Int. J. Pharm.* **232** (2002) 163.
9. H. Bruinewoud, M.F. Kemmere and J.T.F. Keurentjes, submitted for publication.
10. L.A. Kleintjens and R.J. Koningsveld, *Electrochem. Soc.* **127** (1980) 2352.
11. R.H. Lacombe and I.C. Sanchez, *J. Phys. Chem.* **80** (1976) 2568.
12. I.C. Sanchez and R.H. Lacombe, *Macromolecules* **11** (1978) 1145.
13. J. Crank, *The Mathematics of Diffusion*, 2nd ed., Clarendon Press, Oxford, 1975.

14. P. Zoller and D.J. Walsh, *Standard Pressure-Volume-Temperature Data for Polymers*, Technomic Publishing, Lancaster, 1995.
15. C.A. Mertdogan, T.P. DiNoia and M.A. McHugh, *Macromolecules* **30** (1997) 7511.
16. J.R. Royer, J.M DeSimone and S.A. Khan, *Macromolecules* **32** (1999) 8965.
17. S.G. Kazarian, M.F. Vincent, F.V. Bright, C.L. Liotta and C.A. Eckert, *J. Am. Chem. Soc.* **118** (1996) 1729.
18. Y.T. Shieh and Y.G Lin, *Polymer* **43** (2002) 1849.
19. Y. Zhang, K.K. Gangwani and R.M. Lemert, *J. Supercrit. Fluids* **11** (1997) 115.
20. G.J. Fleming and W.J. Koros, *Macromolecules* **19** (1986) 2285.
21. R.G. Wissinger and M.E. Paulaitis, *J. Polym. Sci. B* **25** (1987) 2497.
22. Y. Kamiya, K. Mizoguchi, K. Terada, Y. Fujiwara and J.S. Wang, *Macromolecules* **31** (1998) 472.
23. I.S. Liau and M.A. McHugh, In *Supercritical Fluid Technology*, Elsevier Science Publishers, Amsterdam, 1985, p. 415-434.
24. L.N. Nikitin, E.E. Said-Galiyev, R.A. Vinokur, A.R. Khokhlov, M.O. Gallyamov and K. Schaumburg, *Macromolecules* **35** (2002) 934.
25. J.S. Mackie and P. Meares, *Proc. R. Soc. London* **A232** (1955) 498.
26. R.C. Reid, J.M. Prausnitz and B.E. Poling, *The Properties of Gases and Liquids*, 4th ed., McGraw-Hill, New York, 1987.
27. C.M. Stafford, T.P. Rusell and T.J. McCarthy, *Macromolecules* **32** (1999) 7610.
28. K.N. Lee, H.J. Lee and J.H. Kim, *Polym. Int.* **49** (2000) 712.
29. M.B. Kiszka, M.A. Meilchen and M.A. McHugh, *J. Appl. Poly. Sci.* **36** (1988) 583.

CHAPTER 4

CONTACTLESS LIQUID DETECTION IN A PARTLY FILLED TUBE

Abstract

Contactless fluid level detection in process equipment is an important challenge for the process automation industry, especially under high-pressure conditions. In this study, a method is presented which enables the contactless measurement of liquid levels in thin opaque capillaries at high pressures. The method is based on the mass dependence of the resonance frequencies of a finite section of a tube. These resonance frequencies are determined from the complex electrical impedance of a slitted toroid coil exciting a magnet attached to the tube. The system has been theoretically described using a set of two Bernoulli-Euler beams, resulting in an analytical solution for the equation of motion. To validate the model, experiments have been performed on a thick-walled stainless steel capillary partly filled with mercury. The model is in good agreement with the experimental data. Moreover, the sensitivity of the method appears to be adequate as a fluid level indicator for control purposes in industrial applications.

This chapter has been submitted as: M.A. Jacobs, R. Breeuwer, M.F. Kemmere and J.T.F. Keurentjes, Contactless liquid detection in a partly filled tube by resonance.

4.1 Introduction

In a growing number of chemical and pharmaceutical processes, near critical and supercritical fluids are replacing traditional organic solvents. In particular, high-density carbon dioxide is increasingly used in applications such as extractions[1], polymer synthesis and processing[2] as well as pharmaceutical processing[3, 4]. Depending on the fluid used, these processes are operated at much higher pressures than conventional processes, typically above 50 bar. Additionally, in pharmaceutical and food processes, contactless setups are preferred, to reduce the risk of contamination. Consequently, constraints are imposed on the process equipment, including the methods for liquid level detection.

For the detection of liquids in opaque tubes at fixed positions, a technique based on the intensity of a focused ultrasonic sound beam transmitted through the tube can be used[5]. However, the resolution of the signal sharply decreases with increasing wall thickness of the tubing, rendering the technique unsuitable for high-pressure systems. In this chapter, a technique is presented for the detection of variable liquid levels under high pressures. The method is based on new implementation of the well-known effect of lowering the resonance frequency of an elastic body by mass loading. For this purpose, a section of the tube is clamped at two points and a tiny magnet is attached to the center. A slitted toroid coil excites the section of the tube in transversal resonance. The complex electrical impedance of this same coil is used to determine the resonance frequency. This enables a constructionally simple and contactless setup. Moreover, the method allows for measurements in thin, opaque capillaries, at high pressures and increased temperatures.

To determine the sensitivity of the system, it has been described as a set of two Bernoulli-Euler beams, under the assumption of free vibration. An analytical solution for the equation of motion has been derived. To validate the model, experiments with a realistic stainless steel capillary partly filled with mercury are presented.

4.2 Bernoulli-Euler beam model

In Figure 4.1 a clamped tube partly filled with liquid is shown, which is considered to be in free vibration. The length between the clamps is defined L. The

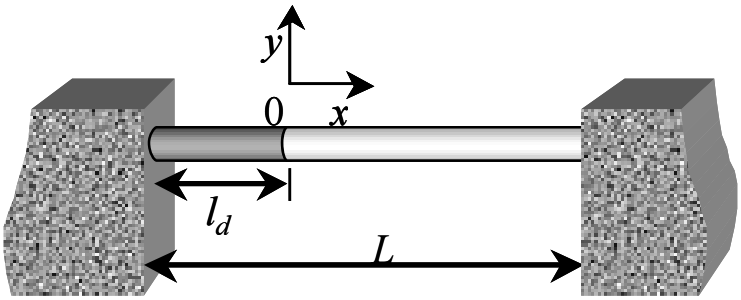

Figure 4.1 Schematic representation of a clamped tube partly filled with liquid.

liquid-gas interface in the tube is marked by an abrupt change in mass density from m_1 to m_2 and is positioned at the origin. The distance between the origin and the left-hand clamp is defined l_d. The system can be regarded as a set of two Bernoulli-Euler beams, each with a uniform bending stiffness *EI* and a constant mass density m_i [6,7]. The equation of motion is given by

$$EI\frac{\partial^4 y_i}{\partial x^4} + m_i \frac{\partial^2 y_i}{\partial x^2} = 0 \tag{4.1}$$

with m_i

$$m_i = \begin{cases} m_1 & -l_d < x < 0 \\ m_2 & 0 < x < L - l_d \end{cases} \tag{4.2}$$

The solutions of Equation (4.1) are $y_1(x,t)$ in the range $-l_d < x < 0$ and $y_2(x,t)$ in the range $0 < x < L - l_d$. The boundary conditions at $x = -l_d$ and $x = L - l_d$ are given by

$$y_1(-l_d,t) = y_1'(-l_d,t) = y_2(L-l_d,t) = y_2'(L-l_d,t) = 0 \tag{4.3}$$

The continuity and equilibrium conditions at the origin are

$$\begin{aligned} y_1(0,t) &= y_2(0,t) & y_1'(0,t) &= y_2'(0,t) \\ y_1''(0,t) &= y_2''(0,t) & y_1'''(0,t) &= y_2'''(0,t) \end{aligned} \tag{4.4}$$

The general solutions of the equation of motion for a uniform beam[8] are

$$y_j(x,t) = \mathbf{C}_j^T \mathbf{G}_j(x) e^{i\omega t} \tag{4.5}$$

with the displacement function and constants given by

$$\begin{aligned}\mathbf{C}_j^T &= \begin{pmatrix} C_{j1} & C_{j2} & C_{j3} & C_{j4} \end{pmatrix} \\ \mathbf{G}_j^T(x) &= \begin{pmatrix} \sin k_j x & \cos k_j x & \sinh k_j x & \cosh k_j x \end{pmatrix}\end{aligned} \tag{4.6}$$

where $k_j^4 = m_j \omega^2 / EI$.

Applying the continuity and equilibrium conditions to the general solution, the following relation is obtained

$$\mathbf{C}_1 = \mathbf{F}\mathbf{C}_2 \tag{4.7}$$

with **F** given by

$$\mathbf{F} = \begin{pmatrix} \gamma\gamma_1 & 0 & \gamma\gamma_2 & 0 \\ 0 & \gamma_1 & 0 & \gamma_2 \\ \gamma\gamma_2 & 0 & \gamma\gamma_1 & 0 \\ 0 & \gamma_2 & 0 & \gamma_1 \end{pmatrix} \tag{4.8}$$

where $\gamma = (m_2 / m_1)^{1/4}$, $\gamma_1 = (1+\gamma^2)/2$ and $\gamma_2 = (1-\gamma^2)/2$. Substitution of Equations (4.5) and (4.7) into the boundary conditions Equation (4.3) results in

$$\mathbf{S}\mathbf{C}_1 = 0 \tag{4.9}$$

with

$$\mathbf{S} = \begin{pmatrix} -\gamma\gamma_1 \sin u_1 - \gamma\gamma_2 \sinh u_1 & \gamma_1 \cos u_1 + \gamma_2 \cosh u_1 & & \\ \gamma\gamma_1 \cos u_1 + \gamma\gamma_2 \cosh u_1 & \gamma_1 \sin u_1 - \gamma_2 \sinh u_1 & & \\ \sin u_2 & \cos u_2 & & \\ \cos u_2 & -\sin u_2 & & \\ & & -\gamma\gamma_2 \sin u_1 - \gamma\gamma_1 \sinh u_1 & \gamma_2 \cos u_1 + \gamma_1 \cosh u_1 \\ & & \gamma\gamma_2 \cos u_1 + \gamma\gamma_1 \cosh u_1 & \gamma_2 \sin u_1 - \gamma_1 \sinh u_1 \\ & & \sinh u_2 & \cosh u_2 \\ & & \cosh u_2 & \sinh u_2 \end{pmatrix} \tag{4.10}$$

where $u_1 = k_1 l_d$ and $u_2 = k_2 (L - l_d)$. A non-trivial solution is obtained when

$$\det \mathbf{S} = 0 \tag{4.11}$$

After some rearrangement and simplification, the analytical solution of Equation (4.11) is given by

$$\begin{aligned}&\left(\gamma_1^2+\gamma_2^2\right)\left[1-\cos u_1\cos u_2\cosh u_1\cosh u_2\right]+2\gamma_1\gamma_2\left[\cos u_1\cosh u_1-\cos u_2\cosh u_2\right]+\\&\gamma\gamma_1\left[\sin u_1\sin u_2\cosh u_1\cosh u_2-\sinh u_1\sinh u_2\cos u_1\cos u_2\right]+\\&\gamma\gamma_2\cos u_2\left[\sin u_2\sinh u_1\cosh u_2-\sin u_1\sinh u_2\right]+\gamma^2\sin u_1\sin u_2\sinh u_1\sinh u_2=0\end{aligned} \tag{4.12}$$

In the special case of a uniform tube ($l_d = 0$ or $l_d = L$), Equation (4.12) reduces to

$$\cos u \cosh u = 1 \tag{4.13}$$

for $\gamma \neq 0$, with $u = \left(m_j / EI\right)^{1/4} \sqrt{\omega_i} L$. Numerically approximated, the solutions of Equation (4.13) are $u \approx 0$, 1.5056π, 2.4998π and $u \approx (n + ½)\pi$ for n = 3, 4, 5… where n corresponds to the vibrational mode. The Bernoulli-Euler theory is only applicable to "long" beams. For beams with compact cross sections, the wavelength has to be larger than 5 times the height of the beam, whereas thin-walled sections require wavelengths of more than 10 times the height of the beam. For smaller wavelengths, the Euler-Bernoulli theory is extended to the Timoshenko beam theory[9].

4.3 Experimental setup and procedures

The experimental setup, shown in Figure 4.2, consists of a steel capillary (ρ = 7950 kg/m^3) clamped by two 20 mm clamps. The distance between the clamps is 160 mm. The capillary has inner and outer diameters of 1.0 and 3.2 mm, respectively. At the bottom, the steel capillary is connected to a glass capillary by flexible tubing. The glass capillary has inner and outer diameters of 2.1 and 3.9 mm, respectively. The two connected tubes are partly filled with mercury

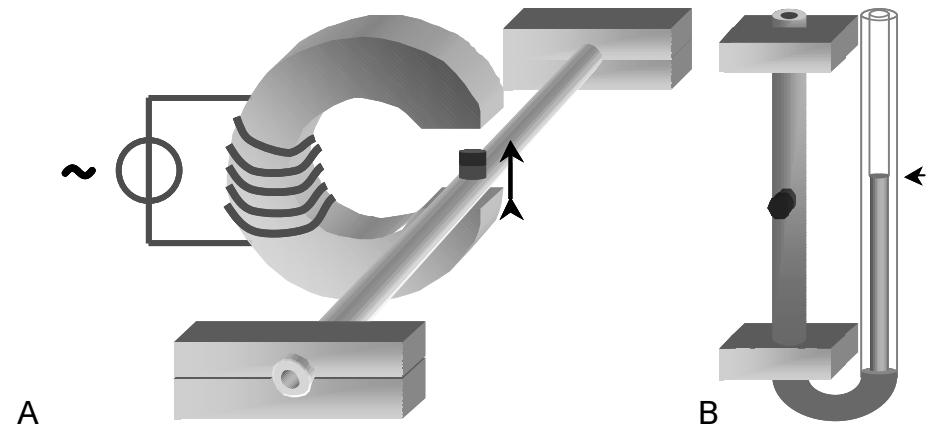

Figure 4.2 Schematic view of the experimental setup. A) Clamped tube configuration with attached magnet, coil and impedance meter. B) Test setup with clamped steel capillary at the left side and a glass capillary at the right side, connected by flexible tubing.

(ρ = 13,540 kg/m^3). To excite the steel tube, a small magnet (m = 0.15 g) is attached to the center. The magnetic field of the magnet is perpendicular to the axis of the tube and in line with the slit in the toroid coil, as shown in Figure 4.2a. The coil is connected to an impedance analyzer (Hioki 3532 LCR, ± 0.1 Hz), controlled by a computer. The resonance frequency of the tube is obtained from a maximum in the spectrum of the coil impedance modulus. This setup allows measurement of the odd modes of vibration, containing an antinode at half the tube length. The resolution of the frequency setting on the analyzer is 0.1 Hz in the low frequency range. In the high frequency range, the resolution is 1 Hz, which is too large to detect the higher modes of vibration. The mercury level in the glass tube is visually observed using a cathetometer (Bleeker, ± 0.1 mm).

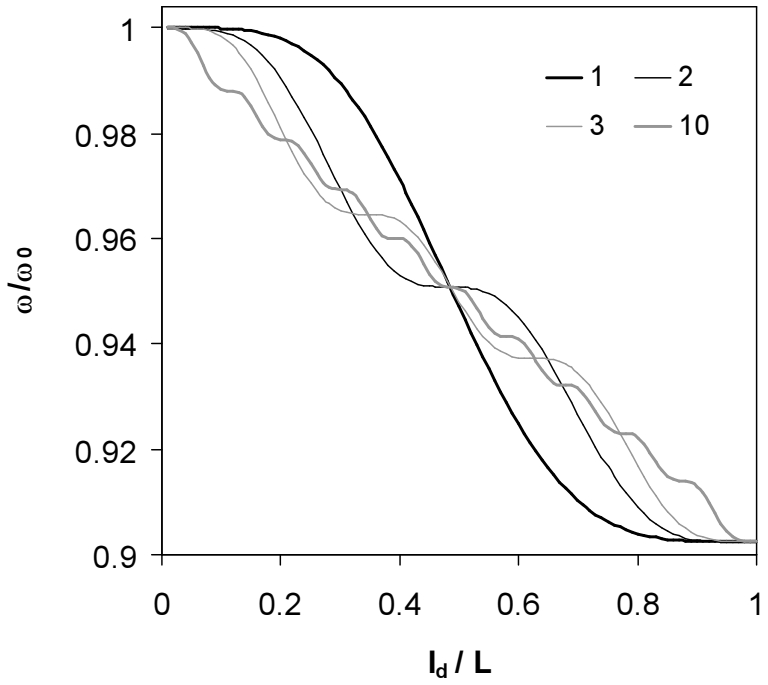

Figure 4.3 Bernoulli-Euler model calculations of the relative frequency change as a function of relative filling height of the tube, with $\gamma = 0.95$ ($m_1/m_2 \approx 1.228$). Vibrational modes 1, 2, 3 and 10 are shown.

4.4 Results and discussion

The relative frequency change as a function of filling height is calculated by Equation (4.11) or (4.12), respectively. In Figure 4.3 the frequency ratios as a

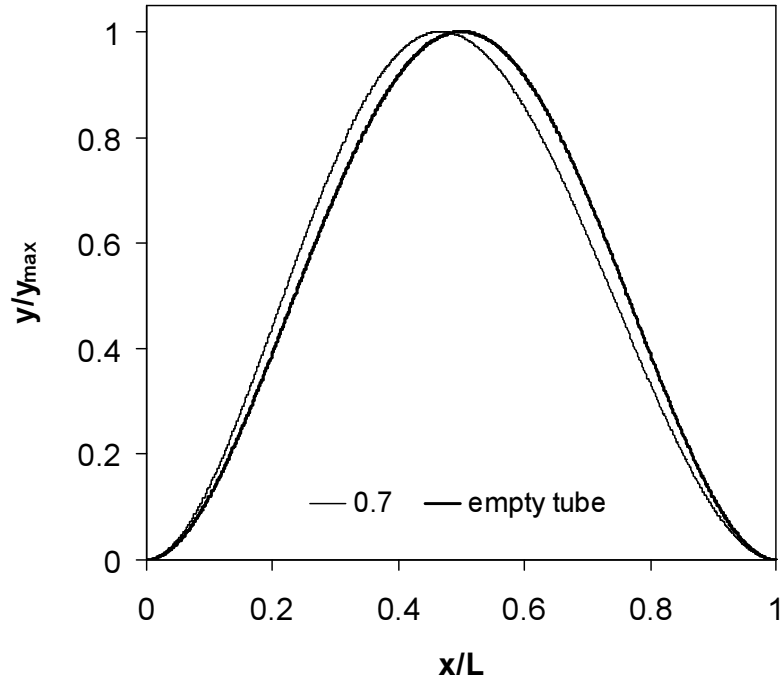

A

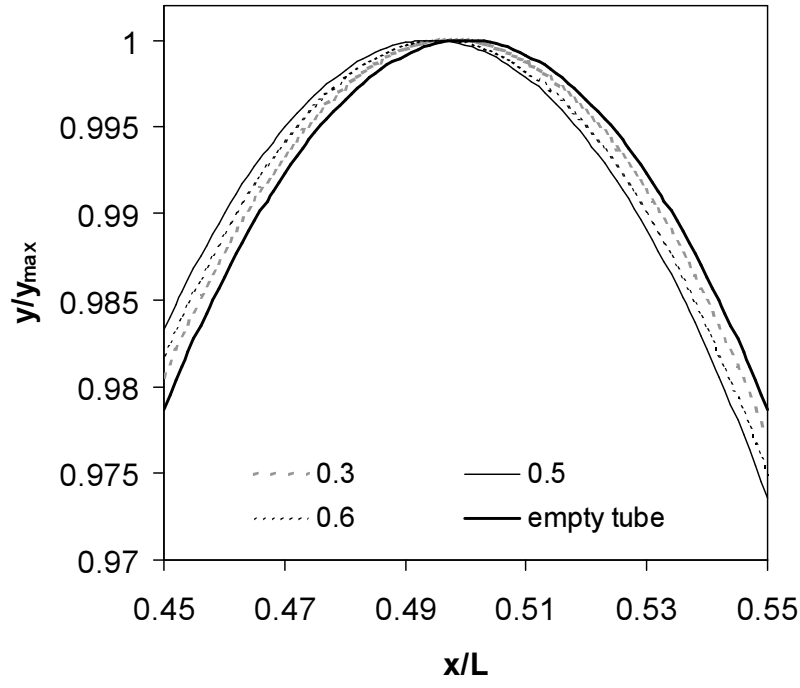

B

Figure 4.4 Shifts in the fundamental mode shape y(x). A) mode shape of a half filled tube with $\gamma = 0.7$ ($m_1 / m_2 = 4.165$) and an empty tube. B) mode shape as a function of filling height l_a with $\gamma = 0.95$ ($m_1 / m_2 = 1.228$).

function of the relative filling height are shown for vibrational modes 1, 2, 3 and 10. Mode 10 is the highest mode, which can be described with the Bernoulli-Euler theory. In the calculations $\gamma = 0.95$ is used, corresponding to a relative mass density increase of 22.8%. All modes show the same relative change in frequency for a fully filled tube. Similar behavior was observed for simply supported[6] and clamped-free[7] geometries.

For the fundamental mode, a continuous decrease of the frequency with increasing fluid levels is observed, with a steep gradient near a relative filling height of 0.5. At higher vibrational modes, regions of non-varying frequencies (plateaus) are observed. These plateaus can be attributed to the occurrence of vibrational nodes. The fundamental mode contains no nodes. For higher modes, each mode adds an additional node. Near a node, displacements and accelerations are small, resulting in less added mass effects. The reverse is true near antinodes, where accelerations are large and a significant shift in frequency with increasing fluid height is observed.

Though symmetric boundary conditions are applied, the curves for all modes are slightly asymmetric, due to the asymmetric mass distribution of the tube. For

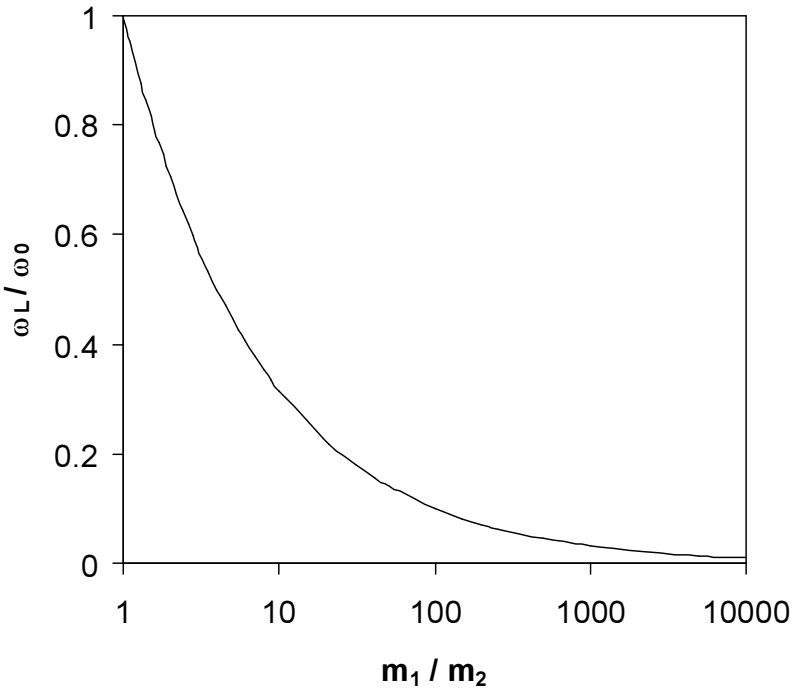

Figure 4.5 Relative frequency shift of a filled tube as a function of the relative mass density ratio

all modes, the central node or antinode is slightly shifted towards the fluid filled side. The actual shift in mode shape depends on the mass density ratio and the filling height. In Figure 4.4a, the fundamental mode shape is shown for a relative filling height of 0.5 and a γ of 0.7, which corresponds to an increase in mass density of 316.5%. Such a large difference in mass densities combined with the fluid level near the antinode, results in a large shift in the position of the antinode towards the filled side of the tube. In Figure 4.4b, the shift in mode shape is shown as a function of filling height of the tube. In these calculations, a more moderate mass density ratio of 1.228 (γ = 0.95) is applied, resulting in smaller changes in mode shape. The largest shifts of the antinode are observed for filling heights near the antinode $(l_d / L) \sim 0.5$, where displacements are large. The shift in frequency for a filled tube is a unique function of the mass density ratio of the two sides of the tube. The ratio is related to tube dimensions and material densities by

$$\frac{m_1}{m_2} = \frac{d_{out}^2 - \left(1 - \frac{\rho_{liquid}}{\rho_{tube}}\right) d_{in}^2}{d_{out}^2 - d_{in}^2} \tag{4.14}$$

In Figure 4.5 the frequency shift of a filled tube is shown as a function of the mass ratios. The frequency shows an asymptotic decline to zero. A reduction in frequency of 50 % is already reached for a mass ratio m_1 / m_2 of 4. These shifts in relative frequency are the same for all vibrational modes. However, for higher modes the natural frequency of the empty tube increases quadratically

$$\frac{\omega_n}{\omega_1} = \left(\frac{u_n}{u_1}\right)^2 \tag{4.15}$$

where n corresponds to the mode number and u_n is the n^{th} solution of Equation (4.13), excluding the trivial solution u = 0.

In Figure 4.6 the shift in frequency for the fundamental mode of a steel tube partly filled with mercury is shown. The experimental data are correlated with the Bernoulli-Euler model. In the specified setup, with $m_1 / m_2 \approx 1.184$ $(\gamma \approx 0.959)$, the frequency shifts from 509.9 Hz to 468.5 Hz. Calculating the bending stiffness *EI* of the tube from the frequency of the empty tube and applying the tube dimensions and material densities, a shift of the frequency to 468.54 Hz is predicted. As shown in Figure 4.6, the model excellently relates the filled tube frequency to the empty tube frequency. However, for partially filled tubes, the experimental data appear

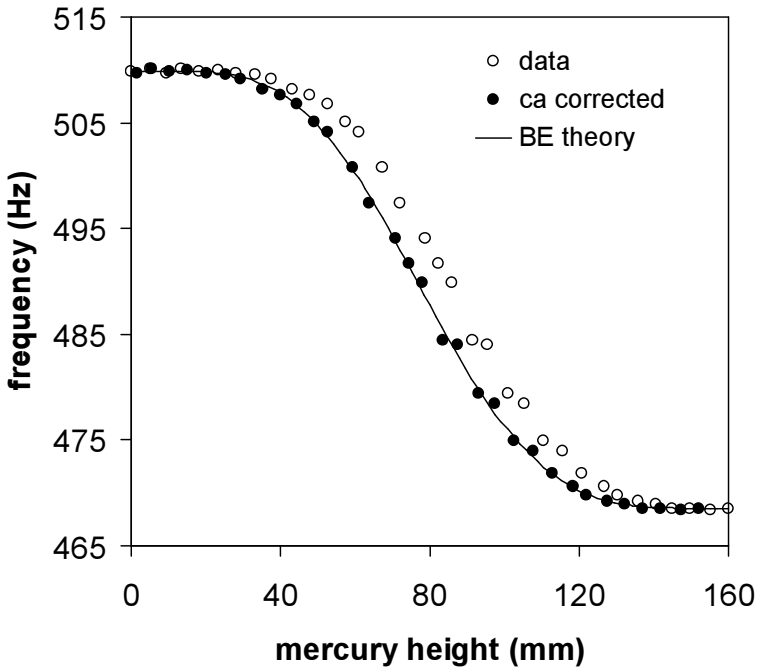

Figure 4.6 Resonance frequency as a function of filling height of a steel capillary partly filled with mercury. Data before and after correction for capillary action (ca), and the correlation with the Bernoulli-Euler model is shown.

to be shifted to lower filling heights. This is caused by the capillary action of mercury in these small tubes, since mercury exhibits a non-wetting behavior on both glass and steel surfaces, causing a negative capillary action. Equation (4.16) shows the difference in height between the steel and glass tubes, which is caused by capillary action.

$$dh = \frac{2\gamma}{\rho g} \frac{r_2 \cos\theta_{c,2} - r_1 \cos\theta_{c,1}}{r_1 r_2} \tag{4.16}$$

Here γ is the surface tension, θ is the contact angle and r are the tube radii. After correction of the experimental data for capillary action, excellent agreement between the model calculations and the data is observed. At least for the fundamental mode, these results justify the assumption that the measured resonance frequency can be described by the natural frequency of the tube. Furthermore, in the applied setup the mass of the magnet attached to the tube appears not to have a measurable influence on the characteristics of the response of the resonance frequency to changing fluid heights. For application of the technique as an indicator for liquid levels in a tube, only the fundamental mode is

applicable. The plateaus occurring at higher modes result in regions with a very small gradient in frequency. For the same reason, practical measurements of fluid levels are limited to the midsection of the tube, approximately $0.25 < l_d / L < 0.75$, thus limiting the effective measuring region of the tube to half the tube length.

To obtain insight in the accuracy of measurements with fluids less dense than mercury, the sensitivity of the filling height to a change in frequency has been determined for water in steel high-pressure tubes. For this purpose, the change of the liquid height Δl_d, corresponding to a change in frequency of 0.2 Hz at a filling of $L / l_d = 0.75$ is calculated for three commercially available Swagelock® high-pressure steel tubes with increasing diameters as a function of the clamped length of the tube. The tubes have outer diameters (OD) of 1/8, 1/4 and 1/2 inch and wall thicknesses of 0.028, 0.035 and 0.065 inch, respectively, which correspond to the minimal available thickness suitable for a working pressure of 300 bar at 475 K.

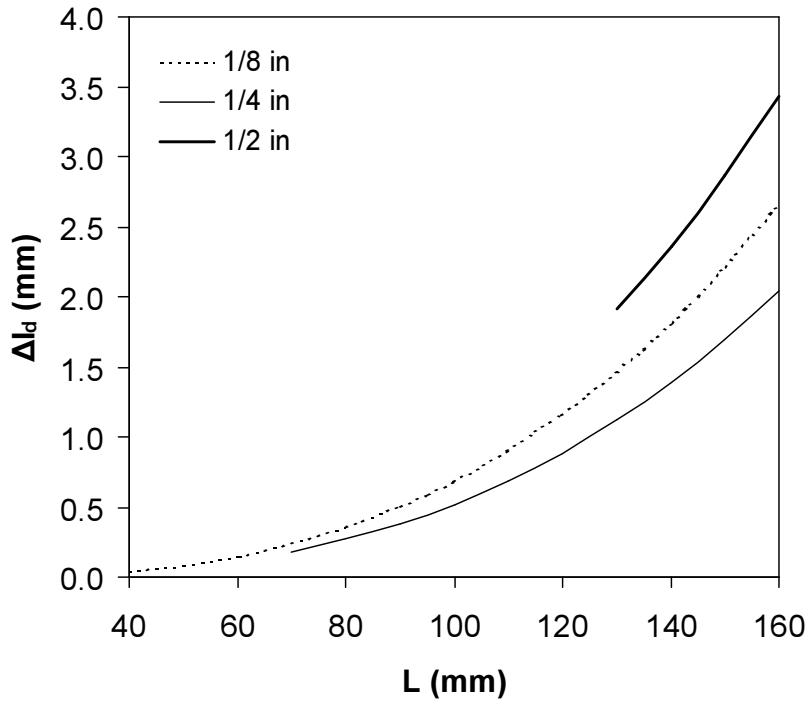

Figure 7. Sensitivity of the calculated filling height of water at $L / l_d = 0.75$ to a frequency change of 0.2 Hz as a function of tube length for three commercially available high-pressure steel tubes with dimensions: 1/8'' OD / 0.028'' wall; 1/4'' OD / 0.035'' wall and 1/2'' OD / 0.065'' wall.

In Figure 4.7, the results are shown for clamped tube lengths of 10×OD to 160 mm. All tubes show a progressively decreasing accuracy with increasing clamp length. If we accept a maximum Δl_d of 1 mm at an accuracy in the frequency of 0.2 Hz, the maximum clamp lengths are 114 mm for the 1/8 inch tube and 125 mm for the 1/4 inch tube. For the 1/2 tube, the maximal achievable accuracy is 1.9 mm at the minimal clamp length of 10×OD. As mentioned previously, the maximum measurement lengths of the tubes are half these clamp lengths. In general, the sensitivity study shows that the operating window of the contactless liquid detection method is sufficiently broad, for which the tube diameter required for the applied pressure forms a critical parameter.

4.5 Conclusions

In this work, the use of transversal resonance frequencies as a contactless indication method for the liquid height in a tube has been investigated. A Bernoulli-Euler vibrational analysis for a partly filled tube has been performed, resulting in an analytical solution of the equations of motion. The analysis shows plateau regions in the frequency shift for higher vibrational modes, thus limiting the technique to the fundamental mode. To verify the model calculations, experiments have been carried out on a realistic steel capillary filled with mercury. The model calculations are in good agreement with the data. In the experiments, the use of the complex electrical impedance of a toroid coil enclosing the tube with a magnet attached has proven to be a good indicator for the detection of the natural frequency of the tube. Using the fundamental mode, accurate measurements are limited to the midsection of the tube, where the largest frequency gradient occurs. For detection of mercury in tubes with inner diameters below 10 mm, the capillary action of the mercury has to be taken into account. The experiments indicate a fluid level detection sensitivity adequate for control purposes in industrial automation applications. The constructional simplicity of the method and its contactless setup as well as the ability to be used in high pressure systems, makes the technique a versatile tool for fluid level detection in a wide variety of industrial applications such as chemical, pharmaceutical and food processes.

4.6 References

1. M.A. McHugh and V.J. Krukonis, *Supercritical Fluid Extraction: Principles and Practice*, Butterworth Heinemann, Boston, 1993.
2. A.I. Cooper, *J. Mat. Chem.* **10** (2000) 207.
3. B. Subramaniam, R.A. Rajewski and K. Snavely, *J. Pharm. Sci.* **86** (1997) 885.
4. E. Reverchon, *J. Supercrit. Fluids* **15** (1999) 1.
5. M.A. Jacobs, M.F. Kemmere, Th.W. de Loos and J.T.F. Keurentjes, In *Proceedings of the 7th Meeting on Supercritical Fluids*, ISAFS, Antibes, 2000, 243.
6. K.T. Chan, T.P. Leung and W.O. Wong, *J. Sound Vibr.* **191** (1996) 590.
7. K.T. Chan and J.Z. Zhang, *J. Sound Vibr.* **182** (1995) 185.
8. R.E.D. Bishop and D.C. Johnson, *The Mechanics of Vibration*, Cambridge University Press, Cambridge, 1960.
9. K. Marguerre and K. Wölfel, *Mechanics of Vibration*, Sijthoff & Noordhoff, Alphen aan den Rijn, 1979.

CHAPTER 5

SIMULTANEOUS MEASUREMENT OF SORPTION AND SWELLING

Abstract

For the effective application of supercritical fluids in polymer processing, a thorough understanding of the phase behavior of polymers in high-density gases is required. In this study, an apparatus is developed to simultaneously measure sorption and swelling of a polymer sample in a high-pressure gas. The swelling of the polymer is determined from a direct volume measurement of the polymer sample by submersion in mercury. The sorption of the gas in the polymer is determined by measuring the pressure decay in a closed polymer-gas-mercury system. This procedure eliminates the need for corrections of buoyancy and anisotropic dilation, as required in some conventional sorption and swelling measurements.

5.1 Introduction

Recent advances in supercritical fluid technology have resulted in a variety of polymer processes using supercritical fluids[1]. Applications include e.g. emulsion and precipitation polymerizations[2,3] as well as shaping and blending of polymers[4,5]. In order to effectively implement carbon dioxide technology in polymer processing, it is necessary to understand the swelling and sorption behavior of polymers in carbon dioxide and the resulting effects on properties such as diffusivity, viscosity, glass transition, melting point, compressibility and thermal expansion.

First, this chapter presents an overview of current techniques for the measurement of sorption and swelling. With the exception of the recent vibrational and spectroscopic techniques, sorption measurements require additional swelling data, which are usually determined separately. Ideally, the sorption and swelling are obtained simultaneously. In paragraph 5.3, we therefore propose a generally applicable method for the simultaneous measurement of sorption and swelling of a single polymer sample under a high-pressure gas atmosphere. The method applies a direct measurement of the volume change of the polymer phase by submersion in an inert liquid. For the determination of the sorption, the barometric method is used, which is an established technique. The implementation of this combined concept in a working apparatus is discussed. Finally, validation experiments focused on the swelling measurement technique are presented. The experiments have been performed on the system poly(ethylene-co-vinyl acetate)-carbon dioxide, which is a rubbery polymer showing rapid sorption of carbon dioxide.

5.2 Current sorption and swelling methods

In literature, various methods are proposed for the measurement of the interactions of supercritical fluids and gases with polymers. Some common techniques for the measurement of sorption and swelling are shown in Figure 5.1.

5.2.1 Sorption

The most applied sorption measurements are based on the gravimetric method and the barometric method. In the gravimetric method, the weight of the polymer sample is measured in situ using a weighing device. In a common technique, the

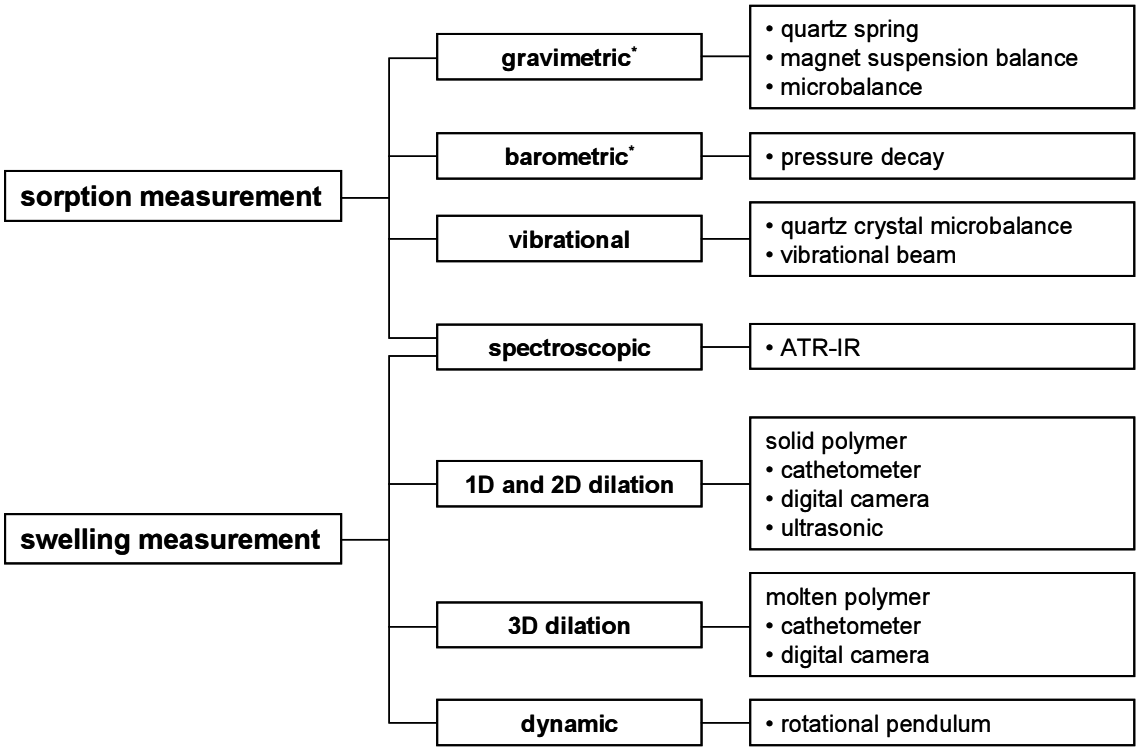

*Figure 5.1 Overview of sorption and swelling measurement methods. *These methods require additional swelling data.*

sample is suspended using a quartz spring[6-8]. The extension of the spring is measured through a view cell window with a cathetometer. Other techniques use balances, such as a microbalance placed inside the pressure cell[9-13] or a balance outside the cell, with the sample magnetically coupled through the cell wall to the balance (magnetic suspension balance)[14-16]. In the gravimetric method, the measurement has to be corrected for buoyancy by

$$\Delta m_{sorp} = \Delta m + \rho_g V_s \tag{5.1}$$

where ρ_g is the gas phase density and V_s is the volume of the swollen polymer sample and the spring or the suspension. The correction for buoyancy requires additional knowledge of the swelling of the polymer at the measurement conditions. Moreover, the buoyancy effects severely limit the use of the technique at high gas pressures and densities.

In the barometric method[17-21], the sample is rapidly pressurized in a calibrated pressure cell, and the pressure decay due to sorption is measured in time. When the equilibrium pressure has been reached, the sorption is determined from the change in gas phase densities by

$$\Delta m = \Delta\rho_g V_g^0 - \rho_g \Delta V_p \tag{5.2}$$

where V_g^0 is the initial gas phase volume and ΔV_p is the swelling of the polymer. The gas phase densities are calculated from the pressures using an accurate equation of state. Similar to the gravimetric method, the barometric method requires additional knowledge of the swelling of the polymer at experimental conditions.

More recently proposed sorption methods are based on vibrational techniques and spectroscopy. Unlike the gravimetric and barometric methods, these methods do not require additional swelling data. The vibrational techniques use the mass dependency of the first harmonic of the resonance frequency. It is well known that the resonance frequency in a vibrating system decreases with increasing mass of the system (see also Chapter 4). By including the sorbing polymer sample into the vibrating system, the increase in mass during sorption can be determined from the change in the resonance frequency. In literature, two applications of this technique are described using a vibrating beam[22,23] and a quartz crystal microbalance[24-26].

In the case of the vibrating beam, the polymer is attached to the tip of a beam, which is excited by an electromagnet. The induced frequency and amplitude of the beam are measured using a strain gauge attached to the beam. Besides the sorbing mass, the frequency is also dependent on the friction of the beam in the gas phase, particularly at high densities, which has to be determined by calibration.

The quartz crystal microbalance uses a similar technique as the vibrating beam. However, in this case the piezoelectric effect is used to excite a polymer coated quartz crystal wafer. The polymer coating (1-3 μm) is applied by (multiple) spin coatings using a solution of the polymer in a volatile solvent.

Recently, Kazarian and coworkers have developed a technique to simultaneously measure sorption and swelling, based on ATR-IR spectroscopy. The method was demonstrated on the system poly(dimethylsiloxane)-carbon dioxide[27]. In this system, the sorption is determined from the increase of the ν_3 band of CO_2 (2335 cm^{-1}). The swelling is determined from the decrease of the $\delta(CH_3)$ band of PDMS (1259 cm^{-1}), as the swelling is causing a lowering of the PDMS concentration. Both bands used are isolated bands that do not overlap with other bands. This enables easier quantification of the absorbance, which allows calculation of the sorption and swelling using the Lambert-Beer law. ATR-IR spectroscopy is applicable as an indirect measurement technique for both sorption and swelling of polymers in supercritical fluids, under the condition that suitable

IR bands are present and that the bands of the polymer and the solute do not overlap.

5.2.2 Swelling and dilation

As discussed above, swelling data can be obtained using ATR-IR spectroscopy for suitable polymers. More common swelling techniques are based on dilation measurements and dynamic measurements.

The most applied swelling measurements are based on the determination of the dilation of a polymer film or strip suspended in a high-pressure view cell. The dilation is usually determined in one or two dimensions using a cathetometer[6-8,17] or a digital camera[15,28]. Under the assumption of isotropic dilation, the swelling of the polymer is obtained from

$$\frac{V}{V_0} = \left(\frac{l}{l_0}\right)^3 - 1 \tag{5.3}$$

The assumption of isotropic dilation can be validated by dilation experiments performed on two samples cut perpendicular to each other from the original film. To check for gravitational elongation due to plasticization, the dilation has to be measured in two dimensions. Recently, Briscoe and coworkers[23] developed a technique using ultrasound to detect the increased thickness of a polymer film upon sorption.

In the case of a molten polymer, the swelling can be determined from the raise of the liquid level in a vessel with known geometry. The liquid level can be observed using a digital camera[29] or a cathetometer[30]. This method allows for a direct measurement of the swelling, without the need for correction of anisotropic dilation. However, as the polymer is enclosed in two dimensions, the diffusion lengths tend to be quite long, resulting in long equilibrium times.

Recently, Keller and coworkers have developed a new dynamic method for the indirect measurement of swelling of a polymer in a high-pressure atmosphere[12]. In this technique, the swelling is determined from the moment of inertia of an oscillating disk. The disk is (partly) filled with polymer and suspended on a thin wire in a high-pressure vessel. The moment of inertia is determined from the angular frequency and the damping of the oscillation. The swelling of the polymer is extracted from the data after a rather complex calibration and assignment of various contributions to the moment of inertia (the polymer, the empty disk, the

boundary layer around the disk, the unsorped gas in the disk and the gas sorped into the polymer).

5.3 Novel method for simultaneous measurement of sorption and swelling

Currently applied techniques for measurement of the phase behavior of polymers in high-pressure gases require the linking of separate sorption and swelling experiments. Usually, these experiments are performed on differently prepared polymer samples. For accurate measurement of sorption and swelling of a polymer in a high-pressure atmosphere, an apparatus is designed to measure both quantities under uniform conditions. Additional requirements are (1) measurement on a single untreated solid polymer sample of arbitrary composition, thus not a cast film, and (2) a direct volume measurement, which is not affected by anisotropic dilation of the polymer.

5.3.1 Simultaneous measurement principle

To fulfill the above requirements, a method has been developed which applies a direct volume measurement by submersion in mercury and an indirect measurement of the sorption by the barometric method. Mercury is used as the measurement fluid, as it shows very low solubilities for gases such as carbon dioxide. The principle of the measurement is shown in Figure 5.2.

The measurement is performed in a pressure cell with a calibrated fixed volume and a defined geometry, i.e. cylindrical. The cell is filled with known amounts of polymer sample and mercury. Initially, the polymer is submerged in the mercury at the measurement temperature and pressure. In this state, the mercury separates

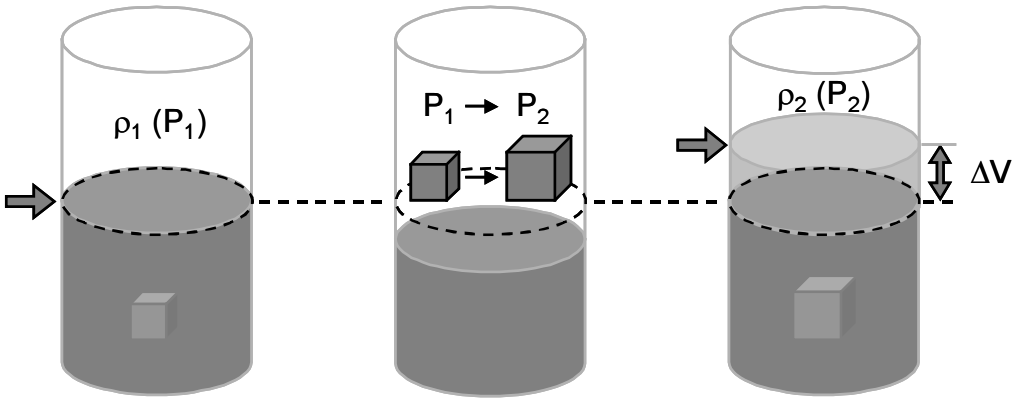

Figure 5.2 Principle of simultaneous measurement of sorption and swelling by pressure decay and mercury displacement.

the polymer from the gas phase, preventing sorption of the gas into the polymer. By measuring the height of the mercury level, the unswollen volume of the polymer is marked. The gas phase density in the system is obtained from the pressure using an accurate empirical equation of state, e.g. for carbon dioxide the IUPAC eos[31].

Subsequently, the polymer is moved from the mercury to the gas phase. In this stage, the polymer sample is directly exposed to the gas phase, causing it to reach a certain sorption and swelling level, which depends on the composition of the polymer. As the partial molar volume of the gas in the polymer usually differs from the specific molar volume of the gas phase, the sorption of the gas into the polymer will alter the gas phase density, and thereby the pressure. Therefore, the pressure of the system is monitored in time and equilibrium is reached when the pressure is constant. Additionally, in the case of a suitable polymer geometry, e.g. spherical, the diffusion coefficient of the gas relative to the stationary polymer can be calculated from the pressure-time curve.

Finally, the polymer is resubmerged into the mercury and the height of the mercury level is measured, marking the swollen volume of the polymer. The absolute amount of swelling of the polymer is directly obtained from the difference in the mercury levels and the vessel geometry. As it is a closed system, the decrease in volume of the gas phase is equal to the increase in volume of the polymer sample, assuming no gas is sorped by the mercury and the volume of the mercury is unchanged. Combined with the equilibrium pressure and the density calculated from this pressure, the sorption is determined from a mass balance for the gas component.

Using this method with a cylindrical mercury displacement, i.e. in a tube, the swelling and the sorption of the polymer are given by

$$\phi_v = \frac{V_{p,2}}{V_{p,1}} - 1 = \frac{1}{4}\pi d^2 \left(h_2 - h_1\right) \tag{5.4}$$

$$\phi_w = \frac{m_{p,2}}{m_{p,1}} - 1 = V_{g,1}\left(\rho_{g,2} - \rho_{g,1}\right) - \rho_{g,2} V_{p,1} \phi_v \tag{5.5}$$

where ϕ_v is the swelling, ϕ_w is the sorption and d and h are the mercury displacement diameter and height, respectively.

5.3.2 Apparatus for simultaneous measurement

The swelling measurement described above is based on changing a polymer sample from a state in which it is submerged in mercury to a state in which it is exposed to the gas phase. After reaching equilibrium, the sample is resubmerged in mercury. To accomplish this behavior in a practical manner, the system is set-up as a closed loop containing two small vessels. One vessel contains the polymer sample and the other one is used as buffer vessel for mercury. Instead of moving the polymer in and out of the gas phase, the mercury is positioned in such a way that the polymer is either submerged or exposed to the gas phase, as shown in Figure 5.3. In the first position, the polymer is submerged in mercury and the height of the mercury level is determined in the tubing between the vessels. In the second position, the mercury is forced to the left side of the loop. In this position, the mercury occupies the buffer vessel and the polymer is exposed to the gas phase. After releasing the mercury, it flows back to the initial position under its own weight. With the swollen polymer resubmerged, the final mercury level can be obtained.

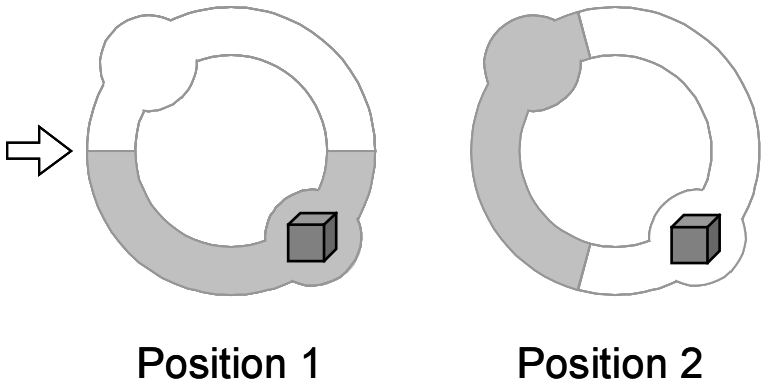

Figure 5.3 Positions of the mercury with the polymer submerged and gas-exposed.

The measurement loop is implemented in the system as shown in Figure 5.4. The apparatus is divided into two sections, a closed measurement loop and a gas supply. The measurement loop contains two vessels. The lower vessel is used as a sample vessel and is constructed for easy refilling with the polymer sample. The upper vessel is a closed vessel used for buffering mercury. The sample vessel and the buffer vessel have volumes of 7.6 mL and 8.8 mL, respectively. The measurement loop is constructed from tubing with an inner diameter of 1.00 mm and the total volume of the empty loop is 18.0 mL. The loop is constructed for operation up to 1000 bar at 423 K.

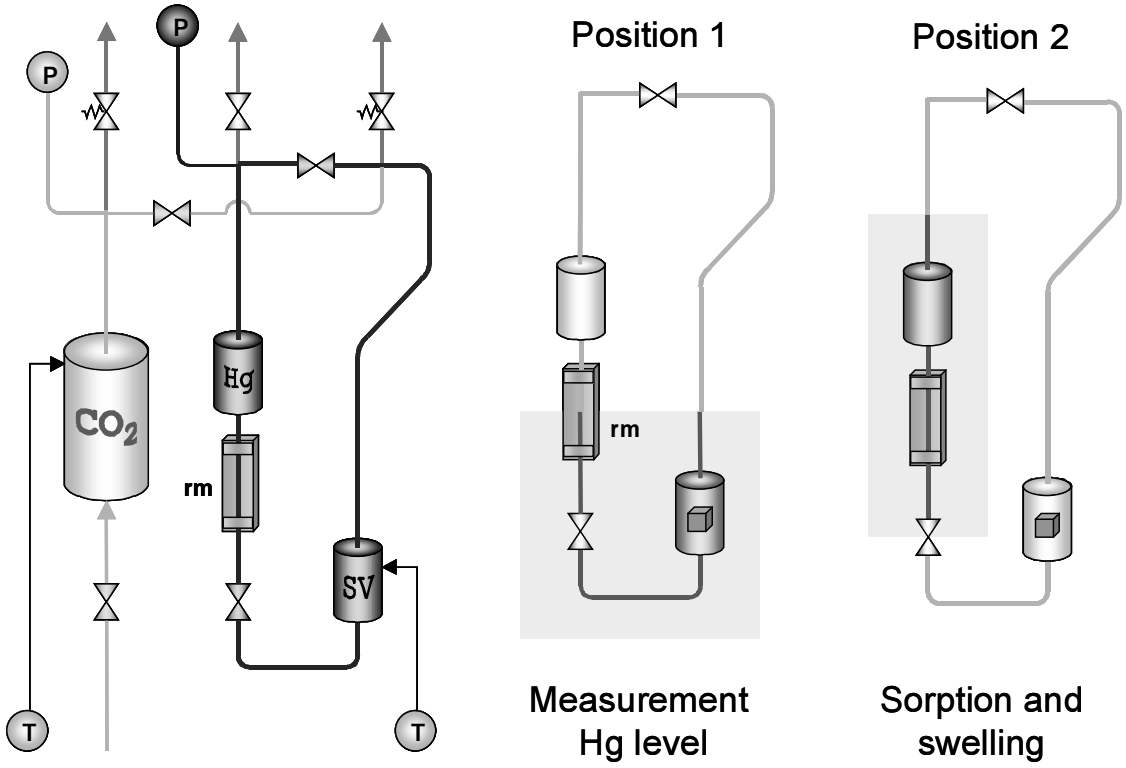

Figure 5.4 Schematic representations of the sorption and swelling apparatus and the mercury positions in the apparatus.

To enable positioning of the mercury, a valve is present in the tubing between the two vessels. In the detection position (position 1), the height of the mercury is measured using a resonance technique. Just below the mercury buffer vessel, a section of 160 mm of the tubing is clamped. By exciting the clamped section, the resonance frequency of the clamped tubing is determined. The resonance frequency is strongly dependent on the mass density of the tube and thus directly related to the height of the mercury. However, due to the clamping of the tubes, reliable detection of the mercury is not possible in the first quarter and the last quarter of the tube, effectively limiting the detection length to 80 mm in this particular setup. This corresponds to absolute swelling volumes up to 0.126 mL. Figure 5.5 shows the Bernoulli-Euler model curve of the height of the mercury as a function of the relative frequency change. A complete description of the resonance detection is given in Chapter 4. Note that the tubing at the left side and the right side of the loop are identical, thus canceling any effects of capillary action.

The gas supply contains a buffer vessel with a volume of 106 mL for rapid filling of the measurement loop. The gas supply section is constructed for operation up to 1200 bar at 423 K. Both the loop and the gas supply are equipped

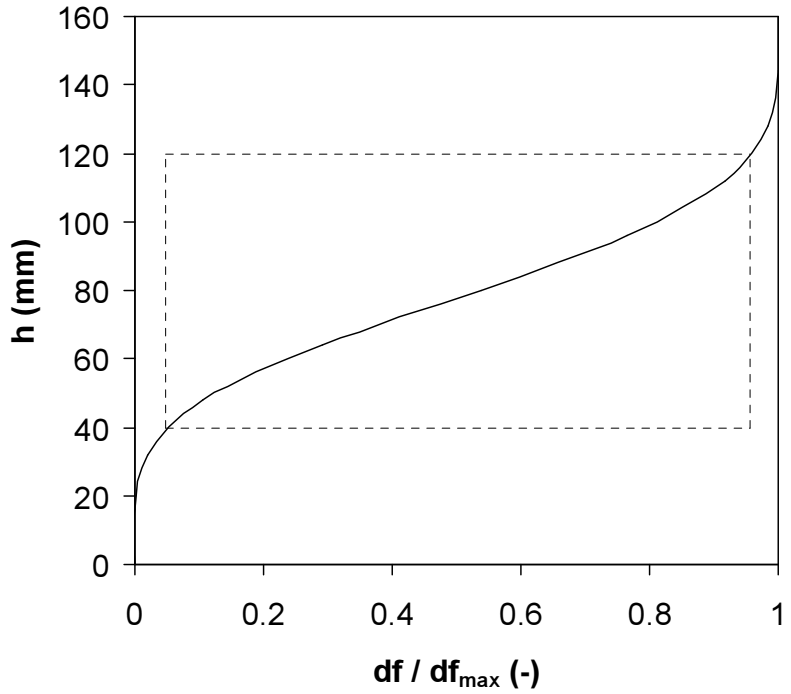

Figure 5.5 Height of the mercury as indicated by the relative frequency change. The measurement window is marked by the dotted lines.

with a pressure indicator and break valves. The system is pressurized using a syringe pump (Isco Inc.) with a maximum pressure of 689 bar (10,000 psi). The whole apparatus is set-up in an oven (Venticell). The apparatus, including the vessels, was manufactured by the DelftChemTech workshop (DCT/AG).

5.4 Experimental

5.4.1 Materials

Poly(ethylene-co-vinyl acetate) (EVA) 40 wt% vinyl acetate was purchased from Aldrich Chemical Company. GPC analysis with a polystyrene standard indicated an M_n of 55,000 and a polydispersity of 2.3. The glass temperature and the melting temperature as determined by DSC analysis revealed a glass temperature of 235 K and two melting temperatures at 328 K and 342 K, respectively. ^{1}H NMR analysis of the EVA showed a copolymer composition of 38 ± 1 wt% VA. Carbon dioxide (grade 4.5) was obtained from Hoekloos (Amsterdam, The Netherlands) and was used without further purification.

5.4.2 Methods

For practical reasons, the apparatus was separately validated for swelling and sorption measurements. Subsequent developments of the apparatus will allow for simultaneous measurement of sorption and swelling.

For the swelling experiments, the initial EVA beads were molten into films of thickness 1.5-2.0 mm. From these films, samples were cut of 3-7 mm by 20-30 mm (sample weights 0.1-0.3 g). Prior to each measurement, the loop, including the vessels, was cleaned to remove any mercury(oxide) from previous experiments. Subsequently, the sample vessel was loaded with an EVA sample and the frequency of the empty tube was determined. During the filling of the loop with mercury, the frequency of the full tube was determined. The loop was filled with mercury up to a height of approximately 40 mm in the resonance measurement section and the start frequency and height were determined. Next, the mercury was carefully pushed to the left side of the loop (position 2) by manually applying a small pressure at the right side of the loop, and the position was fixed by closing the valve below the resonance section. In this position, the polymer is exposed to the gas phase. After closing the loop, the system was pressurized with carbon dioxide, with the pressure controlled by the pump. After reaching equilibrium, typically within 4 hours, the mercury was released by opening the valve below the resonance section. With the mercury in position 1, the resonance frequency was determined to obtain the final height of the mercury.

The sorption experiments were performed on the unmodified EVA beads, without mercury present in the loop. Therefore, the sample vessel was filled with a weighted amount of EVA and the system was closed. Next, the buffer vessel in the gas supply was filled with carbon dioxide at such a pressure, that after expansion into the measurement loop, the desired pressure was reached. The sorption experiment was started by rapidly filling the measurement loop with the carbon dioxide from the buffer vessel. Subsequently, the pressure decay was recorded in time, from which the sorption level and the diffusion coefficient relative to the stationary polymer were obtained.

5.5 Results and discussion

A key element of the apparatus is the level detection of the mercury in a capillary part of the system. This is accomplished using the mass dependence of the resonance frequency of the tube. In Chapter 4, it is shown that the vibration of

a tube partly filled with liquid can be described with the Bernoulli-Euler model and that the equation of motion is given by

$$EI\frac{\partial^4 y_i}{\partial x^4} + m_i \frac{\partial^2 y_i}{\partial x^2} = 0 \tag{5.6}$$

From this equation, it is clear that besides the mass density in the tube, the resonance frequency is dependent on the bending stiffness *EI* of the tube. The effects of varying bending stiffness have been encountered in the measurements. Between measurements, the set-up was repeatedly disassembled and cleaned. Due to variations in tension and torsion of the build-in tube after reassembling, the resonance frequency of the empty tube differed for each measurement. In addition, the applied pressure can cause variations in the tension of the tube. To study this effect, the resonance frequency of the tube only filled with carbon dioxide was measured as a function of pressure. The results are shown in Figure 5.6 for a measurement at 293 K. The frequency appears to be independent of the applied pressure. However, at 57 bar a significanty change in frequency is visible.

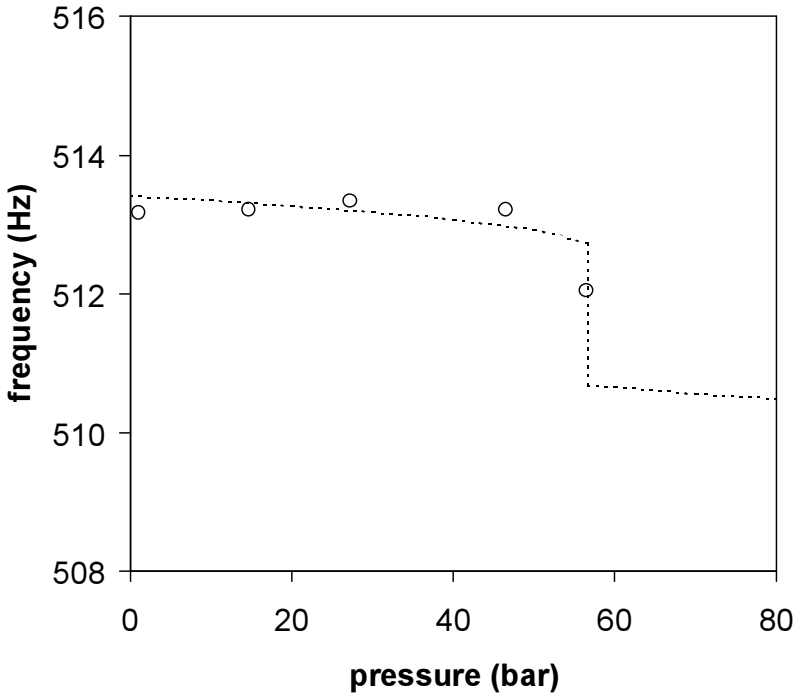

Figure 5.6 The resonance frequency of a tube filled with carbon dioxide at 293 K as a function of pressure; measurements (o) *and Bernoulli-Euler model (---).*

This drop of approximately 1.2 Hz is caused by a (partial) filling of the tube with liquid of carbon dioxide, which leads to an abrupt increase in fluid density. Consequently, the resonance frequency of the empty tube can be determined at ambient pressures, whereas the value for higher pressures is obtained by a correction for the increased fluid density in the tube.

After establishing the pressure independence of the resonance frequencies, the apparatus has been tested for the volume measurement by mercury submersion. Therefore, the volumes of small steel rods with known volumes have been measured in the apparatus. In Figure 5.7, the volumes measured by submersion in mercury are presented as related to the actual volumes of the steel samples. Theoretically, all points should fall on the diagonal line. For the larger samples, i.e. volumes above 0.07 mL, this is indeed the case. However, for the smaller samples the measured volume is smaller than the actual volume. This is possibly caused by mercury remaining in the buffer vessel, although persistently low values obtained for successive measurements indicate a systematic deviation at small volumes. Consequently, volume measurements are restricted to the measurement window

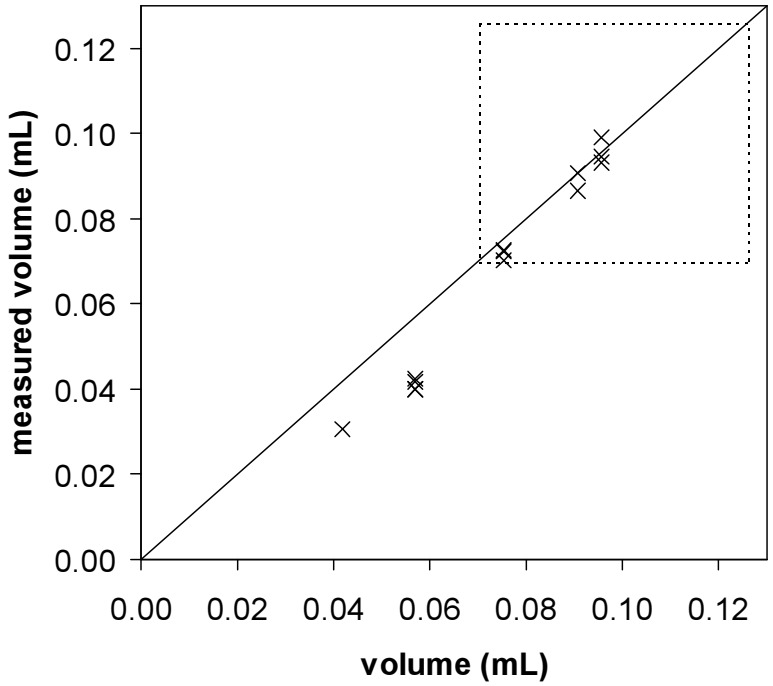

Figure 5.7 Calibration of the volume measurement on steel sample volumes (ambient pressures).

shown in Figure 5.7. The mercury holdup in the buffer vessel is a reoccurring issue. As the mercury is exposed to air for prolonged periods, the surface is oxidized. This mercury oxide has the tendency to stick to the wall of the vessel, where it enables wetting of the wall surface with mercury. Therefore, after each measurement, the system is cleaned in order to remove any mercury(oxide) remains. As mentioned above, the swelling experiments and the sorption experiment have been performed separately. The results of a test series of swelling experiments of carbon dioxide in EVA at 293 K are shown in Figure 5.8. For comparison, the sorption isotherms of the same system are also shown for the temperatures 323 K and 348 K. These have been measured using a cathetometer, as described in Chapter 3. As expected, the swelling isotherm obtained at 293 K increases with pressure, and appears to be above the isotherms at 323 K and 348 K.

The apparatus has also been used to measure the sorption of carbon dioxide in EVA. Therefore, the pressure has been monitored in time. This is shown in Figure 5.9a for the system EVA-CO_2 at 293 K. The pressure initially declines rapidly and reaches equilibrium after approximately one hour. Assuming a swelling level of 0.45, the sorption can be calculated using Equation 5.5. As a result, a value of

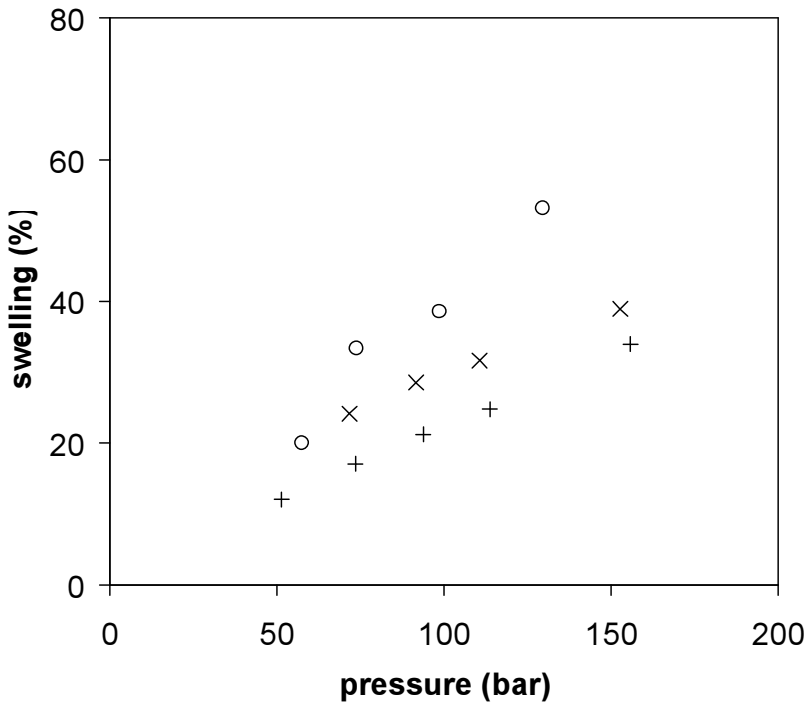

Figure 5.8 Swelling of EVA in carbon dioxide at 293 K (o), compared to the same system measured at 323 K (×) and 348 K (+) using a cathetometer, as described in Chapter 3.

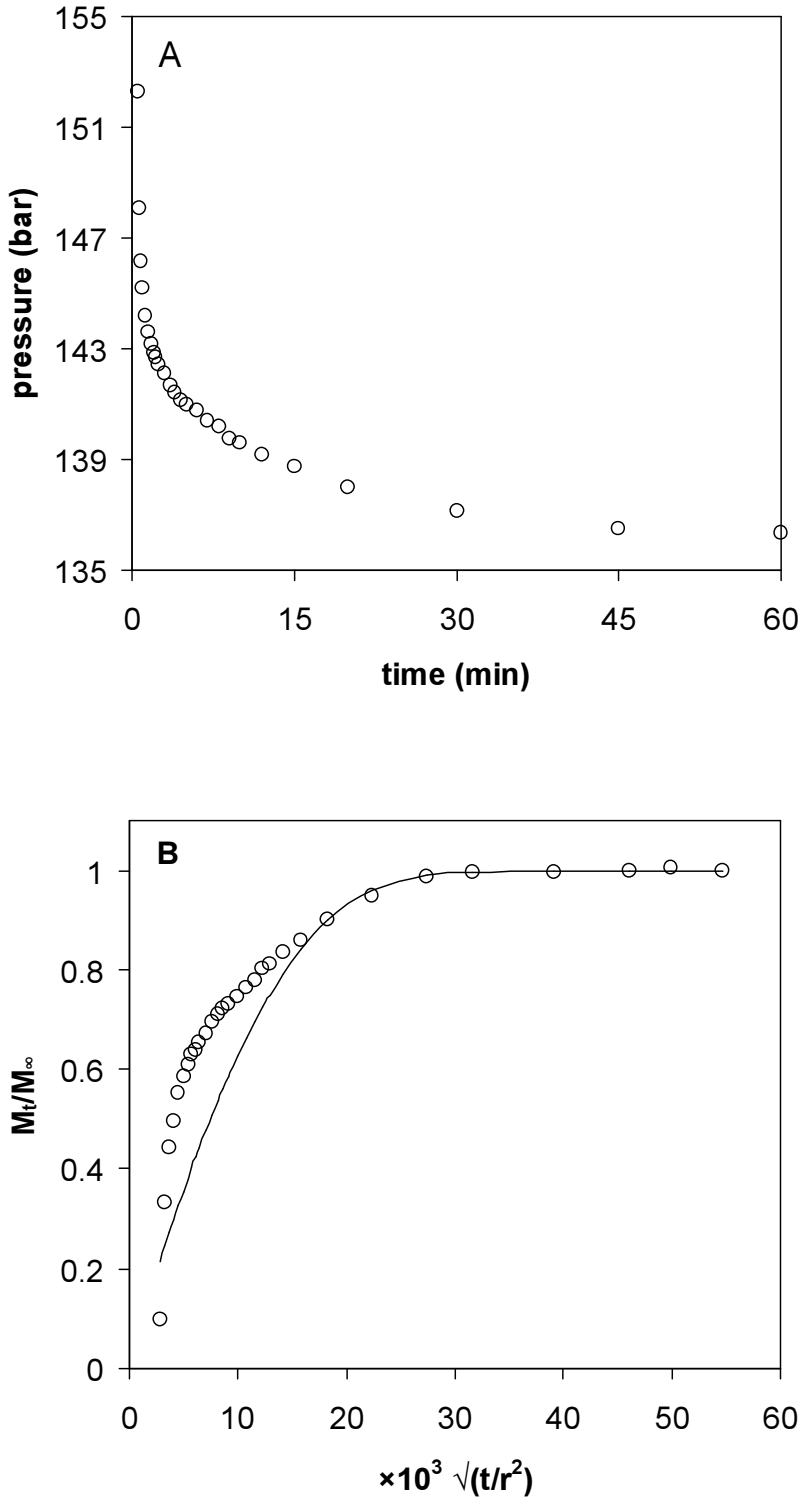

Figure 5.9 Sorption kinetics of carbon dioxide in EVA at 293 K. A) pressure decay; B) normalized sorption kinetics, the line is calculated for spherical Fickian diffusion (Eq. 3.3)

51 wt% for the sorption is obtained. The normalized sorption curve is shown in Figure 5.9b. By fitting Fickian diffusion Equation 3.3 to the data, an estimate of the diffusion coefficient of carbon dioxide in EVA can be calculated. For the data shown in Figure 5.9b, a value of 5.5×10^{-10} m^2/s is obtained, which is in agreement with previous measurements on the same polymer at 323 K[30]. However, the value here is obtained by fitting the second half of the sorption curve only. The initial part of the curve deviates substantially from normal diffusion behavior. Probably, this is caused by the thermal effects due to the rapid expansion of the carbon dioxide from the buffer vessel into the measurement loop.

5.6 Conclusions

A novel technique for the simultaneous measurement of sorption and swelling of solid polymers in high-pressure gases has been proposed. In this technique, the swelling of the polymer is directly measured by submersion in a liquid. The sorption of the polymer is obtained using the barometric method. The technique has been implemented into an apparatus using mercury as the measurement fluid. Evaluation measurements on the system carbon dioxide-poly(ethylene-*co*-vinyl acetate) show that the apparatus is able to measure both the swelling and the sorption of the polymer. Additionally, from the sorption kinetics, an estimate of the diffusion coefficients can be obtained.

5.7 References

1. A.I. Cooper, *J. Mat. Chem.* **10** (2000) 207.
2. J.L. Kendall, D.A. Canelas, J.L. Young and J.M. DeSimone, *Chem. Rev.* **99** (1999) 543.
3. T.J. de Vries, R. Duchateau, M.A.G. Vorstman and J.T.F. Keurentjes, *Chem. Comm.* (2000) 263.
4. S. Mawson, K.P. Johnston, J.R. Combes and J.M. DeSimone, *Macromolecules* **28** (1995) 3182.
5. T.A. Walker, S.R. Raghavan, J.R. Royer, S.D. Smith, G.D. Wignall, Y. Melnichenko, S.A. Kahn and R.J. Spontak, *J. Phys. Chem. B* **103** (1999) 5472.
6. R.G. Wissinger and M.E. Paulaitis, *J. Polym. Sci. B* **25** (1987) 2497.
7. Y. Zhang, K.K. Gangwani and R.M. Lemert, *J. Supercrit. Fluids* **11** (1997) 115.
8. S.H. Chang, S.C. Park and J.J. Shim, *J. Supercrit. Fluids* **13** (1998) 113.
9. Y. Kamiya, K. Terada, K. Mizoguchi and Y. Naito, *Macromolecules* **25** (1992) 4321.
10. J.S. Wang, Y. Naito and Y. Kamiya, *J. Polym. Sci. B* **34** (1996) 2027.
11. Y. Kamiya, K. Mizoguchi, K. Terada, Y. Fujiwara and J.S. Wang, *Macromolecules* **31** (1998) 472.

12. J.U. Keller, H. Rave and R. Staudt, *Macromol. Chem. Phys.* **200** (1999) 1.
13. B. Wong, Z. Zhang and Y.P. Handa, *J. Polym. Sci. B* **36** (1998) 2025.
14. O. Pfannschmidt and W. Michaeli, In proceedings *ANTEC '98*, Atlanta, 1998, p. 1918.
15. J. von Schnitzler and R. Eggers, *J. Supercrit. Fluids* **16** (1999) 81.
16. Y. Sato, T. Takikawa, A. Sorakubo, S. Takishima, H. Masuoka and M. Imaizumo, *Ind. Eng. Chem. Res.* **39** (2000) 4813.
17. I.S. Liau and M.A. McHugh, In *Supercritical Fluid Technology*, Elsevier Science Publishers, Amsterdam, 1985, p. 415.
18. G.K. Fleming and W.J. Koros, *Macromolecules* **19** (1986) 2285.
19. D.S. Pope, I.C. Sanchez, W.J. Koros and G.K. Fleming, *Macromolecules* **24** (1991) 1779.
20. D.S. Pope and W.J. Koros, *J. Polym. Sci. B* **34** (1996) 1861.
21. M.G.D Angelis, T.C. Merkel, V.I. Bondar, B.D. Freeman, F. Doghieri and G.C. Sarti, *J. Polym. Sci. B* **37** (1999) 3011.
22. B.J. Briscoe and H. Mahgerefteh, *J. Phys. Experim. Sci. Instr.* **17** (1984) 483.
23. B.J. Briscoe, O. Lorge, A. Wais and P. Dang, *J. Polym. Sci. B* **36** (1998) 2435.
24. D.C. Bonner and Y. Cheng, *J. Polym. Sci., Polym. Letters* **13** (1975) 259.
25. N.H. Wang, S. Takishima and H. Masuoka, *Int. Chem. Eng.* **34** (1994) 255.
26. J.H. Aubert, *J. Supercrit. Fluids* **11** (1998) 163.
27. N.M.B. Flinchy, S.G. Kazarian, C.J. Lawrence and B.J. Briscoe, *J. Polym. Sci. B* **106** (2002) 754.
28. L.N. Nikitin, E.E. Said-Galiyev, R.A. Vinokur, A.R. Khokhlov, M.O. Gallyamov and K. Schaumberg, *Macromolecules* **35** (2002) 934.
29. J.R. Royer, J.M. DeSimone and S.A. Khan, *Macromolecules* **32** (1999) 8965.
30. M.A. Jacobs, M.F. Kemmere and J.T.F. Keurentjes, *submitted for publication.*
31. S. Angus, B. Armstrong and K.M. de Reuck, *International tables of the Fluid State: Carbon Dioxide*, Pergamon Press, Oxford, 1976.

CHAPTER 6

FUTURE CHALLENGES IN MEASUREMENT AND MODELING OF POLYMER-SUPERCRITICAL FLUID SYSTEMS

Abstract

In this thesis, several aspects concerning the processing of polymers in supercritical fluids have been discussed. In this chapter, some remaining challenges in both measurement and modeling of polymer-supercritical fluid systems will be discussed. With the insight gained from the development of the apparatus for the simultaneous measurement of sorption and swelling, as described in Chapter 5, a revised concept for the apparatus is presented. Subsequently, some modeling aspects of the partitioning behavior in aqueous-supercritical fluid two-phase systems are discussed. These systems are encountered in the extraction of polymer latices with $scCO_2$. Additionally, recent thermodynamic consistency issues using the Sanchez-Lacombe model are addressed. Furthermore, the modeling of supercritical mixtures using excess data as well as the effects of polydispersity on polymer-supercritical fluid systems is described. At the end of this chapter, some future applications of molecular dynamics in polymer systems are discussed.

Parts of this chapter have been submitted as: M.F. Kemmere, M.A. van Schilt, R.M. Wering, M.A. Jacobs and J.T.F. Keurentjes, Partitioning of methyl methacrylate over water and pressurized carbon dioxide; measurements and predictions with the Peng-Robinson equation of state.

6.1 Revised concept for a sorption and swelling apparatus

In Chapter 5, a new technique for the simultaneous measurement of sorption and swelling using a submersion method for the swelling and the barometric method for the sorption has been presented. During the building and subsequent testing of the apparatus, several issues in the design and implementation of the technique have been encountered. One of the main difficulties is the non-wetting behavior of mercury on steel surfaces and the resulting capillary action of the mercury in narrow spaces of the apparatus. Figure 6.1 illustrates some potential causes for the occurring measurement errors. The first issue is the capillary action near sharp corners. Situations such as in Figure 6.1a occur typically near the copper seal ring in the sample vessel and in voids present in the valves. At ambient pressures, when the initial mercury level is determined, these voids are filled with gas. However, at higher pressures, mercury is pressed into the voids, thereby lowering the final mercury level. Consequently, the measured volume changes are underestimated. Fortunately, the surface of the copper seal rings is rapidly covered with amalgam, which completely wets with mercury, reducing capillary action effects.

A second wetting issue that can be encountered is shown in Figure 6.1b. In these situations, a local wetting of the steel surface with mercury occurs. Due to this wetting, the mercury adheres to the wall. This prevents the mercury from flowing under its own weight at shallow angles. The local wetting can be caused by the presence of mercury oxide or by grease on the surface. Unfortunately, the former is difficult to prevent, as mercury is readily oxidized by air at ambient conditions. Therefore, prior to measurements, the apparatus has to be cleaned to remove any remaining mercury oxide. The wetting of steel surfaces is mainly an issue on the bottom of the mercury buffer vessel, where it prevents the mercury to flow completely back in the lower half of the measurement loop.

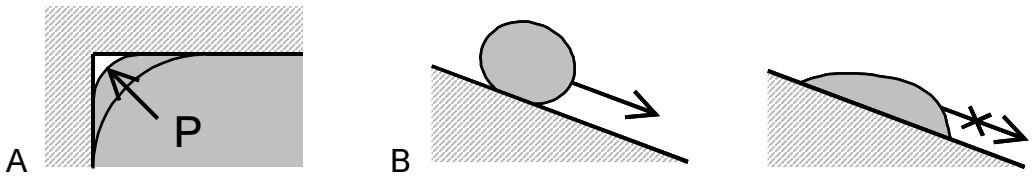

Figure 6.1 Wetting issues of mercury on steel which influence the measurements; A) capillary action near sharp corners; B) wetting of the surface due to mercury oxidation or grease.

An additional point of concern, although not directly affecting the measurements, implies the expansion of the system. At the end of a measurement cycle, the swollen polymer is submersed in the mercury. During depressurization of the gas phase, the polymer releases the sorped gas. As the sample vessel containing the polymer is completely filled with mercury, the released gas forces some mercury through the tubing out of the system. During the expansion, this mercury has to be collected from the exit stream.

To address the above-mentioned difficulties, a revised concept for the sorption and swelling apparatus is proposed. This concept maintains the measurement principles of submersion for the determination of swelling and pressure decay for sorption. However, the whole system is constructed in one single pressure cell, as shown in Figure 6.2.

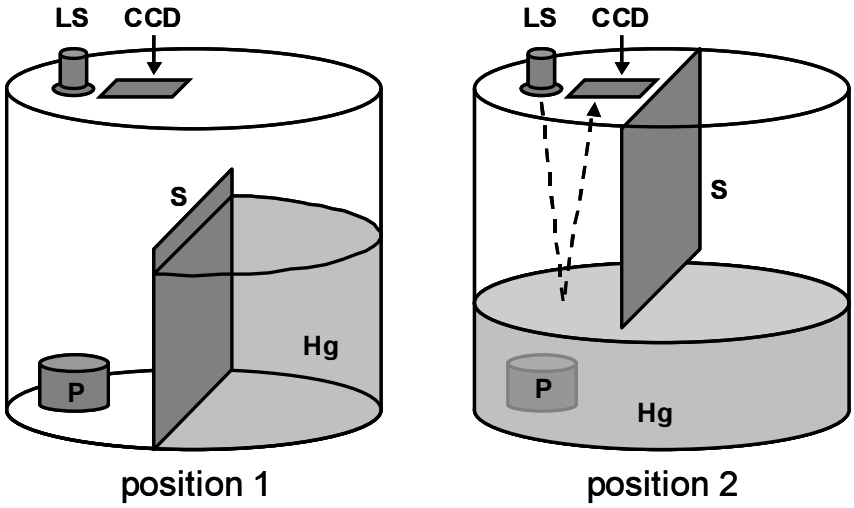

Figure 6.2 Schematic representation of a concept apparatus for the simultaneous measurement of sorption and swelling of a single polymer sample (P) using mercury (Hg) in two positions in the apparatus. The apparatus is equipped with a light source (LS), a camera (CCD) and a slide (S) that controls the release of the mercury.

The apparatus described in Chapter 5 uses the resonance frequency of a capillary part of the system to measure the height of the mercury. The new concept uses a reflecting laser beam for determination of the height of the mercury. This allows for a setup without mercury flowing through narrow tubes, thus avoiding problems with capillary action and wetting. Additionally, the apparatus can be constructed much more compact than the current setup, while retaining a similar gas volume (20-30 mL).

The new setup consists of a cylindrical pressure vessel, which is vertically divided into two sections using a slide. In the first position, with the slide down, the mercury is contained in one half of the cylinder. In this position, the polymer is exposed to the gas phase and the sorption can be determined by pressure decay. For the measurement of sorption, the volume of the cell and the initial volumes of the polymer and the mercury are required. In the second position, with the slide up, the mercury occupies the bottom part of the whole vessel. To prevent floating of the polymer sample on top of the mercury, the sample is attached to the bottom of the vessel. In this position, the height of the mercury is determined using the reflection of a beam of light from the surface of the mercury. The reflected beam is detected on the top of the vessel using photocells (CCD) or a digital camera. As shown in Figure 6.3, the height of the mercury can be determined from the horizontal position of the beam. With a known reflection angle, the height is given by

$$\Delta h = \tfrac{1}{2} \Delta x \tan \alpha \tag{6.1}$$

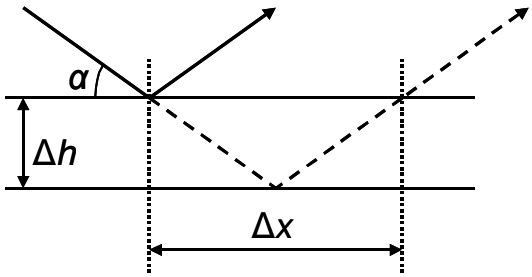

Figure 6.3 Measurement of the fluid height by reflection of a light beam.

This concept avoids problems of wetting and capillary action, as minimal flow restrictions are applied on the mercury. However, the oxidation of the mercury remains an issue in this setup, as it renders the surface of the mercury matte, thereby hindering the reflection. Additionally, the use of light reflection for the mercury level detection requires the cell to be equipped with windows, which allow for a maximum operating pressure of approximately 300-350 bar.

The use of the slide in the concept as a means of controlling the flow of the mercury does introduce some constructional complexity, as the slide has to be operated from outside the pressure cell. However, it circumvents the use of valves in the setup, thereby preventing flow restrictions and possible dead volumes. The issue of expansion is resolved as the gas released from the polymer can leave the vessel without forcing the mercury out of the vessel.

The concept can easily be extended with additional spectroscopy measurements by equipping the cell with two opposing windows. Using e.g. UV-VIS or IR, the composition of the gas phase can be measured. This allows for determination of the partitioning of solutes over the polymer phase and the gas phase, without sampling the gas phase.

Both the apparatus described in Chapter 5 and the concept presented here, use the method of pressure decay for the determination of the sorption of the polymer phase. This technique uses a rapid pressurization of the cell to allow for the determination of the initial pressure. Unfortunately, due to this rapid pressurization, large temperature effects can arise, which affect the initial pressure and thus the calculated initial gas phase density. To enhance the accuracy of the sorption measurements, additional sorption experiments can be performed using the vibrational techniques described in Section 5.2.1. These techniques allow for accurate independent determination of the sorption, without prior knowledge of the volume or the swelling behavior.

6.2 Modeling partitioning behavior of MMA in aqueous scCO$_2$ systems

Emulsion polymerization is widely used in the production of water-based paints, synthetic rubbers, coatings and adhesives[1]. Generally, in these emulsion polymerizations high reaction rates are obtained. However, at the end of the polymerization, the reaction rate usually decreases significantly due to diffusion limitation of the monomer in the polymer particles[2]. As a result, substantial amounts of residual monomer are present in the product. For environmental and health reasons, the monomer concentrations need to be reduced prior to end-use of the polymer product. Reduction of the residual monomer in polymer products can be achieved by conversion or by removal of the monomer[3]. *Conversion* of the residual monomer usually occurs in post-processing tanks at increased temperatures around 348 K, whereas the actual polymerization typically takes place at 323 K. These end-conversion processes are energy-intensive and time-consuming.

Common techniques for residual monomer *removal* include stripping and pervaporation. A viable alternative for stripping and pervaporation is the extraction of residual monomer from latex using supercritical carbon dioxide. As shown in Chapter 1, carbon dioxide has a high solubility for small components such as monomers at process-wise acceptable pressures. Additionally, the solubility of water in carbon dioxide is very limited. Furthermore, carbon dioxide

readily swells common polymers such as PMMA, thereby enhancing monomer diffusivity in the polymer.

In order to obtain insight in the extraction behavior of monomers from aqueous systems and to reduce experimental efforts, the partitioning behavior of MMA in the system water-scCO$_2$ systems has been modeled using the Peng-Robinson equation-of-state. The equation-of-state has been used as implemented by the computer program Phase Equilibria, which has been developed by Brunner and co-workers at the Technical University of Hamburg[4].

6.2.1 Equation-of-state and mixing rules

The Peng-Robinson equation-of-state (PR eos)[5] is one of the most frequently used semi-empirical cubic equations of state, which is able to describe high-pressure and supercritical fluid systems. The PR eos expresses pressure as a summation of a repulsive term and a attractive term and is given by

$$P = P_R + P_A = \frac{RT}{v-b} - \frac{a(T,\omega)}{v(v+b)+b(v-b)} \tag{6.2}$$

where a reflects the temperature dependent intermolecular attraction and b reflects the Van der Waals hard sphere volume. For pure components a and b are given by

$$a = 0.45724\frac{(RT_c)^2}{P_c}\left(1+\left(0.37464+1.54226\omega-0.26992\omega^2\right)\left(1-\sqrt{T_r}\right)\right)^2 \tag{6.3}$$

$$b = 0.07780\frac{RT_c}{P_c} \tag{6.4}$$

where T_r is the reduced temperature and ω the acentric factor.

For the description of multi-component systems, the parameters a and b can be obtained from mixing rules:

$$a_m = \sum_i \sum_j x_i x_j a_{ij} \qquad b_m = \sum_i \sum_j x_i x_j b_{ij} \tag{6.5}$$

Various expressions have been proposed for the cross coefficients a_{ij} and b_{ij}, which are shown in Table 6.1.

The quadratic mixing rule is only applicable to mixtures of similar components showing no specific interactions. The Panagiotopoulos-Reid[6] and Stryjek-Vera[7]

Table 6.1 Cross-coefficients a_{ij} and b_{ij} for various mixing rules.

Mixing rule	Parameter *a*		Parameter *b*
Quadratic	$a_{ij} = \sqrt{a_i a_j}\left(1 - k_{ij}\right)$	$k_{ij} = k_{ji}$	$b_{ij} = \frac{b_i + b_j}{2}\left(1 - \ell_{ij}\right)$ $\ell_{ij} = \ell_{ji}$
Panagiotopoulos-Reid	$a_{ij} = \sqrt{a_i a_j}\left(1 - k_{ij} + \lambda_{ij} x_i\right)$	$\lambda_{ij} = k_{ij} - k_{ji}$	
Stryjek-Vera	$a_{ij} = \sqrt{a_i a_j}\left(1 - \frac{k_{ij} k_{ji}}{x_i k_{ij} + x_j k_{ji}}\right)$		
Melhem	$a_{ij} = \sqrt{a_i a_j}\left(1 - k_{ij} + \lambda_{ij} \frac{x_i}{x_i + x_j}\right)$		
Mathias-Klotz-Prausnitz	$a_m = \sum_i \sum_j x_i x_j \sqrt{a_i a_j}\left(1 - k_{ij}\right) + \sum_i x_i \left(\sum_j x_j \left(\sqrt{a_i a_j}\lambda_{ij}\right)^{1/3}\right)^3$	$k_{ij} = k_{ji}$ $\lambda_{ij} = -\lambda_{ji}$	

mixing rules introduce a second parameter for *a*, thereby enabling description of non-symmetrical behavior. Both these mixing rules suffer from a so-called dilution problem and the Michelsen-Kistenmacher syndrome[8]. Melhem et al.[9] proposed a mixing rule that solved the dilution problem. The Mathias-Klotz-Prausnitz mixing rule[10] is an extension of the Panagiotopoulos-Reid mixing rule, without the dilution problem or the Michelsen-Kistenmacher syndrome. Moreover, when applied to binary mixtures, it becomes identical to the Panagiotopoulos-Reid mixing rule. As shown in Table 6.1, b_{ij} is identical for all mixing rules and generally ℓ_{ij} is set to zero.

The computer program Phase Equilibria[4] includes the Peng-Robinson equation-of-state and the above described mixing rules, thereby allowing a complete description of the phase equilibria of the ternary system and its subsystems.

Partition coefficients obtained from extraction experiments are based on volumetric concentrations and are defined as

$$k = \frac{c_{MMA}^{scf}}{c_{MMA}^{aq}} = \frac{y_{MMA}\rho_n^{scf}}{x_{MMA}\rho_n^{aq}} \tag{6.6}$$

where x and y are mole fractions and ρ_n is the molar phase density. As shown in Equation (6.6), phase densities are required for the calculation of the partition coefficients from the equilibrium mole fractions. Liquid phase densities as calculated by the Peng-Robinson eos show large deviations (approx. 15%), resulting in erroneous partition coefficients. Therefore, the density of the aqueous phase is assumed pure water and is calculated using a Modified Benedict-Webb-Rubin (MBWR) eos.

6.2.2 Experimental data

In the modeling of multi-component phase equilibria using mixing rules, binary interaction parameters are required for each set of two components. The binary interaction parameters for the subsystems present in the ternary H_2O-MMA-CO_2 system were obtained from a fit to the binary VLE data from literature[11-15].

Experimental partition data of MMA in the system water-carbon dioxide was obtained using a high-pressure extraction unit with in-line sampling of the aqueous phase. A detailed description of the equipment and experimental procedures is given by Kemmere et al.[16] It should be noted that, between 58 bar and 63 bar at 298 K a three-phase system was observed in high-pressure view-cell experiments, similar to observations by Adrian et al.[17] As the liquid phase is sampled in the extraction unit, this region was excluded from the extraction measurements.

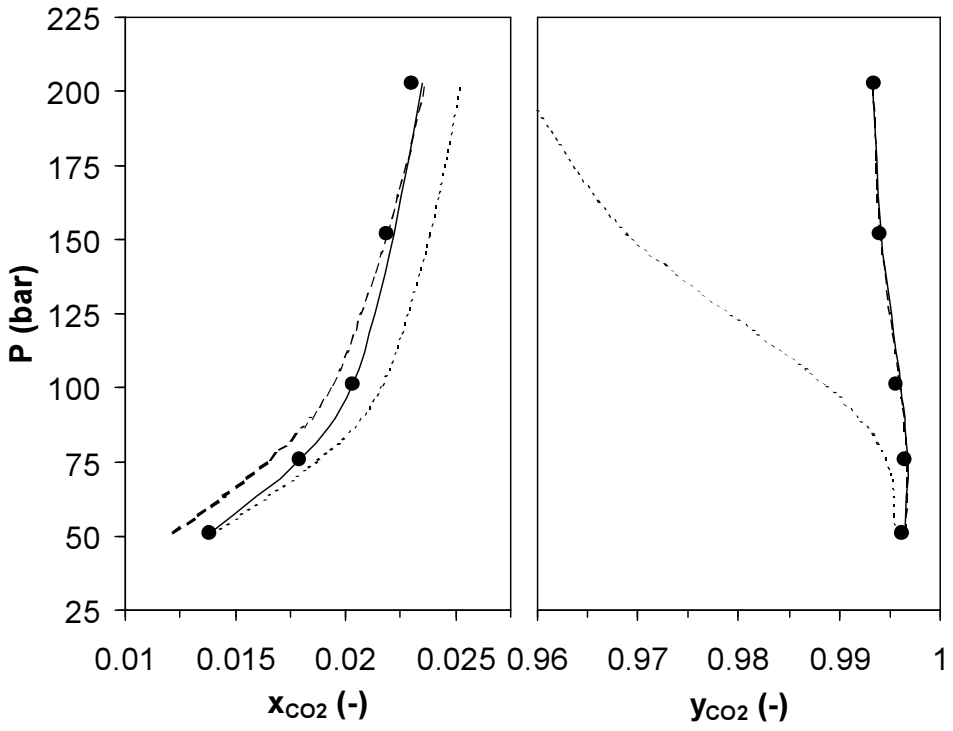

Figure 6.4 Correlation of carbon dioxide-water equilibrium data at 323 K (•) using the Peng-Robinson eos with the Quadratic (···), Stryjek-Vera (---) and the Panagiotopoulos-Reid (—) mixing rules.

6.2.3 Results and discussion

Methyl methacrylate shows a very limited solubility in water. As a result, the ternary systems encountered during the residual monomer extractions consist for over 99% of carbon dioxide and water. Additionally, for the carbon dioxide-water subsystem a relatively large amount of experimental data is available, in contrast to the other subsystems. Therefore, the CO_2-H_2O subsystem is regarded as the determining factor in the evaluation of the mixing rules. A typical correlation of the phase behavior obtained from the various mixing rules with optimized interaction parameters is shown in Figure 6.4 for the system carbon dioxide-water at 323 K[11-13].

A good correlation is obtained using the Panagiotopoulos-Reid (PR) mixing rule, which accurately describes both the water and the gas phase. The Stryjek-Vera (SV) mixing rule also allows for a description of asymmetrical phase behavior, however, less effective than PR, as larger deviations for the aqueous phase are observed. The Quadratic mixing rule, due to its symmetry, show the largest deviations, in both the aqueous and the gaseous phases. The results for the Melhem (M) and the Mathias-Klotz-Prausnitz (MKP) mixing rules are omitted, as these become identical to the PR mixing rule when applied to binary systems.

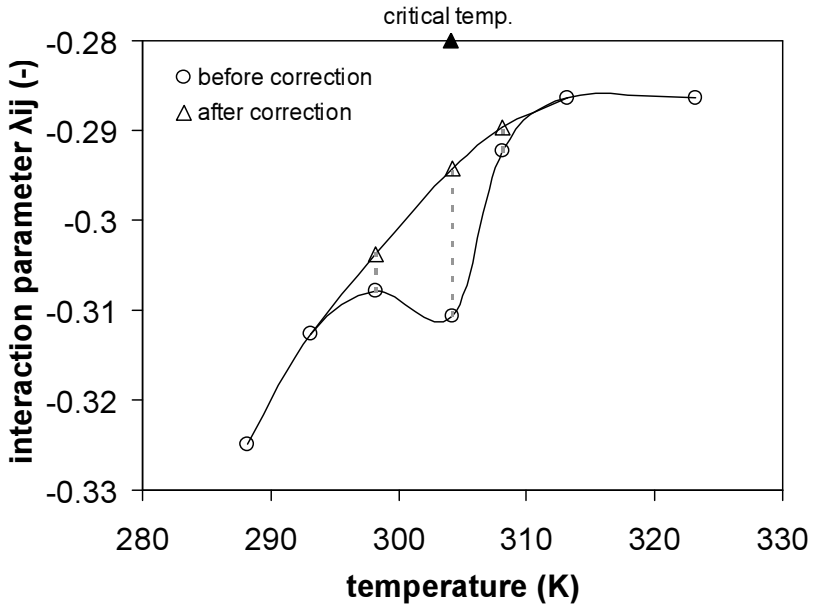

Figure 6.5 Corrections of the binary interaction parameter λ_{ij} for the system CO_2-H_2O.

Table 6.2 Optimized interaction parameters for the Peng-Robinson eos and the PR and SV mixing rules for the systems carbon dioxide-water and carbon dioxide-MMA.

		Panagiotopoulos-Reid			Stryjek-Vera		
T (K)	# points	k_{ij}	λ_{ij}	$\Delta x+\Delta y$ (%)	k_{ij}	λ_{ij}	$\Delta x+\Delta y$ (%)
CO_2-H_2O							
288	5	-0.147	-0.325	0.5	-0.116	-0.292	0.8
293	6	-0.139	-0.313	0.6	-0.111	-0.280	0.8
298	6	-0.134	-0.304	2.1	-0.107	-0.276	2.7
304	6	-0.126	-0.294	3.2	-0.101	-0.278	4.3
308	3	-0.120	-0.290	1.0	-0.097	-0.264	1.1
313	3	-0.113	-0.286	0.9	-0.093	-0.260	1.0
323	6	-0.103	-0.286	1.7	-0.083	-0.254	2.8
CO_2-MMA							
313	7	-0.284	-0.218	6.0	-0.277	-0.277	5.1
353	6	-0.146	-0.034	0.9	-0.159	-0.045	0.9
379	5	-0.046	0.056	1.9	-0.072	0.035	2.8
H_2O-MMA							
293	1	-0.051	0.253	-	-0.074	0.235	-
303	1	-0.040	0.254	-	-0.067	0.231	-
313	1	-0.029	0.255	-	-0.061	0.228	-
323	1	-0.017	0.258	-	-0.055	0.225	-
333	1	-0.005	0.261	-	-0.048	0.223	-

In Table 6.2, the optimized interaction parameters for the PR and SV mixing rules are shown for various temperatures. In the entire temperature range, a more accurate description of the phase behavior is obtained using the PR mixing rule, therefore the PR mixing rule and the MKP mixing rule using the PR binary values are chosen for further calculations. It should be noted that near the critical temperature of carbon dioxide an increased error in the correlation of the data is observed. The interaction parameters obtained in this region, particularly λ_{ij}, show a large deviation from trends observed at other temperatures. Therefore, the λ_{ij} values have been slightly adjusted to conform to the values at the other temperatures, as shown in Figure 6.5.

In addition to the CO_2-H_2O system, interaction parameters have been obtained for the systems CO_2-MMA and H_2O-MMA. For both these subsystems, very little

data is available. For the carbon dioxide-MMA system, interaction parameters have been obtained from bubble point measurements at temperatures in the range 313-379 K and pressures between 11 bar and 101 bar[14]. As dew points are absent from the data set, the interaction parameters have been optimized on the liquid branch of the phase envelope only. Furthermore, the bubble points near the mixture's critical point have been omitted to improve the correlation remaining points.

The only data available in literature for the MMA-water system consists of mutual solubility data at standard pressure for various temperatures[15]. Therefore, the interaction parameters are fit to isobaric data in the temperature range 273-353 K. At each temperature the two interaction parameters are optimized to the two equilibrium phases, resulting in an exact description.

Table 6.3 Binary interaction parameters for the Peng-Robinson eos and the PR and MKP mixing rules for calculation of the ternary system.

	H_2O-CO_2		H_2O-MMA		MMA-CO_2	
T (K)	k_{ij}	λ_{ij}	k_{ij}	λ_{ij}	k_{ij}	λ_{ij}
Panagiotopoulos-Reid						
298	0.170	0.304	-0.046	0.254	-0.056	0.280
313	0.173	0.286	-0.029	0.255	-0.067	0.217
323	0.184	0.286	-0.017	0.258	-0.074	0.175
333	0.201	0.286	-0.005	0.261	-0.082	0.133
Mathias-Klotz-Prausnitz						
298	0.018	0.304	-0.173	0.254	-0.196	0.280
313	0.030	0.286	-0.157	0.255	-0.176	0.217
323	0.041	0.286	-0.146	0.258	-0.162	0.175
333	0.058	0.286	-0.135	0.261	-0.149	0.133

For the description of the partitioning behavior in the ternary system, the temperature dependent interaction parameters obtained from the binary subsystems have been interpolated and, by necessity, extrapolated, knowing that extrapolation increases uncertainty in the predictions of the ternary system. Table 6.3 shows the interaction parameters for the Panagiotopoulos-Reid and the Mathias-Klotz-Prausnitz mixing rules, as used for the prediction of the ternary phase behavior.

The partition coefficients of MMA over water and carbon dioxide as predicted by the Peng-Robinson eos using PR and MKP mixing rule are shown in Figure 6.6. The solvent strength of carbon dioxide and thus the partitioning behavior of MMA is strongly dependent on the density of the carbon dioxide rich phase. This translates in Figure 6.6 to a strong temperature dependence of the partition coefficients, with lower values at higher temperatures. In the subcritical system at 298 K, a phase transition is present at approximately 63 bar, visible as an abrupt increase in *k*-value due to the increased density of the liquefied carbon dioxide phase.

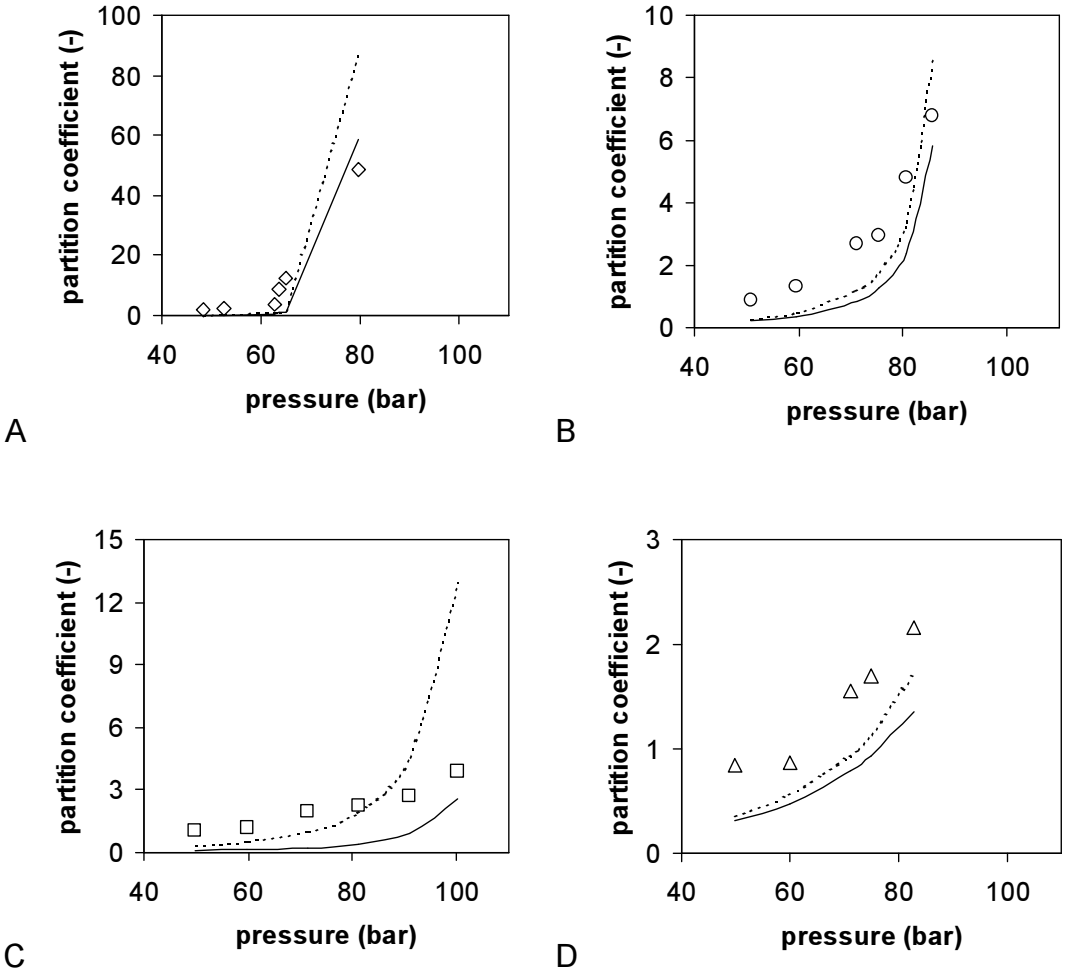

Figure 6.6 Partition coefficients of MMA over water and carbon dioxide, experimental data and Peng-Robinson model predictions. A) 298 K; B) 313 K; C) 323 K; D) 333 K; Peng-Robinson model predictions using PR (—) and MKP mixing rules (---).

Model predictions with the Peng-Robinson eos, using either the PR or the MKP mixing rule, result in a qualitative description of the partitioning behavior of MMA over water and carbon dioxide. Quantitatively, the calculated *k*-values are underestimated at low pressures, whereas at high pressures and temperatures below 333 K, the values are overestimated with the MKP mixing rule. In all calculations, the use of the MKP mixing rule results in higher partition coefficients than the *k*-values obtained with the PR mixing rule. Although the PR mixing rule is suffering from the dilution problem and the Michelsen-Kistenmacher syndrome, the calculated partition coefficients are close to the values obtained with the MKP mixing rule; except for the calculations at 323 K, where much higher values are obtained with the MKP mixing rule.

6.2.4 Conclusions

The partitioning behavior of MMA over water and pressurized carbon dioxide has been modeled with the Peng-Robinson equation of state using the Panagiotopoulos-Reid and Mathias-Klotz-Prausnitz mixing rules. The model qualitatively predicts the phase behavior of the ternary system. In general, regarding the binary systems, more experimental data is required for a better optimization of the interaction parameters.

6.3 Phase equilibria calculations with the Sanchez-Lacombe eos using fugacities

6.3.1 Consistent phase equilibria calculations

The Sanchez-Lacombe (SL) eos[18-20] is a common lattice-fluid equation-of-state, which is able to describe the thermodynamic properties of molecular fluids of arbitrary size, and is mainly used to describe polymer-solvent phase behavior. The basis of the lattice fluid model is the estimation of thermodynamic properties from the partition function. The Helmholtz energy A, the chemical potentials μ_i and the equation-of-state P may be derived from the canonical partition function $Q(T,V,n)$ by

$$A(T,V,n) = -RT\ln Q \tag{6.7}$$

$$\mu_i(T,P,n) = -RT\left(\frac{\partial \ln Q}{\partial n_i}\right)_{T,V,n_j} \tag{6.8}$$

$$P = RT\left(\frac{\partial \ln Q}{\partial V}\right)_{T,n} \tag{6.9}$$

However, Sanchez and Lacombe used the more convenient configurational partition function $Z(T,V,n)$

$$Z(T,V,n) = \Omega_c \exp\left(-\frac{E}{RT}\right) = \frac{Q(T,V,n)}{\lambda(T,n)} \tag{6.10}$$

where Ω_c is the number of configurations, E is the lattice energy and $\lambda(T,n)$ corresponds to the internal and kinetic parts of the canonical partition function. As long as $\lambda(T,n)$ is independent of the mixture composition, the configurational chemical potentials μ_i^{conf} can be used for phase equilibria calculations. However, recent work by Neau[21] reveals that the λ term present in the chemical potentials proposed by Sanchez and Lacombe *is* dependent on mixture compositions. The dependence of the λ term on the mixture composition is shown by the fact that μ_i^{conf} does not satisfy the fundamental thermodynamic expressions of the chemical potential in the ideal gas state. Consequently, the chemical potentials cannot be used for thermodynamically consistent phase equilibria calculations. To overcome this problem, Neau[21] proposes consistent fugacity coefficients ϕ_i derived from the equation-of-state $P(T,V,n)$ by

$$\ln \phi_i = -\ln z + \left(\frac{\partial A^{res}(T,V,n)}{\partial n_i}\right)_{T,V,n_j} \tag{6.11}$$

where z is the compressibility factor and A^{res} is the residual Helmholtz energy

$$A^{res}(T,V,n) = A(T,V,n) - A^{ideal}(T,V,n) = -\int_{\infty}^{V}\left(P - n\frac{RT}{V}\right)\frac{dV}{V} \tag{6.12}$$

6.3.2 Ethylene-PEP cloud-point calculations

In Chapter 2, the description of the antisolvent effect of carbon dioxide on the system ethylene-PEP with the SL eos and the SAFT eos was compared. As shown above, phase equilibria with the SL model using chemical potentials are not thermodynamically consistent. Therefore, the cloud-point behavior of the system ethylene-PEP at 312.6 K was re-evaluated using the SL model calculations based on fugacities. It should be noted that in these calculations the original SL-theory was used, in contrast to the adapted form[22] presented in section 2.2.1. The main

difference between the two versions is the relaxation of the classical assumption that the closest mer-mer distance is related to the lattice hole volume.

The resulting cloud-point curve, along with the curves calculated in Chapter 2, is shown in Figure 6.7. Similar to the previous SL curve, a maximum cloud-point pressure is observed. However, the maximum has shifted from approximately 5 wt% to approximately 10 wt% polymer. The chemical potential-based SL calculations give a fair description of the cloud-point behavior. The fugacity-based SL calculations, however, result in a poor description of the cloud-points, with a much wider miscibility gap. For the system *n*-decane–carbon dioxide Neau reports a decrease in mean deviations for the description of VLE from 44 % to 9 % by using fugacities[21]. The less accurate description of the ethylene-PEP cloud-points with the original SL theory using fugacities compared to the adapted form of the SL theory using chemical potentials may result from the improvements obtained from the adaptation of the SL theory. This is illustrated in Figure 6.8 for the predictive description ($\delta_{12} = 0$) of the system *n*-pentane-carbon dioxide at 408 K.

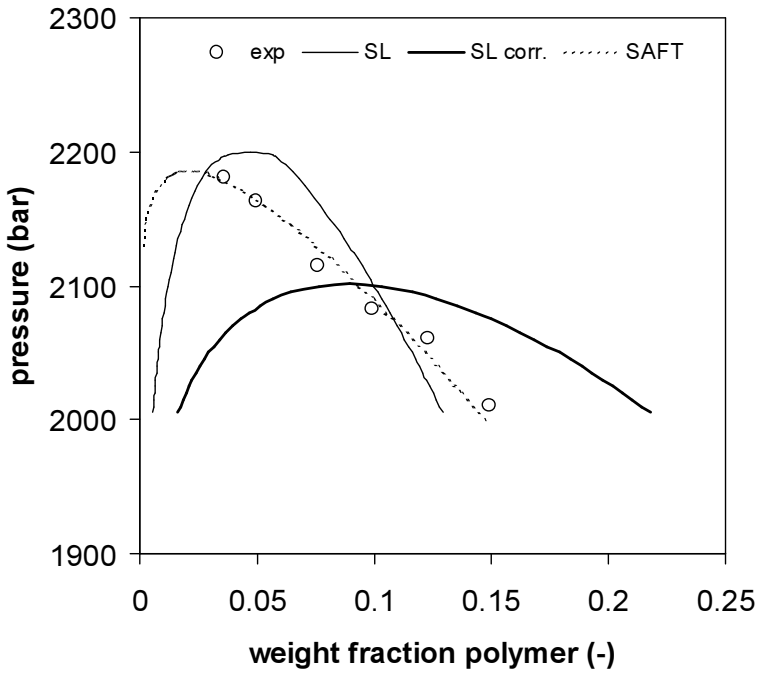

Figure 6.7 Correlation of the cloud-point curve for the system ethylene-PEP at 312.6K with the adapted SL eos described in Chapter 2 using chemical potentials (SL) and with the fugacity based original SL eos (SL corr.) as well as with the SAFT eos.

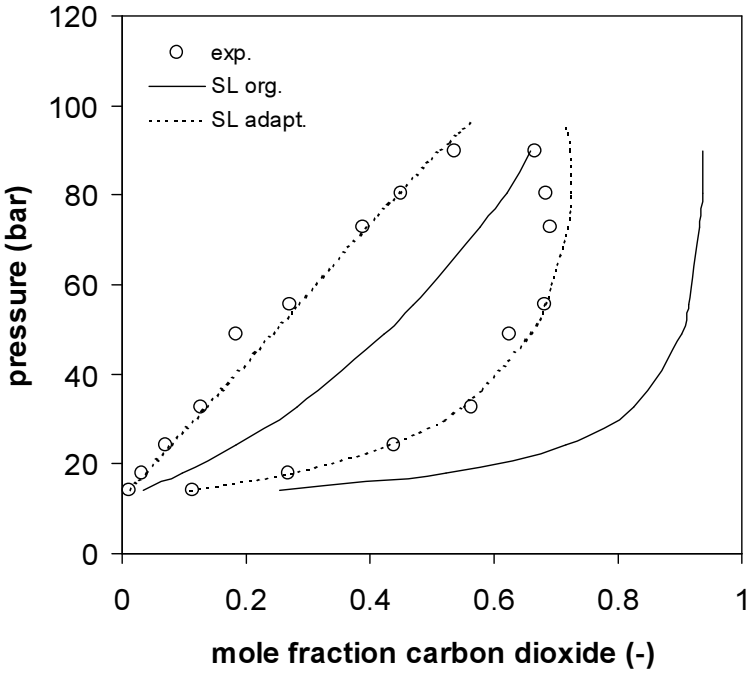

Figure 6.8 Predictions (δ_{12} = 0) for the n-pentane-carbon dioxide VLE at 408 K with the Sanchez-Lacombe eos in the original form[18-20] and the adapted form[22].

Based on the new calculations, the description of the antisolvent effects of carbon dioxide in the ethylene-PEP system using the fugacity-based method are expected to be similar or less accurate than the results described in Chapter 2. The previous conclusion that the SAFT model is more suitable for the description of the ethylene-PEP-carbon dioxide system is likely not affected by the fugacity-based SL calculations.

6.4 Modeling of supercritical mixtures using excess enthalpy data

In Chapter 2 the cloud-point behavior of the ternary system carbon dioxide-ethylene-poly(ethylene-*co*-propylene) has been modeled using the SAFT equation of state. For the modeling of such multi-component fluid mixtures, the system is divided into binary subsystems. For each binary subsystem an interaction parameter is obtained by optimization to appropriate experimental thermodynamic data of the concerning subsystem. The binary interaction parameters for subsystems containing polymer are obtained from cloud-point data. The interaction parameter of the subsystem without polymer, carbon dioxide-ethylene in the case of Chapter 2, is generally obtained from a fit to vapor-liquid equilibria data. Subsequently, the ternary system containing polymer, monomer and carbon dioxide can be described based on the binary interaction

parameters as obtained from the subsystems. In general, these interaction parameters appear to be temperature dependent, as shown in Figure 2.9. Consequently, in order to obtain interaction parameters for supercritical mixtures (i.e. for mixtures in the single fluid region), the temperature relation obtained from the VLE data has to be extrapolated to the desired temperature. For that reason, it would be preferable to obtain the interaction parameters from measurements at the temperature of application.

One of the few thermodynamic properties accessible above the mixture critical point is the excess molar enthalpy. To test the suitability of the excess enthalpy for the determination of interaction parameters used in the SAFT equation of state, the description of both the VLE behavior and the excess molar enthalpies for the system ethylene-ethane have been studied. This system is chosen because of the monomer functionality of ethylene and for of the availability of excess enthalpy data.

6.4.1 Excess molar enthalpy

As shown in Chapter 2, the SAFT equation of state yields an expression for the residual Helmholtz energy $a^R = f(T,\rho,x)$, from which the compressibility is calculated by

$$Z = 1 + \rho\left(\frac{\partial a^R / RT}{\partial \rho}\right)_{T,x} \tag{6.13}$$

where ρ is the molar density. The residual molar enthalpy is obtained from the Helmholtz energy by

$$h^R = a^R - T\left(\frac{\partial a^R}{\partial T}\right)_{\rho,x} + RT(Z - 1 - \ln Z) \tag{6.14}$$

The residual enthalpy is defined as the deviation from the ideal gas enthalpy at given temperature and pressure. However, in experimental mixing enthalpy measurements the excess enthalpy is obtained, which is defined as the deviation from the ideal solution. The excess enthalpy is related the residual enthalpy by

$$h^E = h^R - \sum_i x_i h_i^R \tag{6.15}$$

where x_i and h_i^R denote the molar fraction of component *i* in the mixture and the residual molar enthalpy of the pure component *i* at given temperature and pressure, respectively.

6.4.2 Experimental VLE and excess enthalpy data

All experimental data were obtained from literature. The reported vapor-liquid phase equilibria data were measured using a vapor recirculation equilibrium cell, which circulates the vapor through a stationary liquid[23]. After reaching equilibrium, the temperature and pressure were measured. Additionally, the vapor and liquid compositions were obtained by gas chromatography. Using this technique, measurements were performed on the system ethylene-ethane at 263 K and 293 K, respectively.

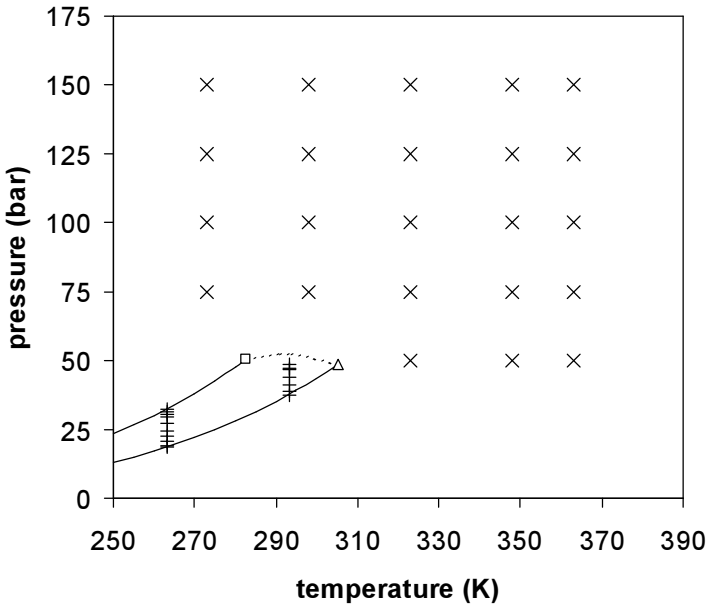

Figure 6.9 Phase diagram of the system ethylene-ethane with the critical points of ethylene (∆) and ethane (□), respectively; the critical locus (···); the conditions of VLE measurements[23] (+) and excess molar enthalpy measurements[24] (×).

The excess molar enthalpy data were obtained using a high-temperature high-pressure calorimeter[24]. Measurements were performed at liquid and supercritical conditions in the ranges 273-363 K and 50-150 bar at regular intervals, as shown in Figure 6.9. In addition, Gruszkiewicz et al.[24] have reported the coefficients of the Redlich-Kister-equation-fit[25] to the experimental data. The Redlich-Kister equation

is a flexible function commonly used for correlating and reduction of binary excess enthalpy data. It is an empirical power expansion of the following form

$$H_m^E = x_1 x_2 \sum_i a_i (x_1 - x_2)^i \tag{6.16}$$

where H_m^E is expressed in J/mol, a_i are adjustable coefficients and x_1 and x_2 are the mole fractions ethylene and ethane, respectively. For practical reasons the values of the Redlich-Kister correlation were used instead of the experimental data. Deviations of the Redlich-Kister values from the experimental data are generally within 1.5% of the maximum value for each pressure range.

6.4.3 SAFT modeling

For the description of the excess molar enthalpy using the SAFT equation-of-state, the program used in Chapter 2 for the phase equilibria calculations was extended with equations (6.14) and (6.15). SAFT binary interaction parameters were obtained by a fit of the excess enthalpy data at nine different concentrations in the range $x_{ethylene}$ = 0.1–0.9. The following objective function (AARD) was used to obtain the interaction parameters

$$OF = \frac{1}{N_P + N_x} \sum_j^{N_P} \sum_i^{N_x} \left| \frac{H_{RK,i}^E - H_{SAFT,i}^E}{H_{RK,i}^E} \right|_j \tag{6.17}$$

For each temperature, the interaction parameters were determined for the individual pressures as well as for the whole pressure range.

Table 6.4 Absolute average relative deviations (AARD, eq. 6.17) in SAFT excess enthalpy descriptions.

	AARD (%)				
P (bar)	273 K	298 K	323 K	348 K	363 K
50	–	–	5.0	10.6	5.1
75	25.6	41.9	328.2	8.2	3.2
100	14.8	53.5	61.2	112.7	35.1
125	9.8	18.0	23.1	64.4	64.2
150	5.5	11.5	14.4	17.6	37.0
50–150	33.1	115.0	331.1	229.8	156.3

The accuracy of the description of the excess molar enthalpies using the SAFT eos is highly dependent on the extend and shape of the excess curves. The deviation in the excess enthalpy at the various temperatures and pressures is shown in Table 6.4. In general, the SAFT eos describes the trends of the excess curves for the various pressures well. However, in the pressure range 75–150 bar, depending on the temperature, highly asymmetric excess curves or particularly large excess values are observed, which lead to large deviations of the SAFT description. This

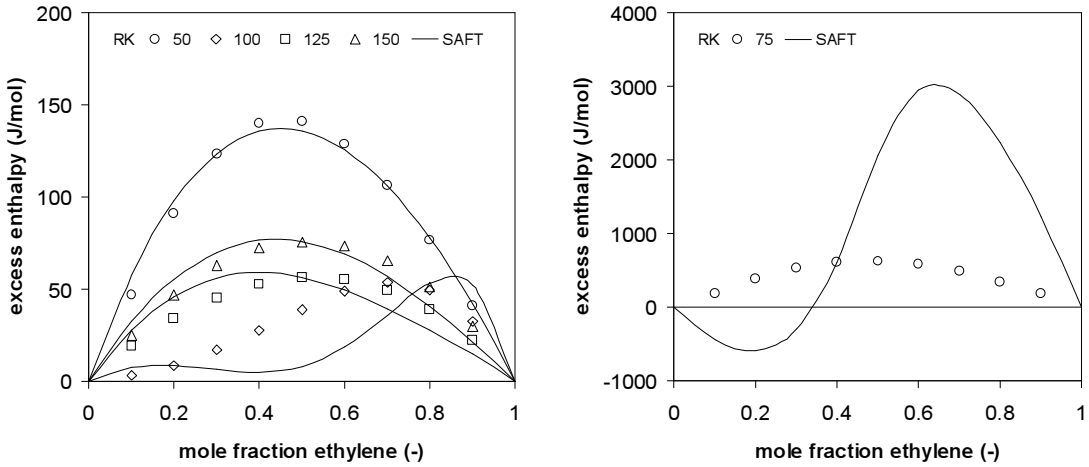

Figure 6.10 Excess molar enthalpy data fit at 323 K to individual pressures with the Redlich-Kister (RK) equation and the SAFT equation of state.

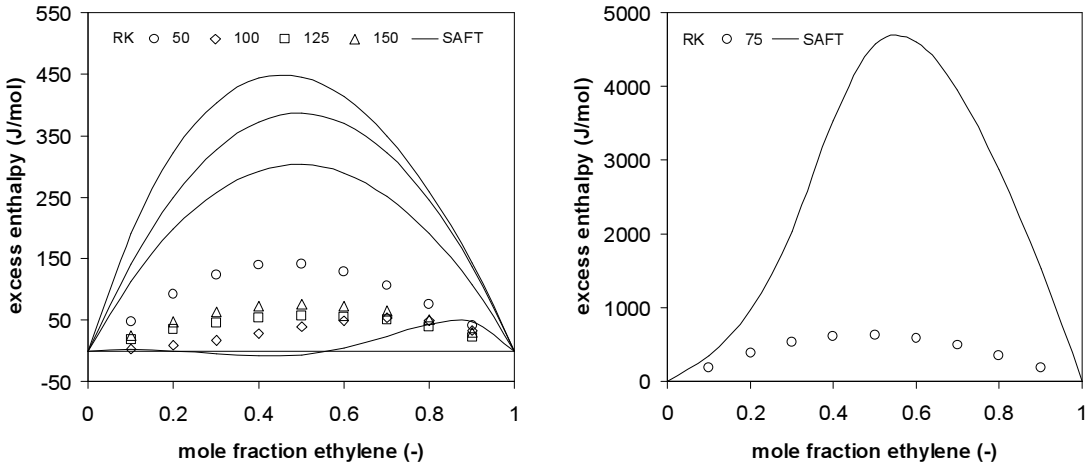

Figure 6.11 Excess molar enthalpy data fit at 323 K to the pressure range 50–150 bar with the Redlich-Kister (RK) equation and the SAFT equation of state.

is illustrated in Figure 6.10 for the excess enthalpy curves at 323 K. Consequently, the interaction parameters obtained at individual pressures show a large variation, particularly for temperatures above 300 K. Using a single interaction parameter per temperature for correlations of the whole pressure ranges results in much larger deviations in the excess enthalpies, as shown in Figure 6.11 for 323 K. However, the interaction parameters show more correlated behavior, as shown in Figure 6.12.

Figure 6.12b shows that the values of the interaction parameters are lower than the values obtained from VLE data at 263 K and 293 K. At the lower temperatures, both sets of parameters show a similar positive correlation with the temperature. At higher temperatures, a negative correlation with temperature is observed for the parameters obtained from the excess data. The binary interaction parameters obtained from the excess molar enthalpies at 323 K and lower can be described by a linear temperature relation. Using this linear temperature relation of the interaction parameters, the VLE data at 263 K and 293 K were modeled. In

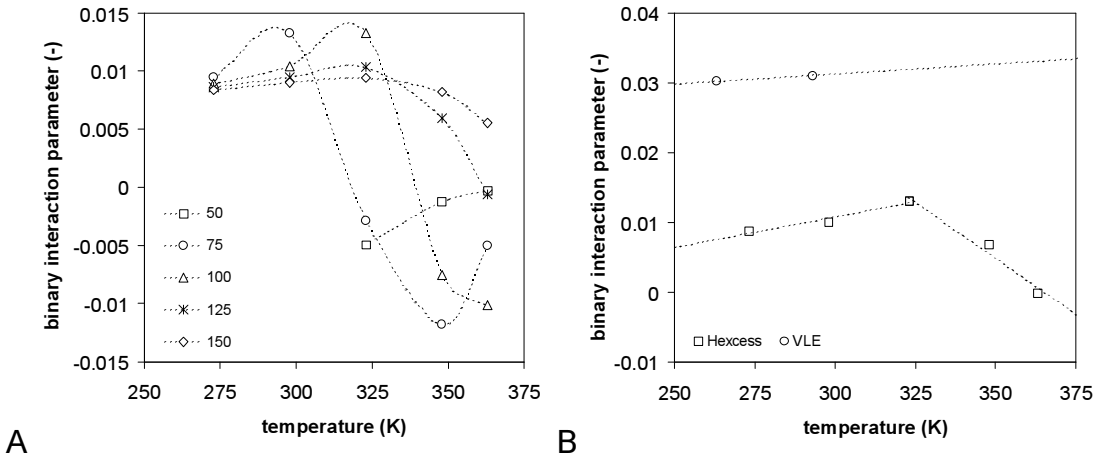

Figure 6.12 A) Binary interaction parameters obtained from excess molar enthalpy data; B) comparison with interaction parameters obtained from VLE data.

Figure 6.13, the resulting phase behavior is compared to the description of the phase behavior using interaction parameters fitted to the VLE data. Both sets of interaction parameters describe the phase behavior well. However, a somewhat better description is obtained with the parameter fit to the VLE data.

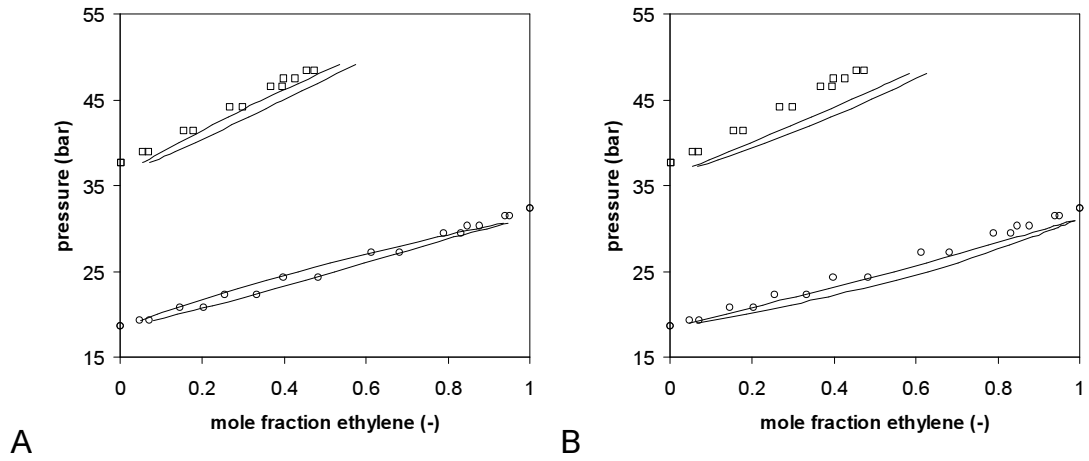

Figure 6.13 SAFT correlation of phase behavior at 263 K (o) and 293 K (□) with binary interaction parameters obtained from A) VLE data; B) excess molar enthalpy data.

6.4.4 Conclusions

The excess molar enthalpy data of the system ethylene-ethane in the critical region has been modeled using the SAFT equation of state. The model correctly predicts the trends in the excess curves. However, large deviations are observed for curves with particularly large excess enthalpy values as well as for highly asymmetric excess curves. The interaction parameters obtained from the excess data are suitable for description of the phase behavior and allow for description of other thermodynamic properties in the supercritical region. However, as the interaction parameters at higher temperatures deviate from the linear correlation at lower temperatures, extrapolation remains as doubtful as extrapolation of VLE fit parameters. Because of the close molecular resemblance, the system ethylene-ethane has a rather "ideal" behavior, as indicated by interaction parameters close to zero. A comparison using a system of two molecularly more different components may provide a more conclusive insight in the predictive value of excess data for the description of supercritical mixtures.

6.5 Polymer polydispersity issues in phase equilibria

The phase behavior of polymer solutions plays an important role in the synthesis and processing of polymers. Many polymers are produced in solution, which requires that the polymer is dissolved during the polymerization process. Therefore, extensive work has been done to measure the cloud-points, i.e. the onset of liquid-liquid immiscibility, for many polymeric systems.

Due to the nature of the polymerization process, polymers are usually polydisperse. Consequently, a wide range of chain lengths is present in a polymer, as characterized by the various averaged molecular weights: M_n, M_w and M_z. The polydispersity significantly complicates the modeling of the cloud-points of these systems. In the case of a binary mixture containing a monodisperse polymer and a solvent, there is no thermodynamic ambiguity. A cloud-point in a binary mixture corresponds with the coexistence point, on the basis of the Gibbs phase rule. In the case of polydisperse polymers, the mixture contains more than two components and the coexistence points do not coincide with the cloud-points. Furthermore, the discrepancy increases with increasing polydispersity.

A common first approximation in the modeling of cloud-points with an equation-of-state is to assume monodispersity of the polymer. This assumption has also been applied in Chapter 2. However, for an accurate description of cloud-point curve, the polydispersity should be accounted for in the calculations. This can be accomplished by using a number of polymer pseudo-components representing the polymer weight distribution[26,27].

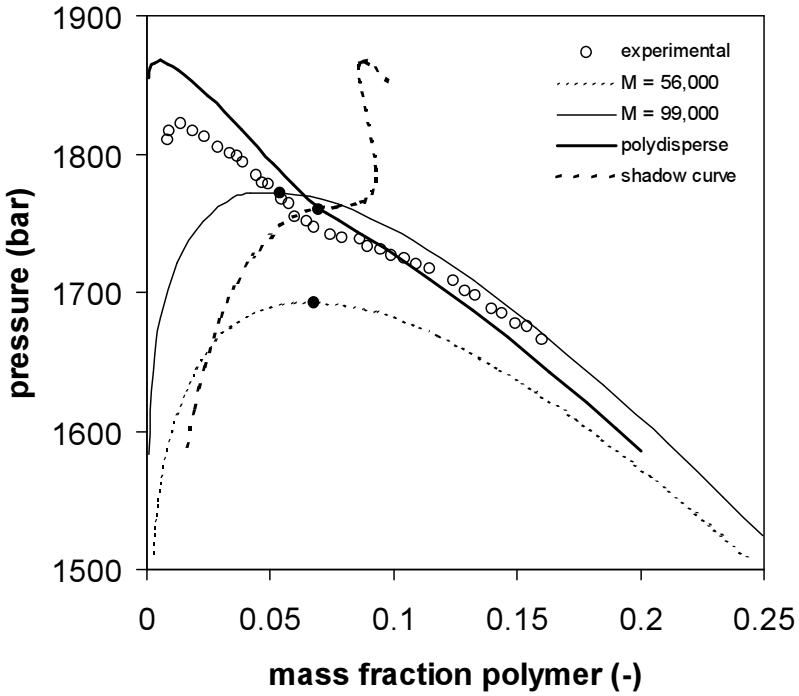

Figure 6.14 Cloud-point curve PE-ethylene at 423 K[28]. SAFT eos correlations[27] assuming monodispersity with molecular weights M = 56,000 g/mol and 99,000 g/mol as well as approximation of polydispersity by 36 pseudo-components describing the polymer weight distribution (interaction parameters: $k_{polymer\text{-}solvent} = 0.0392$, $k_{polymer\text{-}polymer} = 0.0$).

This technique has been applied by Jog et al.[27] to the cloud-points of polyethylene (M_n = 56,000 g/mol, M_w = 99,000 g/mol) in ethylene at 423 K using the SAFT equation-of-state, as shown in Figure 6.14. The experimental cloud-points in this system, show a maximum pressure of 1821 bar at 1.4 wt% PE, whereas the critical point occurs at approximately 1755 bar and 6.0 wt% PE, which is indicated by a rather sharp bend in the curve. In the case of a SAFT description of the cloud-point curve assuming monodispersity of the polymer, the critical point coincides with the highest cloud-point. Consequently, large deviations from the experimental cloud-points are observed at concentrations below the critical point. At concentrations above the critical point, the cloud-points are well described by the monodisperse calculations, when the weight averaged molecular weight of the polymer is used. In the case of SAFT calculations with 36 pseudo-components approximating the polymer weight distribution, a much closer agreement with the experimental data is obtained. This is especially the case at polymer concentrations below the critical point, which occurs at the intersection of the cloud-point curve with the shadow-point curve. The shadow-point curve shows the overall polymer concentration in the second phase formed at the cloud-point (conjugate phase), which has a molecular weight distribution different from the principal phase. At polymer concentrations above the critical point, the differences between de calculations become increasingly less significant. Ultimately, in the sorption and swelling regime, at pressures below 300 bar, the influence of the molecular weight is negligible. Figure 6.15.a shows the sorption and swelling

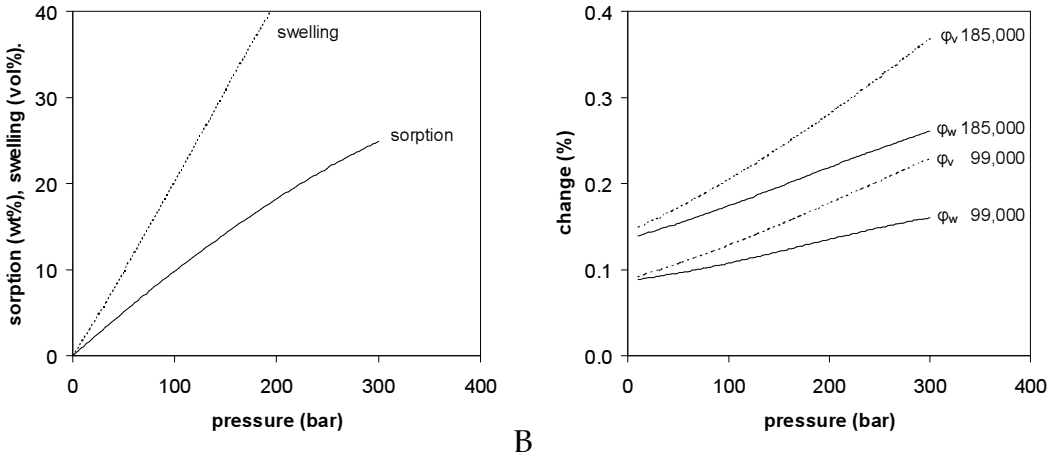

Figure 6.15 A) SAFT modeling of the sorption and swelling of PE in ethylene at 423 K with M = 56,000 g/mol; B) changes to the sorption and swelling fractions when applying M = 99,000 and 185,000 g/mol; —sorption, - - - swelling.

curves of PE in ethylene as predicted by the SAFT eos using a monodispere molecular weight of M = 56,000 g/mol. The relative changes to the sorption and swelling curves when molecular weights of M = 99,000 g/mol and M = 185,000 g/mol are used, are shown in Figure 6.15b. For pressures up to 300 bar, the relative differences are well below 0.5 %, however, the increase of the differences with increasing pressure will ultimately lead to the previous observations for the cloud-points.

6.6 Molecular dynamics, the future?

In the previous chapters, several situations have been encountered where experiments and conventional continuum models reach their limits, e.g. extremely high pressures in cloud-point measurements and experimental uncertainty in sorption and swelling experiments. Issues in the thermodynamic modeling of polymer-solvent systems include uncertainty in polymer pure component eos parameters and increased complexity resulting from polydispersity of the polymer. In these cases molecular dynamics simulations might provide some answers.

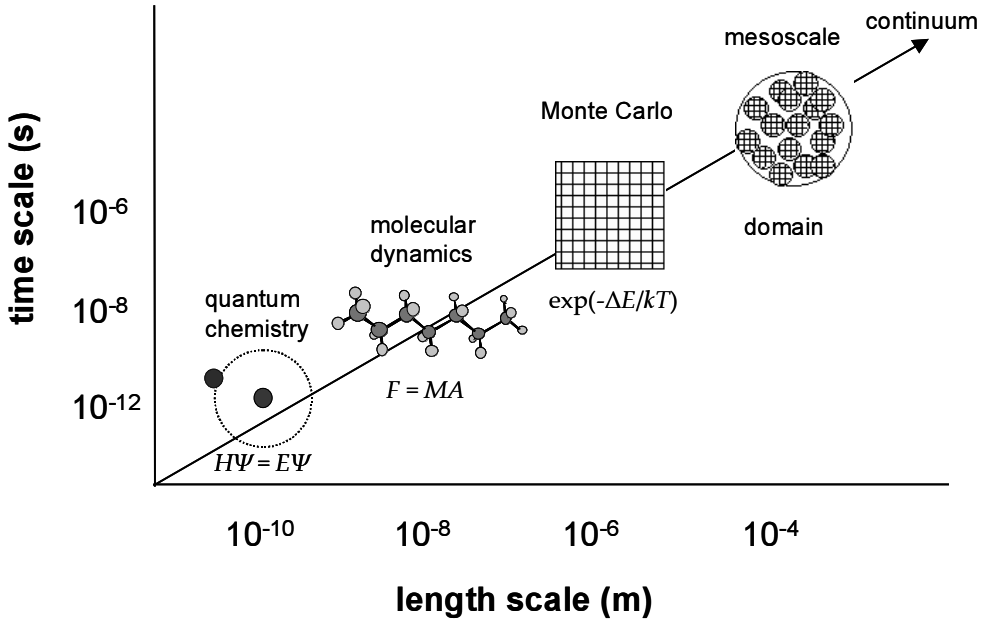

Figure 6.16 Time scales and length scales in simulations[31].

Molecular dynamics (MD) simulations are numerical simulations to classical Newtonian equations of motion for a set of particles interacting with the help of interatomic potentials. Provided that the interatomic potentials for a given system are sufficiently accurate, MD simulations allow for the prediction of the properties

of novel materials which have not yet been synthesized. Moreover, MD simulations can predict difficult-to-measure properties of existing materials as well as validate continuum models. Furthermore, MD provides a picture on the molecular level of both the structure and the dynamics of the system, which allows for elucidation of mechanisms. For example, MD has revealed the mechanism of the diffusion of gas through polymers as a sequence of activated jumps between neighboring locations ("hopping diffusion")[29,30].

However, this same atomic detail also severely limits the time scales and length scales that can be simulated. Currently, the obtainable simulation time and length scales are in the order of nanoseconds and nanometers, respectively. In Figure 6.16, the time and length scales of various simulation techniques are shown.

One of the areas where MD has been applied is in the field of sorption and diffusion of various gases in rubbery and glassy polymer membranes[32]. In these systems, MD allowed for a determination of both the sorption and the swelling of the polymer as a function of gas pressure from desorption isotherms, as shown in Figure 6.17. Additionally, in these isotherms, the sorption-induced glass-transition

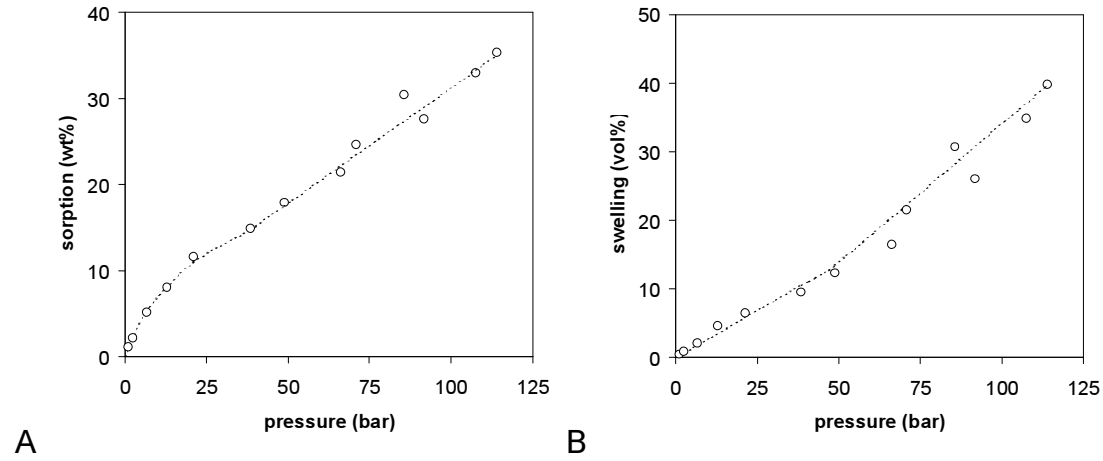

Figure 6.17 Sorption and swelling isotherms of CO_2 in PE (n=60) at 350 K, derived from data of Van der Vegt et al.[33]

can be observed. In the glassy polymer, a convex sorption profile is obtained, whereas in the rubbery state a linear relation is obtained.

An example of MD extending the range of measurement is given by the work of Lyulin and Michels[34], who have simulated the behavior of atactic polystyrene in the vicinity if the glass transition temperature. The glass transitions were obtained

from the specific volume of the polymer, as shown in Figure 6.18a. Using MD, the range of measurement is extended well above 10,000 bar.

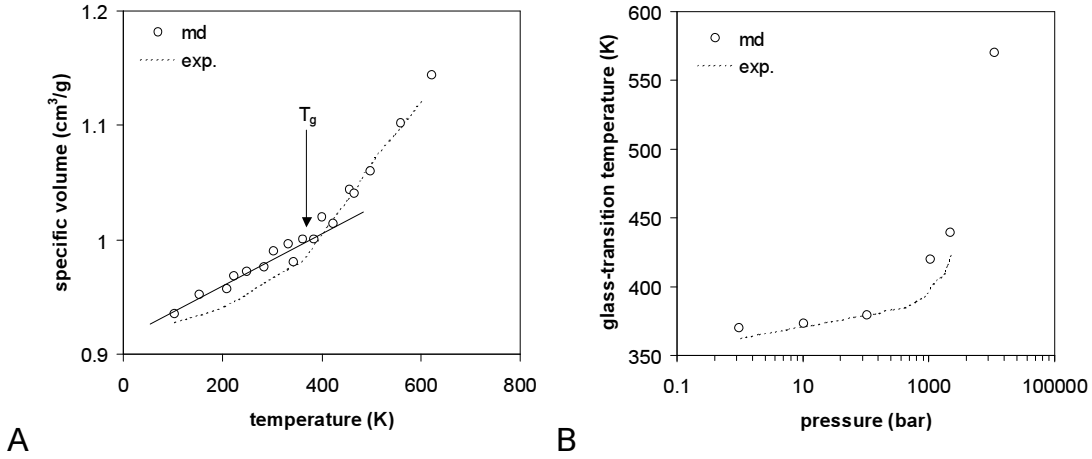

Figure 6.18 Glass-transition temperature of atactic polystyrene (n=80)[34]; A) specific volume as a function of temperature at 1 bar; B) pressure dependence of T_g. Dashed lines represent experimental data for atactic polystyrene of M ~ 9000 g/mol (n≈86).

For many applications, thermodynamic models such as the Sanchez-Lacombe equation-of-state and the Statistical Associating Fluid Theory (SAFT) provide an adequate description of polymer-solution systems. Before these models can be used, pure component parameters of each substance are required. In de case of volatile components, these can be obtained from vapor-liquid equilibria (VLE) data. However, in absence of a vapor-liquid transition, another method is required for polymers and other high molecular weight components. In such cases, the pure component parameters are commonly obtained from a fit to volumetric (*PVT*) data. Unfortunately, the *PVT* behavior of polymers is less sensitive to the pure component parameters than the VLE behavior of volatile components, resulting in an uncertainty in the obtained values. MD might provide an alternative method for obtaining pure component parameters if chemical potentials can be obtained from the simulations. For small gaseous penetrants, this can be achieved using a random particle insertion method[32]. However, larger penetrants, such as a molecule of the polymer itself, induce large rearrangements in the polymer, which renders this method unsuitable. Possibly, the chemical potential of the polymer might be obtained from the difference in free energy from MD boxes of identical temperature and volumes with n and n+1 equilibrated polymer molecules, assuming n is sufficiently large. Currently, such large-scale calculations with

polydisperse polymer molecules, realistic chain lengths and calculational time scales beyond the polymer relaxation time scales are unachievable with the present computer technology. However, considering Moore's law and advances in high-performance computing, e.g. hyper-threading and clustering, computational speeds are expected to reach the petaflop region somewhere between 2007 and 2010 (1 petaflop is 10^{15} floating point operations per second, approximately 100 times the current maximum speed of 10 teraflop). When mainstream petaflop computing is achieved, large-scale realistic molecular dynamics calculations on polymer system will become possible.

6.7 Concluding remarks

In this thesis, some aspects of polymer processing using supercritical fluids, particularly supercritical carbon dioxide ($scCO_2$), have been discussed. Key issue in the application of $scCO_2$ for polymer processing is the phase behavior of the polymer-SCF systems, for which two regimes are important; the cloud-point regime where low concentrations of polymer are dissolved in the SCF and the sorption and swelling regime, where the SCF is dissolved in the polymer phase. The phase behavior in the high-pressure cloud-point region is of relevance to supercritical polymerizations and chemical modifications. Addition of CO_2 to these polymer-monomer/reactant systems may lead to even higher cloud-point pressures. Equation-of-state models have been successfully applied to describe the antisolvent effects caused by carbon dioxide in these systems.

The sorption and swelling regime, occurring at much lower pressures, is encountered in applications ranging from shaping and blending to extractions and impregnations. To simultaneously measure both the sorption and swelling behavior of a polymer in $scCO_2$ under well-defined conditions, a method has been developed based on a liquid displacement technique. A key feature of this apparatus is the detection of liquids in steel capillaries under high pressures, by means of a resonance technique.

Based on this knowledge of the sorption and swelling behavior, the controlled foaming of rubbery polymer using $scCO_2$ has been explored successfully. This leads the way to a more detailed study of various polymer shaping operations applying supercritical carbon dioxide as the shaping agent.

6.8 References

1. R.G. Gilbert, *Emulsion Polymerization: A Mechanistic Approach*, Academic Press, London, 1995.
2. I.A. Maxwell, E.M.F.J. Verdurmen and A.L. German, *Makromo. Chem.* **193** (1992) 2677.
3. M.F. Kemmere, M.H.W. Cleven, M.A. van Schilt, J.T.F. Keurentjes, *Chem. Eng. Sci.* **57** (2002) 3929.
4. O. Pfohl, S. Petkov and G. Brunner, *Phase Equilibria for Windows*, V2.085 Release December 2000, Hamburg, 2000.
5. D. Peng and D.B. Robinson, *Ind. Eng. Chem. Fund.* **15** (1976) 59.
6. A.Z. Panagiotopolous and R.C. Reid, *ACS Div. Chem., Prepr.* **30** (1985) 46.
7. R. Stryjek and J.H. Vera, *Can. J. Chem. Eng.* **64** (1986) 820.
8. M.L. Michelsen and H. Kistenmacher, *Fluid Phase Equilibria* **58** (1990) 229.
9. G.A. Melhem, R. Saini and C.F. Leibovici, *Proceedings of the 2nd International Symposium on Supercritical Fluids*, Boston, 1991, p. 475.
10. P.M. Mathias, H.C. Klotz and J.M. Prausnitz, *Fluid Phase Equilibria* **67** (1991) 31.
11. R. Wiebe and V.L. Gaddy, *J. Am. Chem. Soc.* **62** (1940) 815.
12. R. Wiebe and V.L. Gaddy, *J. Am. Chem. Soc.* **63** (1941) 475.
13. M.B. King, A. Mubarak, J.D. Kim and T.R. Bott, *J. Supercrit. Fluids* **5** (1992) 296.
14. M. Lora and M.A. McHugh, *Fluid Phase Equilibria* **157** (1999) 285.
15. C.T. Kauter, *Ullmann's Enzyklopädie der Technischen Chemie* 12, Verlag Chemie, Weinheim, 1960, p. 392.
16. M.F. Kemmere, M.A. van Schilt, M.W.H. Cleven, A.M. van Herk and J.T.F. Keurentjes, *Ind. Eng. Chem. Res.* **41** (2002) 2617.
17. T. Adrian, M. Wendland, H. Hasse and G. Maurer, *J. Supercrit. Fluids* **12** (1998) 185.
18. I.C. Sanchez and R.H. Lacombe, *J. Phys. Chem.* **80** (1976) 2352.
19. R.H. Lacombe and I.C. Sanchez, *J. Phys. Chem.* **80** (1976) 2568.
20. I.C. Sanchez and R.H. Lacombe, *Macromolecules* **11** (1978) 1145.
21. E. Neau, *Fluid Phase Equilibria* **203** (2002) 133.
22. I.C. Sanchez, In *Encyclopedia of Physical Science and Technology*, 2nd edition, vol. 13, p. 153, Academic Press, Boston, 1992.
23. A. Fredenslund, J. Mollerupand K.R. Hall, *J. Chem. Eng. Data* **21** (1976) 301.
24. M.S. Gruszkiewicz, J.T. Sipowska, J.B. Ott, P.R. Brown and J.D. Moore, *J. Chem. Thermodyn.* **27** (1995) 507.
25. O. Redlich and A.T. Kister, *Ind. Eng. Chem.* **40** (1948) 345.
26. N. Koak, R.A. Heidemann, *AIChE J.* **47** (2001) 1219.
27. P.K. Jog and W.G. Chapman, *Macromolecules* **35** (2002) 1002.
28. Th.W. de Loos, W. Poot and G.A.M. van Diepen, *Macromolecules* **16** (1983) 111.

29. A.A. Gusev, F. Müller-Plathe, W.F. van Gunsteren and U.W. Suter, *Adv. Polym. Sci.* **116** (1994) 207.
30. F. Müller-Plathe, *Acta Polym.* **45** (1994) 259.
31. G.D. Smith, *Molecular Dynamics Simulations of Polymers: An Introduction*, internet publication: http://www.che.utah.edu/~gdsmith/tutorials/tutorial1.ppt.
32. N.F.A. van der Vegt, *Molecular dynamics simulations of sorption and diffusion in rubbery and glassy polymers*, Ph.D. thesis, Twente University, Enschede, 1998.
33. N.F.A. van der Vegt, W.J. Briels, M. Wessling and H. Strathmann, *J. Chem. Phys.* **110** (1999) 11061.
34. A.V. Lyulin and M.J. Michels, *Macromolecules* **35** (2002) 1463.

Summary

A global awareness of environmental issues regarding the widespread use of organic solvents in the polymer industry has driven the research towards more sustainable technologies. Promising alternatives for the replacement of organic solvents include supercritical fluids. The unique properties of supercritical fluids (SCFs) provide opportunities for a variety of polymer reaction and processing applications. Carbon dioxide ($scCO_2$), in particular, has been brought forward as an ideal organic solvent replacement, as it is environmentally benign, non-toxic, non-flammable and inexpensive. Moreover, its supercritical state is easily accessible due to its low critical temperature and pressure. However, the poor solubility of many high molecular weight components and polymers in $scCO_2$, limit its use as polymerization solvent. To study antisolvent effects caused by carbon dioxide on solvent-polymer systems, the influence of CO_2 on the phase behavior of poly(ethylene-co-propylene) (PEP) in ethylene has been modeled using the Sanchez-Lacombe and SAFT equations-of-state. Thereby monodispersity of the polymer has been assumed. Both models give a qualitative description of the increase in ethylene-PEP cloud-point pressures upon addition of CO_2. For a quantitative correlation with the Sanchez-Lacombe model, a temperature-dependent interaction parameter is required. Additionally, the parameter is determined for each individual cloud-point composition. For the SAFT model, one temperature dependent interaction parameter suffices for all compositions. The description of the phase behavior with the SAFT model is in much better agreement with experimental data than for the Sanchez-Lacombe model.

Although the solubility of polymers in $scCO_2$ is very limited, many polymers show a substantial sorption and swelling in carbon dioxide. Consequently, this enables $scCO_2$ to be used as a polymer shaping and processing medium, e.g. in the foaming of rubbers. Soft rubber foams like poly(ethylene-*co*-vinyl acetate) (EVA) are industrially applied in a broad range of products, including sports gear, insulation materials and drug delivery systems. The most common techniques for the shaping of porous polymers are foaming by thermally induced phase separation (TIPS) and the use of chemical foaming agents (CFAs). In this study, open microporous matrices of EVA have been formed using supercritical carbon dioxide. Prior to the foam expansion, the sorption and swelling behavior of EVA in $scCO_2$ has been investigated and a pressure-independent diffusion coefficient of CO_2 in EVA has been obtained from these experiments. The open microporous foams have been formed by a pressure quench of the carbon dioxide-swollen polymer matrix. Sorption pressure as well as temperature and decompression times appear to control the pore size and bulk density of the foam. Increasing the sorption

pressure or decompression rate produces more dense foams with a smaller pore size. Although higher sorption temperatures also reduce the pore size, the processing temperature is limited by the melting point of the polymer.

For the effective application of supercritical fluids as a polymer-processing medium, a thorough understanding of the phase behavior of polymers in high-density gases is required. Therefore, an apparatus has been developed for the simultaneous measurement of sorption and swelling of a polymer sample in a high-pressure gas. The sorption of the gas in the polymer is determined by measuring the pressure decay in a closed polymer-gas-mercury system. The swelling of the polymer is determined from a direct volume measurement of the polymer sample by means of submersion in mercury. This procedure eliminates the need for corrections of buoyancy and anisotropic dilation, as required in most conventional sorption and swelling measurements.

To enable fluid level detection in process equipment under high pressures, such as encountered in the sorption and swelling apparatus, a method has been developed, which enables the contactless measurement of liquid levels in thin opaque capillaries at high pressures. The method is based on the mass dependence of the resonance frequency of a section of a tube, which is determined from the electrical impedance of a coil exciting a magnet attached to the tube. The system has been theoretically described using a set of two Bernoulli-Euler beams, for which an analytical solution to the equation of motion has been derived. Validation experiments on a thick-walled stainless steel capillary partly filled with mercury show a good agreement between the model and the experimental data. Moreover, the sensitivity of the method appears to be adequate as a fluid level indicator for control purposes in industrial applications.

In this thesis, several aspect concerning the processing of polymers in supercritical fluids have been discussed. Nevertheless, future challenges in both measurement and modeling of polymer-supercritical fluid systems remain. These include the determination of the phase behavior in ternary and higher systems, such as encountered in the extraction of residual monomer from latices with $scCO_2$. Therefore, some modeling aspects of the partitioning behavior in aqueous $scCO_2$ systems are discussed. Additionally, recent thermodynamic consistency issues have been encountered for phase equilibria calculations using the Sanchez-Lacombe model. Implications for the Sanchez-Lacombe phase calculations in this thesis are described. Furthermore, the model description of supercritical mixtures using excess data, as well as the effect of polydispersity on polymer-supercritical fluid systems is discussed. Finally, some future applications of molecular dynamics in polymer systems are addressed.

Samenvatting

Een groeiend bewustzijn van de milieubezwaren verbonden aan het veelvuldig gebruik van organische oplosmiddelen in de polymeerindustrie heeft het onderzoek naar duurzame, nieuwe technologieën gestimuleerd. Veelbelovende alternatieven voor de vervanging van organische oplosmiddelen omvatten superkritische vloeistoffen. De unieke eigenschappen van superkritische vloeistoffen voorzien in een verscheidenheid aan polymerizatie en verwerkingstoepassingen. Met name superkritisch kooldioxide ($skCO_2$) wordt gezien als een ideale vervanger van organische oplosmiddelen, aangezien het milieuvriendelijk, niet giftig, onbrandbaar en goedkoop is. Daarnaast is het kritisch punt van kooldioxide makkelijk toegankelijk met een kritische temperatuur en druk van 31°C en 74 bar. Daarentegen wordt het gebruik van superkritisch kooldioxide als polymerisatie oplosmiddel beperkt door de veelal slechte oplosbaarheid van hoog-moleculaire stoffen. Om de anti-solvent effecten van kooldioxide op polymeer-oplosmiddel systemen te onderzoeken, is de invloed op het fasengedrag van het toevoegen van CO_2 aan het systeem etheen-poly(etheen-*co*-propeen) (PEP) gemodelleerd met de Sanchez-Lacombe en SAFT toestandsvergelijkingen. Hierbij is monodispersiteit van het polymeer verondersteld. Beide modellen geven een kwalitatieve beschrijving van de verhoging van de ethyleen-PEP ontmengdruk (cloud-point) veroorzaakt door toevoeging van CO_2. Voor een kwantitatieve beschrijving met het Sanchez-Lacombe model is een temperatuur-afhankelijke interactieparameter vereist. Bovendien wordt de interactieparameter voor elke cloud-point samenstelling apart bepaald. Daar staat tegenover, dat voor het SAFT model één temperatuur afhankelijke interactieparameter voor alle samenstellingen volstaat. De beschrijving van het fasengedrag met het SAFT model komt, vergeleken met het Sanchez-Lacombe model, beter overeen met de experimentele gegevens.

Hoewel de oplosbaarheid van polymeren in $skCO_2$ zeer beperkt is, vertonen veel polymeren een aanzienlijke sorptie en zwelling in kooldioxide. Dit maakt het mogelijk $skCO_2$ toe te passen als vormgevings- en verwerkingmedium, ondermeer bij het schuimen van rubbers. Zacht schuimvormig rubber als poly(etheen-*co*-vinylacetaat) (EVA) wordt industrieel toegepast in een brede scala van producten, uiteenlopend van sportuitrustingen tot isolatiematerialen en medicijndoceringssystemen. Gebruikelijke technieken voor het schuimen van polymeren zijn het schuimen door thermisch geïnduceerde fasenscheiding (TIPS) en het schuimen met behulp van chemische schuimvormers (CFAs). In dit onderzoek zijn open microporeuze EVA schuimen gevormd met behulp van superkritisch kooldioxide. Voorafgaand aan de schuimexpansie

is het sorptie- en zwelgedrag van EVA in skCO_2 onderzocht. Tevens is uit deze experimenten een druk-onafhankelijke diffusiecoëfficiënt van CO_2 in EVA verkregen. De open microporeuze schuimen zijn gevormd door middel van een snelle drukval in het kooldioxide-gezwollen polymeer. De poriegrootte en de bulkdichtheid van de gevormde schuimen blijken afhankelijk te zijn van zowel de sorptiedruk als de temperatuur en de decompressietijd. Verhoging van de sorptiedruk of de decompressie snelheid resulteert in schuimen met een hogere dichtheid en een kleinere poriegrootte. Verhoging van de sorptietemperatuur leidt ook tot een kleinere poriegrootte, waarbij echter de verwerkingstemperatuur beperkt wordt door het smeltpunt van het polymeer.

Voor efficiënte toepassing van superkritische vloeistoffen als polymeerverwerkings-medium is een grondig inzicht in het fasengedrag van polymeren in dichte gassen vereist. Hiervoor is een apparaat ontwikkeld voor de simultane meting van sorptie en zwelling van een polymeermonster in een hoge druk atmosfeer. De sorptie van het gas in het polymeer wordt bepaald door de drukval te meten in een gesloten polymeer-gas-kwik systeem. De zwelling van het polymeer wordt bepaald uit een directe volumemeting van het polymeermonster door middel van onderdompeling in kwik. Deze procedure elimineert de noodzaak voor correcties voor drijfvermogen en anisotrope uitzetting, zoals vereist in bepaalde conventionele sorptie en zwellingsmetingen.

Om het mogelijk te maken vloeistofniveaus te meten in hoge druk procesapparatuur, zoals zich voordoet in het sorptie- en zwellingsapparaat, is een methode ontwikkeld voor contactloze meting van vloeistofniveaus in dunne ondoorzichtige buizen onder hoge druk. De methode is gebaseerd op de massa-afhankelijkheid van de resonantiefrequentie voor een ingeklemd deel van de buis. Deze wordt bepaald uit de elektrische impedantie van een spoel die een aan de buis bevestigde magneet exciteert. Het systeem is theoretisch beschreven door middel van twee Bernoulli-Euler balken, waarvoor een analytische oplossing is afgeleid voor de bewegingsvergelijking. Validatie-experimenten met een gedeeltelijk met kwik gevulde, dikwandige roestvrij stalen buis laten een goede overeenkomst zien tussen het model en de experimentele gegevens. De gevoeligheid van de methode lijkt voldoende te zijn om te dienen als vloeistofniveau-indicator voor regeldoeleinden in industriële toepassingen.

In dit proefschrift zijn verscheidene aspecten van de verwerking van polymeren in superkritische vloeistoffen besproken. Niettemin, blijven er in de toekomst uitdagingen bestaan met betrekking tot het meten en modelleren van polymeer-superkritische vloeistof systemen. Dit betreft o.a. het bepalen van het fasengedrag in ternaire en hogere systemen, zoals voorkomend bij de extractie van restmonomeer uit latices met behulp van skCO2. Hiertoe zijn enige modelleringsaspecten van het verdelingsgedrag in waterige skCO2 systemen besproken. Recentelijk zijn thermodynamische consistentieproblemen

voor de berekening van fasenevenwichten met het Sanchez-Lacombe model aan het licht gekomen. De implicaties hiervan voor de Sanchez-Lacombe fasenberekeningen in dit proefschrift zijn besproken. Tevens zijn de modellering van superkritische mengsels met behulp van excesgegevens en de effecten van polydispersiteit op polymeer-superkritische vloeistof systemen beschreven. Tot slot zijn enige toekomstige toepassingen van moleculaire dynamica in polymeersystemen behandeld.

Dankwoord

Het is zover, na ruim vier jaar meten, rekenen en schrijven is de inhoud van het boekje af. Rest nog wellicht het meest belangrijke deel van het boekje: het bedanken van iedereen die direct danwel indirect heeft bijgedragen aan het totstandkomen van dit werk.

In de eerste plaats zijn dat natuurlijk mijn promotor en copromotor Jos en Maartje. Jullie hebben het mij mogelijk gemaakt dit onderzoek te verrichten, mij aangezet het op papier te zetten en het geschrevene van vele nuttige commentaren voorzien. Daarnaast dank ik Theo de Loos voor de gelegenheid om een deel van het werk aan de TU Delft uit te voeren.

Het bouwen van een hogedrukopstelling en het uitvoeren van hogedruk-experimenten vergt de kennis en hulp van velen. Voor het bouwen van het sorptie en zwelling apparaat wil ik Fred Neervoort, René Breeuwer, Jack Maat en Chris Luijk bedanken. Tjerk, Earl en Henny bedankt voor jullie hulp bij de experimenten in Eindhoven. Verder wil ik Marcus en Rob bedanken voor jullie hulp bij het modelleren van de diverse systemen. En niet te vergeten, Dion, bedankt voor de fantastische weergave van het badwater van Archimedes op de kaft.

Tot zover de mensen die inhoudelijk hebben bijgedragen aan het boekje. Minstens zo belangrijk zijn de mensen die het een bijzonder prettige ervaring hebben gemaakt om ruim vier jaar te werken bij SPD. Menigeen heeft daaraan bijgedragen. Hiervoor wil ik alle collega's van SPD bedanken, maar in het bijzonder mijn kamergenoten Gert-Jan en Xaviera en de buren Iris en Henny. Zonder jullie zou het een stuk saaier zijn geweest. Gezien de prettige ervaringen van de 'sociale buurt controle' de afgelopen jaren mogen jullie, Iris en Henny, nog een keer op mij passen tijdens de zitting als paranimfen.

Verder wil ik mijn ouders, familie, en vrienden bedanken voor hun steun. Tot slot, Saskia, bedankt voor je onvoorwaardelijke steun, vertrouwen en liefde.

Marc

Stellingen

behorende bij het proefschrift "Measurement and modeling of thermodynamic properties for the processing of polymers in supercritical fluids" van Marc Jacobs.

1. Behoudens milieuwetgeving, is het gebruik van superkritische technologie op industriële schaal alleen economisch haalbaar indien de herwinning van het superkritische medium gepaard gaat met een geringe drukval.

2. Superkritisch kooldioxide is zeer geschikt als schuimmedium voor rubberachtige polymeren welke CO_2-fiele groepen bevatten en is derhalve een goed alternatief voor conventionele schuimvormers als azodicarbonamide en p-tolueensulfonylhydrazide.
   dit proefschrift, hoofdstuk 3

3. Iteratieve correctie voor zwelling van het polymeer in gravimetrisch verkregen sorptiedata middels de Sanchez-Lacombe toestandsvergelijking welke geoptimaliseerd is aan dezelfde sorptiedata, leidt tot grote onzekerheid in de verkregen sorptiewaarden.
   dit proefschrift; Y. Sato, T. Takikawa, A. Sorakubo, S. Takishima, H. Masuoka en M. Imaizumi, Ind. Eng. Chem. Res. **39** *(2000) 4813.*

4. Door de ontoegankelijkheid van het volume van een gezwollen polymeer onder hoge druk, ontbreken data voor simultaan bepaalde sorptie en zwelling in de literatuur.
   dit proefschrift, hoofdstuk 5; A. Rajendran, B. Bonavoglia, G. Storti en M. Mazzotti, in AIChE 2003 Annual Meeting, San Fransisco, 2003, 95f.

5. Inactivatie van vegetatieve micro-organismen in sinaasappelsap door middel van pasteurizatie met behulp van superkritisch kooldioxide is op grond van versheid slechts zeer beperkt van toepassing, daar het sap vrijwel altijd reeds in het land van herkomst is geconcentreerd en derhalve al een extensieve hittebelasting heeft ondergaan.

6. Van iemand wiens valkuil volgens de Kern-Kwadranten van Ofman overlapt met een eigen allergie kan men op het persoonlijke vlak veel leren. Het betreft echter wel een steile leercurve.
PD-training SPD, Vught, 2001

7. Mode heeft enkel tot doel het instandhouden van de consumptie in Westerse maatschappijen.

8. Het rijgedrag van de gemiddelde Nederlandse automobilist druist in tegen zijn volksaard van zuinigheid, daar men middels de houderschapsbelasting ook voor de meest rechtse rijbaan heeft betaald.

9. Openbare geschiedschrijving vindt plaats onder auspiciën van het heersend leiderschap en is derhalve nooit objectief.

10. Het zit hem niet in het harde lopen, maar in het op tijd vertrekken.
mijn vader